ELECTRICAL TRANSPORT DURING PHASE TRANSFORMATION IN METALLIC GLASSES

Thesis by

Robert Schulz

In Partial Fulfillment of the Requirements

for the Degree of

Doctor of Philosophy

California Institute of Technology

Pasadena, California

1984

(Submitted May 23, 1984)

TO MY MOTHER

ACKNOWLEDGEMENTS

I am very grateful to Professor W.L. Johnson and Professor Pol Duwez for introducing me to the field of metallic glasses. I would especially like to thank Bill Johnson for his support and for giving me the opportunity to pursue my own interest in the field. His great knowledge in materials, constant enthusiasm and fascination in science, together with his friendship makes him a great person to work with.

I would like to thank Konrad Samwer for his help and encouragement with the work on Cu-Zr, Madhav Mehra and Bruce Clemens with Mo-Ru-B, Vladimir Matijasevic with Zr-Ni and the Mossbauer experiment, and finally Michael Atzmon and Pat Koen with the TEM results. For many useful discussions and experimental advice I would like to thank Art Williams and Mike Tenhover who were very helpful when I first joined the group.

On the technical side I would like to thank Concetto Geremia and Angela Bressan. Their help and companionship during the past years will always be cherished. I would like to acknowledge Johanne Laganiere for her great support during the writing of this thesis and also Dave Baxter for many useful comments.

To conclude, I wish to thank all the members of Bill's group who helped in making my years at Caltech fruitful and enjoyable.

Support for this work came from the National Research Council of Canada and from the United States Department of Energy.

ABSTRACT

Electrical resistivity measurements have been used as a primary tool to study relaxation phenomena and high temperature structural transformations in metallic glasses. We will try to correlate, throughout this work, the resistivity behavior with structural measurements from high and low angle X-ray scattering, transmission electron microscopy, Mossbauer experiments and low temperature superconductivity measurements to get a better understanding of the scattering mechanism during the phase transformation. We will distinguish between topological relaxation and chemical relaxation and in this latter case, emphasis will be given to phase separation. Three systems will be discussed extensively. Amorphous $Cu_{100-x}Zr_x$ around the equiatomic composition, $(Mo_{0.6}Ru_{0.4})_{100-x}B_x$ for boron concentrations ranging from x=14 to x=22 and $(Zr_{1-x}Hf_x)_{62}Ni_{38}$ across the concentration range. We will show that upon annealing at temperature above 300°C, $Cu_{50}Zr_{50}$ phase separates into two amorphous phases of concentration close to $CuZr_2$ and $Cu_{10}Zr_7$. During the phase separation an anomalous resistivity behavior, similar to the one observed during the early stage of Guinier-Preston zones formation in crystalline alloys is seen. In Mo-Ru-B alloys, the nonlinear behavior in resistivity is correlated with the presence of a peak in the small angle X-ray intensity and is explained in term of spinodal decomposition caused by the diffusion of boron in the amorphous matrix. In $(Zr_{1-x}Hf_x)_{62}Ni_{38}$, an exothermic transformation which gives rise to an increase in resistivity but no resolvable Bragg peaks in the high angle X-ray pattern is investigated in detail.

The applicability of the Ziman formalism to successfully explain the behavior of the resistivity in all these cases is questioned and an alternative approach, based on d-band conduction, is proposed. New ways of understanding transport phenomena during structural relaxation in metallic glasses follow from these discussions.

TABLE OF CONTENTS

		Page
I.	INTRODUCTION	1
II.	THEORETICAL ASPECTS	9
	II.1 The Ziman Formalism	9
	II.2 Topological Relaxation	18
	A. The Kelton-Spaepen Approach	19
	B. Egami's Model for Structural Relaxation	23
	C. The Allia - Turtelli Theory	25
	D. Phenomenological Approach Based on the Cohen and Grest Theory of the Glass Transition	26
	II.3 Chemical Relaxation	32
	A. The Rossiter and Wells Theory	36
	B. The Hillel, Edwards and Wilkes Theory	39
	C. Application to Nucleation in Topologically Random Structures	43
	D. The Case of Spinodal Decomposition	49
III.	EXPERIMENTAL CONSIDERATIONS	52
	A. The Resistivity Measurements	53
	B. The Structural Measurements	57
IV.	RESULTS AND DISCUSSIONS	
	IV.1 $Cu_{100-x}Zr_x$ Glasses	62
	IV.2 $(Mo_{0.6}Ru_{0.4})_{100-x}B_x$ Glasses	84
	IV.3 $(Zr_{1-x}Hf_x)_{62}Ni_{38}$ Glasses	110
V.	EVIDENCE FOR d-BAND CONDUCTION IN METALLIC GLASSES	136
VI.	CONCLUSION	158
REFERENCES		162

LIST OF TABLES

		Page
Table II.3.1	Parameters used for calculating the excess resistivity during the growth of fcc microcrystals in a topologically random structure.	48
Table II.3.2	Size and number of atoms for several fcc spherical microcrystals.	48
Table IV.1.1	G(r) parameters for $Zr_{50}Cu_{50}$ metallic glasses (a) as quenched (b) annealed 11h. at 210°C and (c) subsequently annealed 9h. at 300°C.	82
Table IV.2.1	Crystallization temperatures and the % drop of the resistivity during the first two steps of the crystallization of $(Mo_{0.6}Ru_{0.4})_{100-x}B_x$ for x=14, 18, 22.	90
Table IV.2.2	G(r) parameters for $(Mo_{0.6}Ru_{0.4})_{100-x}B_x$ after several heat treatments.	105
Table IV.3.1	Temperatures of the exotherms and the relative change in electrical resistance for each transition occurring in $(Zr_{1-x}Hf_x)_{62}Ni_{38}$ for x=0, 50, 100.	116

		Page
Table IV.3.2	Superconductivity transitions, critical field gradients and average electronic diffusivities for as quenched and heat treated $Zr_{62}Ni_{38}$.	126
Table IV.3.3	Quadrupole splitting for different sites in $(Zr_{0.62}Ni_{0.38})_{99.8}Fe_{0.2}$ alloys.	132
Table V.1	Electronic density of states at the Fermi level together with other parameters for $Cu_{100-x}Zr_x$ metallic glasses.	154

LIST OF FIGURES

Fig.		Page
1.1a	Change of electrical resistance with temperature, normalized to the value at 300°K for $Cu_{73}Tl_{27}$ metallic glasses (Heating rate = 10°K/min.).	4
1.1b	Enlargement of (a) showing the excess resistivity above the linear contribution observed at low temperature.	4
1.2	The structure factor S(Q) obtained from neutron diffraction for $Cu_{66}Tl_{34}$ in the liquid state and in the glassy state.	6
1.3	Excess resistivity measured for $Cu_{73}Tl_{27}$ glasses during the first and the second heating cycle (Heating rate = 10°K/min.). After the second cycle a reversible behavior in the resistivity can be achieved.	7
2.2.1	Schematic illustration of the first peak of the structure factor S(Q) in the as quenched state, relaxed state and at high temperature.	21
2.2.2	Relative change in resistivity as a function of annealing time at various temperatures for $(Mo_{0.6}Ru_{0.4})_{78}B_{22}$ glasses. The solid line is a fit to the Kelton-Spaepen theory of structural relaxation.	22
2.2.3	Relative change in resistivity for $Au_{0.77}Ge_{0.136}Si_{0.094}$ alloys calculated for different heating rates together with the experimental data of Chen and Turnbull (ref. 31).	29

		Page
2.3.1	Phase diagram for a binary alloy (or the infinite three dimensional Ising model, ref. 36) and the evolution of a high temperature configuration following a quench to a temperature $T = 0.59\ T_c$.	33
2.3.2	Development with time of the structure factor $S(K,t)$ (full line) corresponding to a quench from a temperature above the coexistence curve to a temperature $T = 0.59\ T_c$ inside the spinodal region (see fig. 2.3.1) (the data are from ref. 36). Also represented in the figure is the function $K^3 \lvert u(K)\rvert^2 = K^3/(1+(K/\lambda)^2)^2$ (dashed lines) for different values of the parameter .	35
2.3.3	Structure factor S(K) for spherical fcc clusters. The hard sphere atomic radius is taken to be 1.3 Å. The first ten shells are represented.	42
2.3.4	Normalized resistance trace taken at a heating rate of $10^{o}C$/min. for $Pd_{64}Y_{36}$ metallic glasses.	44
2.3.5	Calculated excess resistivity during the growth of fcc microcrystals in a topologically random structure. The excess resistivity is plotted vs the size of the zones. All the parameters relevant to this calculation can be found in Table II.3.1 and II.3.2	47
3.1	Picture of the experimental setup.	55

		Page
3.2	Picture and schematic design of the tip of the resistivity probe.	56
3.3	Mossbauer experimental setup and the drive electronics.	59
4.1.1	The main and the second band of the radial distribution function for the Cu-Zr system across the concentration range.	65
4.1.2	Average nearest neighbor distances vs Zr concentration for $Cu_{100-x}Zr_x$ metallic glasses.	66
4.1.3 & 4.1.4	Relative change with time of the electrical resistance of $Cu_{50}Zr_{50}$ in isothermal annealing $R_o = R(t=0)$.	68 69
4.1.5	High angle X-ray scans with CuK radiation for CuZr (a) as quenched (b) annealed 10h. at 300°C (c) annealed 10h. at 350°C.	71
4.1.6	Change in the electrical resistance with temperature of $Cu_{50}Zr_{50}$ for different pre-annealed conditions. $R_o = R(T=300K)$.	72
4.1.7	X-ray diffraction pattern of (a) $CuZr_2$ crystalline powder (b) CuZr annealed 12h. at 350°C then quenched after the first resistivity drop (c) same sample quenched after the second resistivity drop (d) $Cu_{10}Zr_7$ crystalline powder.	74

		Page
4.1.8	X-ray diffraction scans with Mok ratiation for CuZr, $Cu_{10}Zr_7$ and $CuZr_2$ (a) as quenched (b) annealed at 210°C for 10h. (c) sample b annealed at 300°C for 9h.	75
4.1.9	Pair distribution functions for $Cu_{50}Zr_{50}$ (a) as quenched (b) annealed at 210°C for 9h. (c) sample b annealed at 300°C for 9h.	76
4.1.10	Pair distribution function for (a) $Cu_{10}Zr_7$ (b) $CuZr_2$.	78
4.1.11	Pair distribution function for as quenched $Cu_{50}Zr_{50}$ and the RDF between the annealed $Cu_{50}Zr_{50}$ at 300°C for 9h. and the as quenched sample.	79
4.1.12	The full curve (a) which represents the sum of three G(r) [(b) (67.8% $Zr_{50}Cu_{50}$), (c) (26.9% Zr_7Cu_{10}) and (d) (5.2% Zr_2Cu)] corresponds to a least square fit to the data for the annealed $Cu_{50}Zr_{50}$ (cross points).	80
4.1.13	(a) TEM of as quenched ZrCu (b) annealed 11h. at 210°C and 9h. at 300°C (c) diffraction pattern of the annealed sample.	81
4.2.1	Resistance traces obtained at a heating rate of 15°C/min. for x=14 , 18 and 22 (R_o= room temperature resistance).	89
4.2.2	The heat treatment, monitored by resistance changes, applied to $(Mo_{0.6}Ru_{0.4})_{86}B_{14}$ for the crystallization study.	91

Page

4.2.3 X-ray scan (CuK_α radiation) of the crystalline phases obtained after each quench showed in fig. 4.2.2 . 92

4.2.4 Enlargement of the resistance traces around the crystallization temperature. 94

4.2.5 Enlargement of the resistance traces below the crystallization temperature for x=14, 18 and 22. (Region "a" and "b" correspond to region II and III in fig. 10 of ref. 4.2.16). The lower plot represents the excess resistivity above the extrapolated linear temperature dependence characteristic of the low temperature region. 95

4.2.6 Percent change in resistance as a function of annealing time at various temperatures. The solid lines are fit to the Kelton-Spaepen theory. 97

4.2.7 Enlargement of the resistance traces below the crystallization temperature for x=14 and 22 annealed previously 12h. at various temperatures. 99

4.2.8 Correlation between the excess resistivity and the change in the density of states (from 4.2.16) vs the reduced annealing temperature. T_{cr} is the crystallization temperature (^oC) corresponding to the onset of the drastic drop in the measured property. 101

		Page
4.2.9	Normalized specific heat coefficient vs conductivity for $(Mo_{0.6}Ru_{0.4})_{100-x}B_x$ (ref. 4.2.22 and 4.2.23) and $(Zr_2Ni)_{100-y}B_y$ glasses (ref. 4.3.31). The normalization constants correspond to x=18 and y=0 respectively.	104
4.2.10	Reduced radial distribution function for x=14 and 22 annealed for different time at 525°C.	106
4.3.1	Resistance and DSC traces on $Zr_{62}Ni_{38}$, $(Hf_{0.5}Zr_{0.5})_{62}Ni_{38}$ and $Hf_{62}Ni_{38}$.	115
4.3.2a	Enlargement of the resistance traces below the crystallization temperature. The dashed line represents the extrapolated linear dependence at low temperature.	118
4.3.2b	Excess resistivity above the linear dependence obtained from a least square fit of the data at low temperature.	118
4.3.3	Radial distribution function before (full lines) and after (dashed lines) the heat treatment represented in the onset of each figure for (a) $Zr_{62}Ni_{38}$ (b) $(Hf_{0.5}Zr_{0.5})_{62}Ni_{38}$ and (c) $Hf_{62}Ni_{38}$.	121
4.3.4	Superconducting transition measured resistively for $Zr_{62}Ni_{38}$ as quenched and heat treated beyond the first exotherm.	124
4.3.5	Upper critical field vs temperature for $Zr_{62}Ni_{38}$ as quenched and heat treated beyond the first exotherm at a heating rate of 15°C/min.	125

		Page
4.3.6	a) and b) TEM micrographs of heat treated $Zr_{62}Ni_{38}$.	128
4.3.7	Diffraction pattern of heat treated $Zr_{62}Ni_{38}$ (a) selected area in fig. 4.3.6 containing no pits and holes (b) area including holes and sample's edges.	129
4.3.8	Mossbauer spectra of $(Zr_{62}Ni_{38})_{99.8}Fe_{0.2}$ as quenched, heat treated beyond the first exotherm and fully crystallized after the second exotherm.	131
5.1	Upper critical field gradient vs concentration for Mo-Ru-B and Zr-Ni-B systems.	141
5.2	Normalized density of states vs conductivity (or resistivity for x>55) for the Ni-Zr system. The concentrations are indicated in parenthesis. The data are normalized to the respective values for x=55.	145
5.3	Upper critical field gradient vs concentration for Ni-Zr and Cu-Zr systems.	146
5.4	Log-Log plot of the upper critical field gradient vs the density of states for the Cu-Zr and Ni-Zr systems.	148
5.5	Positions of the first peak of the structure factor vs composition for the Zr-Ni system.	150

		Page
5.6	Normalized density of states vs conductivity for the Cu-Zr system. The concentrations are indicated in parentheses and the density of states are from either calorimetric measurements or superconductivity measurements. The data are normalized to the respective values for x=55.	153
5.7a	Calculated electronic diffusivity for the s and d states vs the Cu concentration for different parameters (or s-d scattering matrix elements).	156
5.7b	Calculated conductivities for a parameter α=0.3 together with the experimental data points from Altounian et al. (ref. 70 and 75).	156
6.1	Calculated local density of states: for nickel in a solid-like cell (high density region), for liquid nickel and for crystalline nickel. (The data are from ref. 83)	160

I. INTRODUCTION

In September of 1984, it will be the twenty-fifth anniversary of the discovery of the first metallic glasses. It was, indeed, in September of 1959 at Caltech, that Pol Duwez and his co-workers[1] found a broad diffuse band in the X-ray diffraction pattern of a gold-silicon alloy rapidly quenched from the melt. Prior to this date, work on amorphous metals was limited to very thin films[2] obtained by techniques such as physical vapor deposition, sputtering and electrodeposition. Because of their geometry, these samples were restricted to a certain limited type of experiments. The importance of the discovery of Duwez resides in the bulk nature of the samples which can be obtained by quenching from the melt. The interest of physicists and material scientists in the field has been growing almost exponentially and since the discovery of the "melt-spinner" with which comes the possibility of massive production, the engineers as well contributed to improve our knowledge on noncrystalline metals.

Among all of the interesting properties of amorphous metals, probably one of the most important is the electrical conductivity. However, the basic theoretical difficulty which arises from the lack of long range order and the fact that the Bloch theorem is not valid makes transport phenomena in these systems, a very controversial field.

These difficulties have limited the use of electrical resistivity measurements as a structural probe for short range order in amorphous metals. Some experimentalists even question usefulness of these

measurements in metallic glasses because of the difficulty in assigning an unequivocal, specific scattering mechanism. On the other hand, the measurements are relatively easy to perform and, despite the above theoretical considerations, large amounts of data and extensive work can be found in the literature.

Most of the studies of the electrical transport in metallic glasses concern the low temperature behavior. Many models and scattering mechanisms have been proposed, with varying degrees of success, to explain the very low temperature dependence of the resistivity: Kondo effect[3], scattering from two-level tunneling states[4], coherent magnetic scattering[5], localization[6] etc. In the low and intermediate temperature range, theories like the localized spin-fluctuation scattering model[7] and especially the diffraction model[8] based on the extended Ziman metal theory have been used. Both of these theories predict a T^2 dependence of the resistivity at low temperature ($T < \theta$) and a linear dependence at high temperature ($T > \theta$). θ is the Debye temperature. The diffraction model has been quite successful in explaining the temperature coefficient of the resistivity at high temperature in many amorphous metallic systems and in particular, the negative temperature coefficient observed for the Cu-Zr and the Ni-Zr systems which we will discuss extensively in the following chapters.

The purpose of this thesis is not to study or criticize any of these scattering mechanisms in particular, but instead to use the most widely applied model (i.e. the extended Ziman theory), together with the electrical resistivity, as a tool to detect and study phase transformations which occur at high temperature in metallic glasses.

Because of their metastable nature, phase transformations, in which I include relaxation phenomena (topological as well as chemical) are inherent to metallic glasses. Phase separation of a homogenous phase into two distinct amorphous phases represents by itself an important problem in the field of glassy metals. We will show that resistivity measurements can be very useful to locate, in the temperature-time diagram where such separation occurs, and to study its kinetics. The behavior of the resistivity around the glass transition and its dependence on the free volume content can also be used to test the various theories proposed for the glass transition. Several authors realized how helpful high temperature resistivity measurements can be in following the crystallization processes of metallic glasses and numerous studies can be found in the literature[9-11]. For this reason we will restrict our interest in this thesis to amorphous phase transformations or at most, to the very early stage of crystallization.

Fig. 1.1a shows a typical resistivity scan on a $Cu_{73}Tl_{27}$ amorphous alloy. At first sight, the resistivity varies linearly with temperature, from room temperature to around 250°C, in agreement with the prediction of the diffraction model at high temperature. Around the crystallization temperature, the resistivity decreases by more than 40%. This is because of the much greater static order of the polycrystalline phase. The typical temperatures of interest in the thesis will include a range starting from a few hundred degrees below the crystallization temperature. Fig.1.1b shows that, on a small scale, the resistivity is actually highly nonlinear in this range of

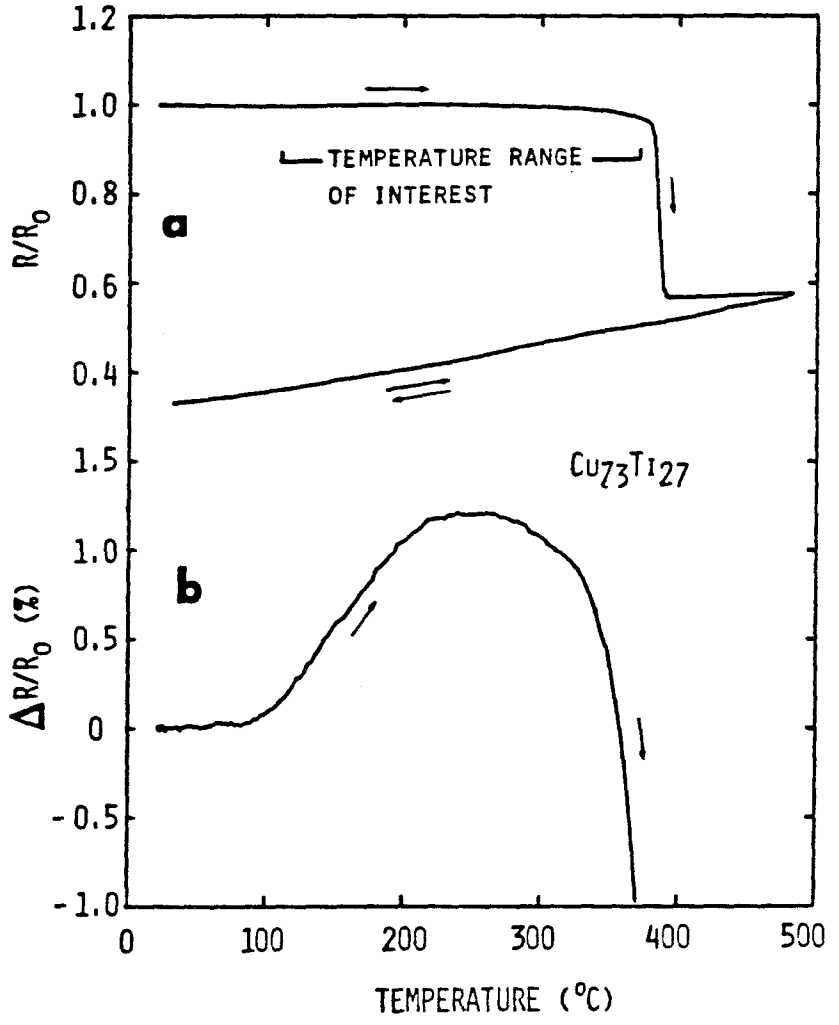

Fig. 1.1a & b

Change of electrical resistance with temperature, normalized to the value at 300°K for $Cu_{73}Tl_{27}$ metallic glasses (Heating rate = 10°K/min.).

Enlargement of (a) showing the excess resistivity above the linear contribution observed at low temperature.

temperature. The plot shows the excess resistivity above the linear contribution due to phonon scattering. The increase in the excess resistivity reflects an evolution towards a state of higher chemical short range order (CSRO). It has been demonstrated[12], indeed, that CSRO exists in $Cu_{66}Ti_{34}$ alloys in the liquid as well as in the glassy phase. Fig.1.2 shows the structure factor S(Q) obtained by neutron diffraction from a $Cu_{66}Ti_{34}$ alloy in the liquid and glassy state. The prepeak at $Q \approx 1.9 Å^{-1}$ provides direct experimental evidence of CSRO or a tendency for unlike atoms to be neighbors. This prepeak is the diffraction evidence of a non-random, like-atom correlation at the second-neighbor distance ($R_2 = (5/4)(2\pi/1.9) \approx 4.1Å$) and represents a pseudo-periodicity A-B-A-B in the random structure. The size of the prepeak in fig. 1.2 shows that CSRO is enhanced on vitrification. Therefore, by annealing below the crystallization temperature, the CSRO should grow and the increase in resistivity in fig. 1.1b just reflects this tendency. Fig. 1.3 shows that after a non-reversible ordering process observed during the first heating cycle, we can achieve a reversible behavior in the variation of the resistivity vs. temperature which can be thought to be a reflection of the " metastable equilibrium state" of chemical short-range order. The higher the temperature, the lower the degree of order and the smaller is the resistivity. Balanzat et al.[13] found similar behavior for a $Cu_{50}Ti_{50}$ amorphous alloy.

This brief introduction shows how sensitive and powerful resistivity measurements can be in detecting ordering processes in metallic glasses. Before moving further into the experimental results, I will describe in chapter II some of the theoretical

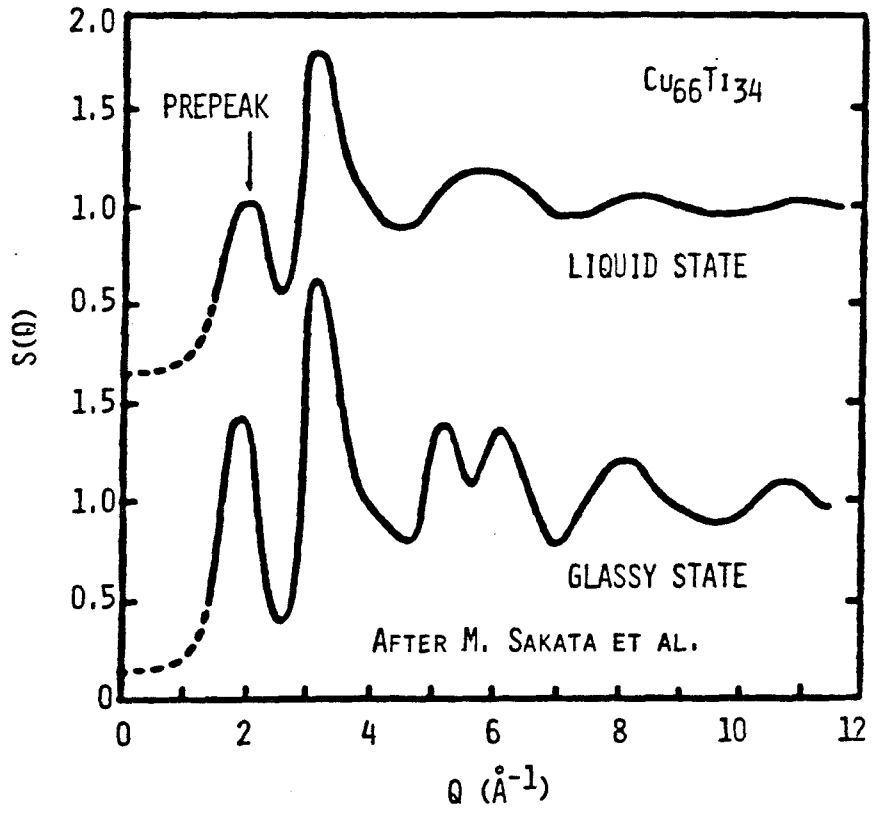

Fig. 1.2

The structure factor S(Q) obtained from neutron diffraction for $Cu_{66}Ti_{34}$ in the liquid state and in the glassy state.

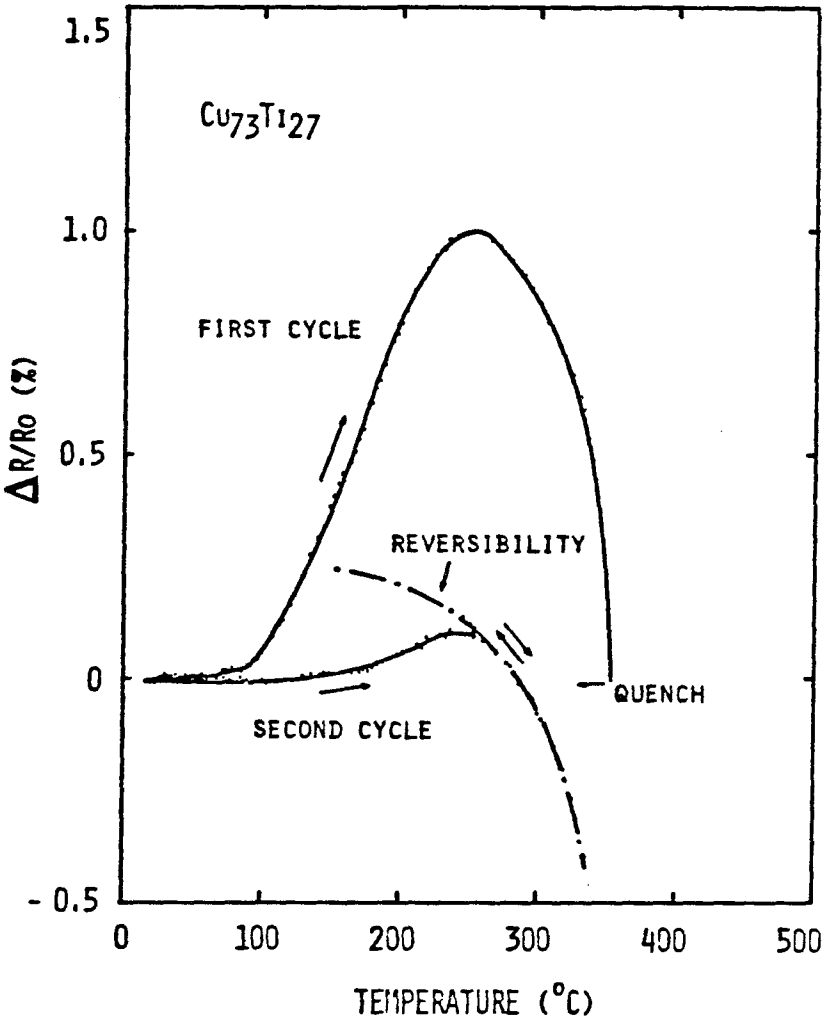

Fig. 1.3

Excess resistivity measured for $Cu_{73}Ti_{27}$ glasses during the first and second heating cycle (Heating rate = 10°K/min.) After the second cycle a reversible behavior in the resistivity can be achieved.

background necessary in order to fully appreciate the results in this thesis. I will describe in detail, topological as well as chemical relaxation and I will present the standard approach used to investigate problems such as phase separation and phase segregation in amorphous structures. Chapter V represents an attempt to explain the behavior of the electrical resistivity for the various systems studied in this research, from a different point of view than the one usually adopted i.e. the extended Ziman approach based on Boltzmann's transport theory. This will give rise, in conclusion, to new ways of interpreting relaxation phenomena in amorphous structures.

II. THEORETICAL ASPECTS

II.1 The Ziman Formalism

Transport theory in a highly disordered structure is one of the major unresolved problems in solid state physics. Several models have been proposed to explain the behavior of the electrical resistivity in metallic glasses and in particular, the negative temperature coefficient of resistivity found when the magnitude of ρ is larger than 150 $\mu\Omega$ cm. I will choose, in this work, to interpret the results within only one model: The Ziman Formalism. This approach has been particularly successful in explaining, at least qualitatively most of the transport phenomena observed in metallic glasses. It is a suitable choice because it relates electrical resistivity to atomic structure in a natural manner. We should keep in mind, however, that its applicability to metallic glasses, where the electron mean free path is very short, is questionable. Indeed, the Ziman formalism is derived from the Boltzmann transport theory in the weak scattering regime which fails when the mean free path becomes comparable to the lattice spacing or when the resistivity reaches values on the order of 200 $\mu\Omega$ cm. Nevertheless, the Ziman theory is still widely used in the field and for this reason, I will address the important problem of its applicability in chapter V.

In the original formulation, Ziman[14] considered the elastic scattering of nearly free electrons in plane wave states by the pseudo-potential associated with the ions in a simple liquid metal. Using the Boltzmann equation in the relaxation time approximation we can write in the Born approximation $\rho = m/ne^2\tau$, where m is the electron mass, n is the free electron density and e is the

electronic charge. The scattering rate $1/\tau$ is given by the following relation $1/\tau = \int_0^{2\pi} (1-\cos\theta)\, P_{kk'}(\theta)\, d\theta$ where $P_{kk'}(\theta)$ is the probability of scattering by unit time and unit solid angle. Using the Fermi Golden Rule we may write this scattering probability as $P_{kk'} = \frac{2\pi}{h} |U_{kk'}|^2 \rho(E = E_f)$ where $\langle U_{kk'} \rangle$ is the matrix element for scattering from state k to k' by the total potential and $\rho(E=E_f)$ is the density of states at the ferml level. Assuming a quadratic dispersion relation and a spherical Fermi surface we obtain $\rho(E=E_f) = \frac{mVk_f}{8\pi^3 h^2}$ where V is the total volume and k_f is the Fermi wave vector which is related to the electron density by $k_f = (3\pi^2 n)^{1/3}$. Using the well-known relation $v_f = hk_f/m$ for the Fermi velocity the resistivity becomes:

$$\rho = \frac{12\pi\Omega}{he^2 v_f^2} \int_0^1 N |U_{kk'}|^2 \left(\frac{K}{2k_f}\right)^3 d\left(\frac{K}{2k_f}\right) \qquad (2.1.1)$$

$K = k-k'$ is the scattering vector and Ω is the average atomic volume. The matrix element $\langle U_{kk'} \rangle$ can be written as:

$$\langle \psi_{k'} | U | \psi_k \rangle = \frac{1}{V} \int_0^V e^{iKr}\, U(r)\, d^3r \qquad (2.1.2)$$

where the total potential is considered as a sum of pseudopotentials associated with each of the ions $U(r) = \sum_i u_l(r-r_l)$. If $u_l^{(K)}$ is the Fourier transform of the pseudopotential, the interference function

I(k), which I will take to be equal to $N|U_{kk'}|^2$ becomes:

$$I(k) = \frac{1}{N} \left| \sum_i u_i(K)\, e^{iK\cdot r_i} \right|^2 \qquad (2.1.3)$$

For a monoatomic liquid the structure factor is defined as:

$$a(K) = \frac{1}{N} \left| \sum_i e^{iK\cdot r_i} \right|^2 \qquad (2.1.4)$$

therefore, the interference function becomes:

$$I(K) = a(K)\, |u(K)|^2 \qquad (2.1.5)$$

and the expression 2.1.1 for the resistivity becomes:

$$\rho = \frac{12\pi\Omega}{he^2 V_f^2} \int_0^1 d\left(\frac{K}{2k_f}\right)\left(\frac{K}{2k_f}\right)^3 a(K)\, |u(K)|^2 \qquad (2.1.6)$$

This is the classical Ziman formula in its usual form. It is easy to show that the structure factor in eq. 2.1.4 can be related to the radial pair distribution function g(r) defined as follows:

$$\frac{N}{V}\, g(r) = \frac{1}{N} \left\langle \sum_{i\neq j} \delta(r - r_i + r_j) \right\rangle$$

through the relation:

$$a(K) = 1 + \frac{1}{N} \sum_{i\neq j} e^{iK\cdot(r_i - r_j)}$$

$$= 1 + \frac{N}{V} \int_0^\infty (g(r) - 1)\, \frac{\sin(Kr)}{Kr}\, 4\pi r^2 dr \qquad (2.1.7)$$

Faber et al.[16] have extended this theory to binary simple liquid metals by introducing the partial structure factor $a_{\alpha\beta}(K)$ which is related to the partial pair-correlation function $g_{\alpha\beta}(r)$ by an expression analogue to eq. 2.7. $g_{\alpha\beta}(r)$ is the probability of finding an ion of type α in a unit volume at a distance β from the center of the β ion, normalized in such a way that it tends to unity for larger r. In this case eq. 2.1.3 or $a(K)|u(K)|^2$ in the expression for the resistivity (2.1.6), has to be replaced by:

$$I(K) = c_1u_1^2 + c_2u_2^2 + c_1^2u_1^2(a_{11} - 1) + c_2^2u_2^2(a_{22} - 1) + 2c_1c_2u_1u_2(a_{12} - 1) \qquad (2.1.8)$$

It is interesting to note that for a substitutional alloy in which the two constituents have the same atomic volume and the same structure factor $a_{11}=a_{22}=a_{21}=a$, eq. 2.1.8 can be reduced to:

$$I(K) = (c_1u_1^2 + c_2u_2^2)\, a(K) + c_1c_2(u_1 - u_2)^2\,(1 - a(K))$$

$$= \overline{(u^2)}\, a(K) + (u_1 - u_2)^2\, c(1-c)\,(1 - a(K)) \qquad (2.1.9)$$

therefore, for the resistivity one obtains:

$$\rho = \rho_1 + \rho_2$$

where $$\rho_1 = \frac{12\pi\Omega}{he^2v_f^2} \left\langle (cu_1^2 + (1 - c)u_2^2)\, a(K) \right\rangle$$

and $$\rho_2 = \frac{12\pi\Omega}{he^2v_f^2}\, c(1 - c) \left\langle (u_1 - u_2)^2\,(1 - a(K)) \right\rangle$$

ρ_2 gives rise to the Nordheim's rule and ρ_1 varies in a more or less linear fashion between the resistivity of the two pure constituents. In the above expressions $\langle f(K) \rangle$ means

$\int_0^1 f(K)\left(\frac{K}{2k_f}\right)^3 d\left(\frac{K}{2k_f}\right)$. Bhatia and Thornton[17] proposed a different formalism for binary alloys and introduced new correlation functions which, in terms of the partial structure factors defined previously, can be written as:

$$a_{NN}(K) \equiv \frac{1}{N}|N(K)|^2 = c_1^2 a_{11} + c_2^2 a_{22} + 2c_1c_2a_{12}$$

$$a_{CC}(K) = \frac{1}{N}|C(K)|^2 = c_1c_2(1 + c_1c_2(a_{11} + a_{22} - a_{12})) \qquad (2.1.10)$$

$$a_{NC}(K) = \mathrm{Re}(N(K)^*C(K)) = c_1c_2(c_1(a_{11} - a_{12}) - c_2(a_{22} - a_{12}))$$

these were called the density-density, concentration-concentration and density-concentration correlation functions. N(K) and C(K) are respectively the Fourier transform of the local deviation in the total number density and the mean concentration:

$$N(K) = \sum_{i,\alpha=1,2} e^{iK\cdot r_i^\alpha}$$
$$C(K) = \frac{1}{N}\left(c_2 \sum_i e^{iK\cdot r_i^1} - c_1 \sum_i e^{iK\cdot r_i^2}\right) \qquad (2.1.11)$$

Using eq. 2.1.11, eq. 2.1.3 for the interference function becomes:

$$I(K) = \frac{1}{N}\left| \bar{u}\, N(K) + N(u_1 - u_2)\, C(K) \right|^2$$
$$= \bar{u}^2 a_{NN}(K) + (u_1 - u_2)^2 a_{CC}(K) + 2\bar{u}(u_1 - u_2) a_{NC}(K) \qquad (2.1.12)$$

where $\bar{u} = c_1u_1 + c_2u_2$. When the partial atomic volumes of the two species in a binary alloy are nearly identical as is for the case of the regular solution, then $a_{NC}(K) \approx 0$ for all K and only two

Independent structure factors are needed to describe the resistivity completely. Furthermore, if we have an ideal solution (heat of mixing = 0) the concentration-concentration correlation function is given by $u_{CC}(K) = c(1-c)$ and expression 2.1.12 becomes identical to equation 2.1.9.

The resistivity can therefore be expressed in terms of a topological and chemical part.

$$\rho \approx \rho_{TSRO} + \rho_{CSRO}$$

$$\rho_{TSRO} = \frac{12\pi\Omega}{he^2 v_f^2} \int_0^1 \bar{u}^2 \, a_{NN}(K) \left(\frac{K}{2k_f}\right)^3 d\left(\frac{K}{2k_f}\right) \qquad (2.1.13a)$$

$$\rho_{CSRO} = \frac{12\pi\Omega}{he^2 v_f^2} \int_0^1 (u_1-u_2)^2 \, a_{CC}(K) \left(\frac{K}{2k_f}\right)^3 d\left(\frac{K}{2k_f}\right) \qquad (2.1.13b)$$

During structural relaxation, the changes in bond distances and angles which leads to a higher topological short range order, affect the resistivity through eq. 2.1.13a whereas the exchanges of chemically different neighbors which leads to a higher chemical short range order, affect the resistivity through eq. 2.1.13b.

In order to extend the Ziman formalism to liquid transition metals where the scattering is strong and the electron mean free path is very short, Evans et al.[18] replaced in the original Ziman formula (eq. 2.1.6) the weak pseudopotential u(K) by the t-matrix for scattering from state k to k' by the muffin-tin potential of the ions.

$$t(K) = -\frac{2\pi\hbar^3}{m\Omega\sqrt{2mE_f}} \sum_{\ell} (2\ell + 1)\sin(\eta_\ell(E_f))e^{i\eta_\ell} P_\ell(\cos\theta) \qquad (2.1.14)$$

For transition metal elements, the d-phase shift η_2 dominates and since most of the contribution to the integral in eq. 2.1.6 comes from the region near $2k_f$ we can write to a reasonable approximation:

$$\rho \approx \frac{30\pi^3 h^3}{me^2 \Omega k_f^2 E_f} \sin^2(\eta_2)\, a(2k_f) \qquad (2.1.15)$$

For binary transition metal alloys, an expression similar to eq. 2.1.8, in which $u_1(K)$ and $u_2(K)$ are replaced by single site t-matrices, has to be used in the expression for the resistivity.

The temperature dependence of the resistivity can be included by taking into account the change in the structure factor (eq. 2.1.4) with temperature. $a(K)$ has to be replaced by the resistivity static structure factor $S(K)$ which can be expanded for an amorphous Debye solid as[19]:

$$S(K) = S_0(K) + S_1(K) + S_2(K) + \ldots$$

where

$$S_0(K) = a(K)\, e^{-2W} \qquad \ldots\text{elastic term}$$

$$S_1(K) = \alpha(K)\, A^{\rho}(K)\, (T/\theta)^2 I_2(\theta/T) e^{-2W} \qquad \ldots\text{one phonon term}$$

$$S_2(K)+\ldots \approx 1-(1 + 2W)\, e^{-2W}$$

The Hernandez-Calderone approximation[20] to the multiphonon series has been used for the higher order terms. In the above expression $\alpha(K) = \frac{3h^2K^2}{mk_B\theta}$ where M is the atomic weight, θ is the Debye temperature and k_B is the Boltzmann constant, e^{-2W} is the Debye Waller damping factor with $2W = \alpha(K)(T/\theta)^2 I(\theta/T)$, $A^{\rho}(K)$ is the

average of the structure factor a(K) over the Debye sphere center on K and finally:

$$I(\theta) = \int_0^{\theta/T} \frac{x\,dx}{2} \coth(x/2)\,dx \quad \begin{cases} 1.64 & (T \ll \theta) \\ \theta/T & (T \gg \theta) \end{cases}$$

$$I_2(\theta) = \int_0^{\theta/T} \frac{x^2 dx}{[e^x-1][e^{-x}-1]} \quad \begin{cases} 3.29 & (T \ll \theta) \\ \theta/T & (T \gg \theta) \end{cases}$$

From these expressions we can write the static structure factor in the high and low temperature limit as follows:

For $T \ll \theta$ $S(K) = a(K) + \alpha(K)(3.29A^{\rho}(K)-1.64a(K))(T/\theta)^2 + \ldots$ (2.1.16a)

For $T \gg \theta$ $S(K) = a(K) + \alpha(K)(A^{\rho}(K)-a(K))(T/\theta)+\alpha^2(K)(1-A^{\rho}(K))(\frac{T}{\theta})^2$ (2.1.16b)

The factor $(1-A^{\rho}(K))$ in eq. 2.1.16b is usually small so we can neglect the quadratic temperature dependence term at high temperature in most cases.

We therefore conclude, after substitution of these expressions into eq. 2.1.6 or eq. 2.1.15 that the diffraction model predicts a resistivity varying like T^2 at low temperatures and linear in T at high temperatures.

The sign of the temperature coefficient of resistivity $\alpha = \frac{1}{\rho}\frac{d\rho}{dT}$ at high temperature depends whether $a(2k_f)$ is greater or less than $A^{\rho}(2k_f)$ or, in other words, it depends on the position of $2k_f$ with respect to the position of the main peak in the structure factor k_p. When $2k_f$ is close to k_p, $a(2k_f)$ is large and α is negative whereas

when $2k_f$ is far from the main peak in the structure factor, α is positive.

In this thesis we are primarily interested in the high temperature region ($T > \theta$) where the resistivity varies linearly with temperature due to thermal broadening.

II.2 Topological Relaxation

Topological relaxation and the concept of free volume are closely related. We usually associate the increase in the topological short range order with a consequent reduction in the free volume content. The theory of free volume was originally developed for liquids[21]. The free volume was defined as the "macroscopic" excess volume of the liquid (in the sense discussed by Egami et al.[22]), compared to the extrapolated volume of the solid. This free volume is distributed over the whole system in the form of vacant spaces between the atoms. The repulsive part of the interatomic potential was assumed to be almost hard sphere like and the free volume was written as:

$$v_f = \bar{\Omega} - \Omega_0 \qquad (2.2.1)$$

where $\bar{\Omega}$ is the average atomic volume and Ω_0 , the atomic volume at ideal close packing. The theory was then applied to amorphous solids by Spaepen and his co-workers who described the structural relaxation in metallic glasses in the following way: In a relaxation event, the atoms at a relaxation site collapse at about a local free volume fluctuation. The collapsed volume is transferred permanently to the specimen surface through many individual atomic rearrangements. Following this event, the total free volume is reduced and the viscosity increases. The viscosity can be expressed in the theory by:

$$\eta = \eta_0(T)e^{\gamma v^*/v_f} \qquad (2.2.2)$$

where v^* is the critical free volume fluctuation for an atomic jump producing flow, γ is a geometrical factor close to 1 and η_0 is a structure independent factor.)

A. The Kelton-Spaepen Approach

Kelton et al. studied the kinetics of isothermal structural relaxation through changes in the electrical resistivity[23]. Their understanding of the behavior of the resistivity is based on the experimental observation that the viscosity for Pd-Si-V amorphous alloys increases linearly as a function of annealing time ($\dot{\eta}$ is a constant depending only on temperature). Using eq. 2.2.2 we can write:

$$\eta_0 e^{\gamma v^*/v_f(t)} = \dot{\eta} t + \eta_0 e^{\gamma v^*/v_f(0)}$$

which can be inverted to give

$$\frac{v_f(t)}{v_f(0)} = \frac{\gamma v^*/v_f(0)}{\ell n(\frac{\dot{\eta}}{\eta_0} t\, e^{-\gamma v^*/v_f(0)} + 1) + \gamma v^*/v_f(0)} \qquad (2.2.3)$$

According to eq. 2.1.15, the change in the electrical resistivity can be directly related to the change in the structure factor evaluated at $2k_f$. Ashcroft and Langreth[24] found that the Percus-Yevick hard-sphere model is a suitable approximation to the main peak of the structure factor. In this model the alloy is characterized by a packing fraction parameter $\xi = \Omega_h/\Omega$ where Ω_h is the hard sphere volume. The peak height reduction and broadening of the structure factor with temperature can be approximated in the Percus-Yevick model by allowing for a change in packing fraction with temperature. Kelton et al.[23] used this model to describe the structural relaxation in metallic glasses. Let us expand the Percus-Yevick structure factor in a Taylor series:

$$S(K,\xi) = S(K,\xi_0) + \left.\frac{\partial S}{\partial \xi}\right|_{\xi_0} \Delta\xi + \ldots$$

From this, using the preceding discussion, we can write

$$\Delta\rho \propto \left.\frac{\partial S}{\partial \xi}\right|_{\xi_0} \Omega_h \left(\frac{1}{\bar{\Omega}(t)} - \frac{1}{\bar{\Omega}(t=0)}\right)$$

and by using equation 2.2.1

$$\Delta\rho \propto \left.\frac{\partial S}{\partial \xi}\right|_{\xi_0} \frac{\Omega_h v_f(o)}{\Omega_o} \left(1 - \frac{v_f(t)}{v_f(o)}\right) \qquad (v_f(o) << \Omega_o) \qquad (2.2.4)$$

With eq. 2.2.3 and eq. 2.2.4, we can fit the electrical resistivity change with three parameters: a prefactor, $\dot{n} / n_o$ and $\gamma v^*/v_f(0)$. The sign of the resistivity change depends on the sign of $\left.\frac{\partial S(2k_f)}{\partial \xi}\right|_{\xi_0}$. When k_f is close to the main peak in the structure factor, α is negative and the resistivity increases upon relaxation. When $2k_f$ is far from the main peak, α is positive and the resistivity decreases with topological relaxation. Fig. 2.2.1 shows a schematic plot of the structure factor in the as-quenched state, relaxed, and at high temperature. Fig. 2.2.2 shows a fit to the electrical resistivity for an $(Mo_{0.6}Ru_{0.4})_{78}B_{22}$ amorphous alloy using eq. 2.2.4. Even if it has not been proven that the viscosity increases linearly with time during isothermal annealing in this specific alloy, the fit is very good at low temperature (450°C and 500°C), but becomes worse and even impossible as we raise the temperature to 600°C. We will show later that chemical relaxation and phase segregation is responsible for this behavior at high temperature.

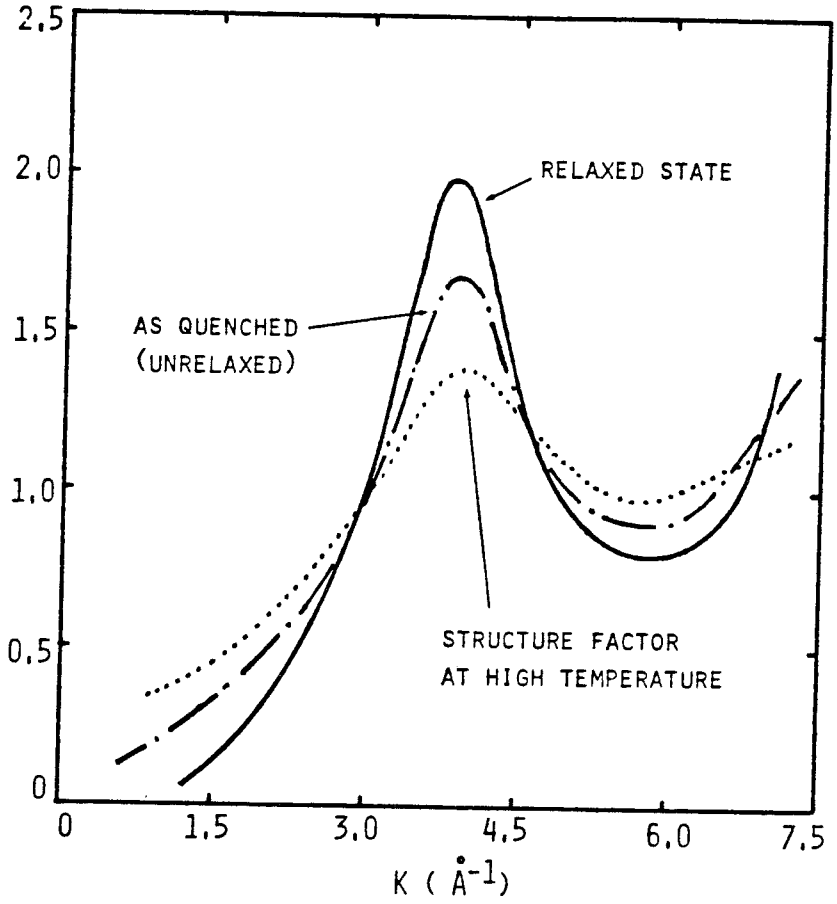

Fig. 2.2.1

Schematic illustration of the first peak of the structure factor S(Q) in the as quenched state, relaxed state and at high temperature.

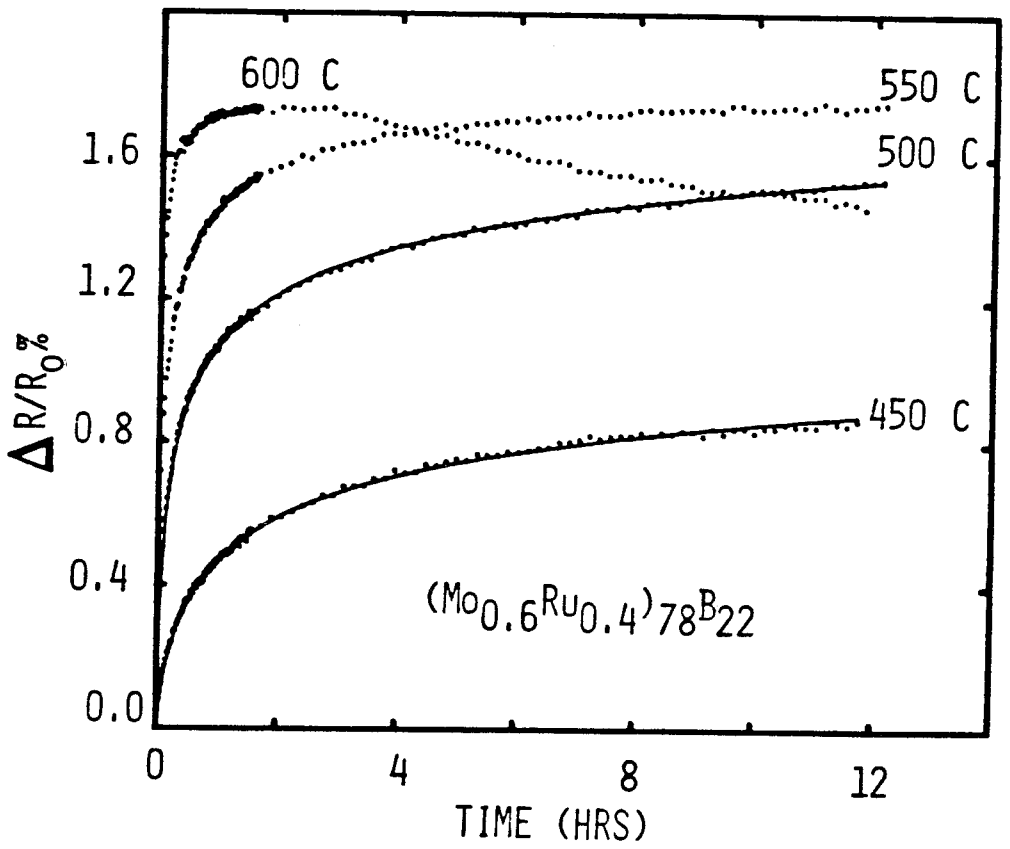

Fig. 2.2.2

Relative change in resistivity as a function of annealing time at various temperatures for $(Mo_{0.6}Ru_{0.4})_{78}B_{22}$ glasses. The solid line is a fit to the Kelton-Spaepen theory of structural relaxation.

B. Egami's Model for Structural Relaxation

Egami et al.[23,25] discussed the short-comings of the macroscopic free volume theory when applied to metallic glasses and proposed instead a microscopic model for structural relaxation in those amorphous alloys. They introduced several local parameters to describe the local atomic structure. Among the most important is the local hydrostatic stress parameter defined as:

$$p_i = \frac{1}{6\Omega_i} \sum_j \left.\frac{\partial \phi}{\partial r}\right|_{r_{ij}} r_{ij} \qquad (2.2.5)$$

Where Ω_i is the local atomic volume and $\phi(r)$ is the inter-atomic potential. Because of the quasi harmonicity of this potential in an amorphous metal both positive and negative density fluctuations are present. The regions in tensile stress are called n-type and are free-volume-like, whereas the regions in compressive stress are called p-type and can be viewed as anti-free volume-like. The n and p type local density fluctuation contribute to the total volume in an opposite way. In this picture, structural relaxation results from the recombination of the n-p pairs. Even if the microscopic free volume, defined as $\langle(\Omega_i - \bar{\Omega})^2\rangle$, is greatly affected by this process, the macroscopic free volume or the total volume is only changing slightly as a result of the anharmonicity of the interatomic potential. Using a computer model containing 2067 atoms for the amorphous structure, Srolovitz, Egami and Vitek[26] simulated the effect of structural relaxation on the radial distribution function (RDF) by calculating the ΔRDF when one fixes the origin on each atom in the model and then excludes all the sites having the largest

tensile and compressive stress. They found good agreement between their model and an experimental Δ RDF measured on an amorphous $Fe_{40}Ni_{40}P_{16}B_6$ alloy. To a good approximation, the local RDF centered on atoms with hydrostatic stress p can be expressed as[26]:

$$G_p(r) = G_o(r + \gamma p) \tag{2.2.6}$$

where γ is a constant and $G_o(r)$ is the RDF for atoms with p=0. G(r) is related to the g(r) defined previously in eq. 2.1.7 by:

$$G(r) = 4\pi r \frac{N}{V} (g(r)-1) \tag{2.2.7}$$

The effect of the local density fluctuation is then to shift the local RDF by an amount proportional to p. If we expand 2.2.6 in a Taylor series around p=0,

$$G_o(r + \gamma p) = G_o(r) + \frac{\partial G_o}{\partial r} \gamma p + \frac{1}{2!} \frac{\partial^2 G_o}{\partial r^2} \gamma^2 p^2$$

the total RDF $\langle G_p(r)\rangle = \int G_o(r + \gamma p)N(p)dp$ (where N(p) is the normalized distribution of the hydrostatic stress parameter) becomes:

$$\langle G_p(r)\rangle = G_o(r) + \frac{1}{2} \gamma^2 \left(\frac{\partial^2 G_o}{\partial r^2} \right) \langle p^2 \rangle \tag{2.2.8}$$

since $\int pN(p)dp=0$. Experimentally, it is often observed that the effect of structural relaxation is to sharpen the peaks of the RDF without shifting them. For this reason Egami et al. choose to interpret the changes in the RDF solely on the basis of the relaxation

of the density fluctuation $\langle p^2 \rangle$ and write:

$$\Delta RDF = \frac{\gamma^2}{2} \frac{\partial^2 G_o(r)}{\partial r^2} \Delta\langle p^2 \rangle \qquad (2.2.9)$$

where $\Delta\langle p^2 \rangle = \langle p^2 \rangle_{annealed} - \langle p^2 \rangle_{as\ quenched}$

The success of Egami's model is that it predicts correctly the small change in the total density of the amorphous alloy during structural relaxation and it predicts a ΔRDF in agreement with the experiment.

C. The Allia-Turtelli Theory

Based on the previous microscopic model for structural relaxation, Allia et al.[27] proposed a correlation between the resistivity and the density fluctuation $\langle p^2 \rangle$ using the Ziman formalism. From eq. 2.2.7 and eq. 2.1.7 we can write:

$$\langle a_p(K) \rangle = 1 + \frac{1}{K} \int_o^\infty \langle G_p(r) \rangle \sin(Kr)\, dr \qquad (2.2.10)$$

and by substitution of 2.2.8 into 2.2.10, the equation after integrating twice by parts becomes:

$$\langle a_p(K) \rangle = a_o(K) + \frac{1}{2} \gamma^2 K^2 (1 - a_o(K)) \langle p^2 \rangle$$

where $$a_o(K) = 1 + \frac{1}{K} \int_o^\infty G_o(r) \sin(Kr)\, dr \qquad (2.2.11)$$

Using expression 2.1.16b and eq. 2.1.15 for the resistivity at high temperature we find:

$$\rho(T) \propto \langle a_p(2k_f) \rangle + \alpha(2k_f)(A^\rho(2k_f) - \langle a_p(2k_f) \rangle)\frac{T}{\theta} \qquad (2.2.12)$$

and therefore the change in resistivity and coefficient of the

resistivity at a fixed temperature due to relaxation, can be written as:

$$\Delta\rho \propto \frac{1}{2}\gamma^2(2k_f)^2(1 - \alpha\frac{T}{\theta})(1 - a_0(2k_f))\ \Delta\langle p^2\rangle \qquad (2.2.13)$$

and $$\Delta\alpha \equiv \Delta\left(\frac{1}{\rho}\frac{d\rho}{dT}\right) \propto \frac{\gamma^2(2k_f)^2\alpha}{2\rho_0\,\theta}\,(1 - a_0(2k_f))\ \Delta\langle p^2\rangle$$

where $\rho_0 = a_0(2k_f) + \alpha\,(A^{\rho}(2k_f) - a_0(2k_f))\,\frac{T}{\theta}$ and $\Delta\langle p^2\rangle$ has the same meaning as in eq. 2.2.9 . We see in eq. 2.2.13 that $\Delta\rho$ and $\Delta\alpha$ have opposite signs. When $2k_f$ is close to k_p (which corresponds to the maximum of the structure factor), $a_0(2k_f)>1$ and the resistivity increases upon structural relaxation since $\Delta\langle p^2\rangle <0$. The temperature coefficient of the resistivity on the other hand decreases, in this case, with structural relaxation. These observations seem to agree with experimental measurements[27,28].

D. Phenomenological Approach Based on the Cohen and Grest Theory of the Glass Transition

Among the several theories which have been proposed to explain the liquid-glass transition, one of the most extensive is the model of Cohen and Grest[29]. The theory is based on the existence in dense liquids and glasses of a well defined cellular structure which persists on a time scale comparable to the typical time for atomic motion within the cell. These cells are equivalent to the Voronoi Polyhedra in a dense random packing model of hard spheres. They assume that the local free energy of a cell f(v) depends only on its volume,

and write:

$$f(v) = f_0 + \frac{1}{2} K (v - v_0)^2 \qquad v < v_c$$
$$= f_0 + \frac{1}{2} K (v - v_0)^2 + \xi (v - v_c) \qquad v > v_c$$

When $v<v_c$ the cells are called solid-like and when $v>v_c$, they are called liquid-like. The free volume of a cell is defined as $v_f = v-v_c$. The linearity of f(v) for $v>v_c$ implies that free exchange of free volume can take place between liquid-like nearest neighbor cells. If P(v) is the probability that a cell has a volume v, the probability that a given cell is liquid-like is:

$$p = \int_{v_c}^{\infty} P(v)\, dv \qquad (2.2.14)$$

Furthermore, they define a percolation problem where p_c is the critical liquid-like cell concentration, above which there exists an infinite liquid-like cluster. They found that the "equilibrium" fraction of the liquid-like cells p, as a function of temperature, undergoes a discontinuous change at a temperature T_p. This discontinuity is taken to be evidence of an underlying equilibrium glass transition. This transition is never seen experimentally because of kinetic effects. At a temperature called the experimental glass transition, the relaxation time of the system becomes comparable to the time of measurement and the system falls out of complete thermodynamic equilibrium. T_p is usually some 20^o below T_g. The glass is therefore characterized by a frozen fraction of liquid-like cell p_{froz} which relaxation toward the equilibrium fraction $p_{eq}(T)$ upon annealing below T_g.

In this picture, a glass can be viewed as a binary alloy in which the two species are respectively the solid-like and the liquid-like cells. Using the Faber-Ziman formalism[16] for the resistivity of binary simple liquid metals, it is straightforward to show that the interference function defined in eq. 2.1.3 can be written as:

$$I(K) = N\left|U_K\right|^2 = u_s^2 \frac{N_s}{N} a_{ss}(K) + u_\ell^2 \frac{N_\ell}{N} a_{\ell\ell}(K) + I_{s\ell}(K) \quad (2.2.15)$$

where $u_s(K)$ and $u_\ell(K)$ are respectively the Fourier transform of the pseudopotential associated with an atom in a solid-like cell and in a liquid-like cell. $N_s/N = (1-p)$ and $N_\ell/N = p$ are the fractions of solid-like and liquid-like cells, $a_{ss}(K)$ and $a_{\ell\ell}(K)$ are the corresponding partial structure factors, and $I_{s\ell}(K)$ is the interference function between a solid-like and a liquid-like cell. For a segregated system (i.e. a system in which the solid-like cells and the liquid-like cells are clustered), $I_{s\ell}$ is non negligible only at small K values i.e. for $K \ll 2\pi/R$ where R is the average cluster size. Since the resistivity is proportional to the structure factor evaluated at $2k_f$, $I_{s\ell}(2k_f)$ will make a negligible contribution to the resistivity. For a segregated system, therefore, eq. 2.1.15 and 2.2.15 give:

$$\rho \propto u_s^2 a_{ss}(2k_f) + (u_\ell^2 a_{\ell\ell}(2k_f) - u_s^2 a_{ss}(2k_f))\, p$$

or
$$\frac{\Delta\rho}{\rho_0} \propto \frac{1}{\rho_0} (u_\ell^2 a_{\ell\ell}(2k_f) - u_s^2 a_{ss}(2k_f))\, \Delta p \quad (2.2.16)$$

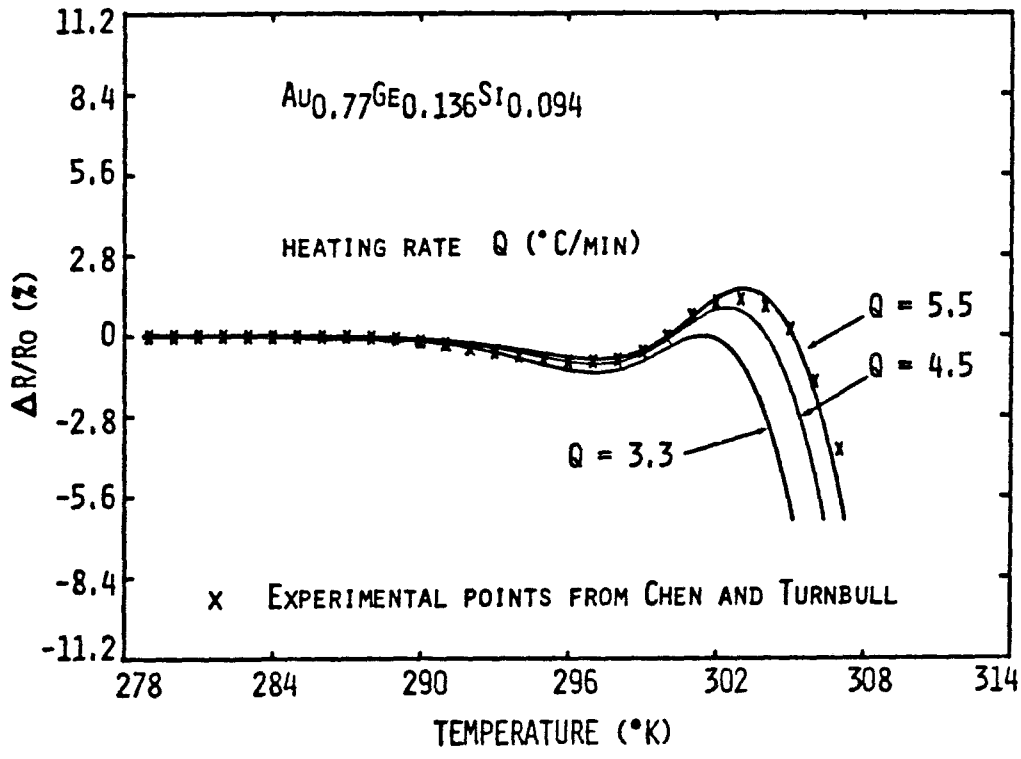

Fig. 2.2.3

Relative change in resistivity for $Au_{0.77}Ge_{0.136}Si_{0.094}$ alloys calculated for different heating rates together with the experimental data of Chen and Turnbull (ref. 31).

The sign of $\Delta\rho$ during isothermal annealing depends on the sign of the expression in parentheses in eq. 2.2.16. When $2k_f$ is close to k_p, $a_{\ell\ell}(2k_f) < a_{ss}(2k_f)$ and the resistivity increases with structural relaxation since $\Delta p<0$. When $a_{\ell\ell}(2k_f) > a_{ss}(2k_f)$ equation 2.2.16 agrees with our intuitive feeling that an atom near an interface between a solid-like and a liquid-like cluster will scatter the electrons more effectively in the liquid-like phase than in the solid-like phase. In that case this approach is similar to Tsuei's model[30] which considered a disordered solid as a structure with a highly developed short range order containing, however, some disordered sites, (the liquid-like cells) which are considered to be scattering centers for the electrons.

Fig. 2.2.3 shows a calculated resistivity curve using eq. 2.2.16 for a $Au_{0.77}Ge_{0.136}Si_{0.094}$ amorphous alloy together with the experimental data of Chen and Turnbull[31]. In calculating $\Delta\rho/\rho_0$ we assume that the fraction of liquid-like cells relaxes towards its equilibrium value $p_{eg}(T)$ given by the theory of Cohen and Grest with a single time constant $\tau(T)$ which scales with the viscosity:

$$\frac{dp}{dt} = - \frac{(p - p_{eq}(T))}{\tau(T)}$$

where

$$\tau(T) = \tau_0 \exp(v_m/v_f)$$

$$= 10^{-10} \exp(1360/(T - 241.3))$$

In order to take into account the contribution of crystallization we assume that the equilibrium fraction of liquid-like cells not crystallized at a time t follows a Johnson-Mehl-Avrami equation[32].

$$(1-X)P_{eq}(T) = P_{eq}(T) \exp\ (-\ (kt)^n)$$

where $$k(T) = k_o \exp\ (-\ \Delta E/kT)$$

For Au-Ge-Si we have T_p = 280K and T_g = 295K. All the other parameters used in the calculation can be found in references 29, 31, and 33. The resistivity values of Chen and Turnbull are the average values taken from several measurements. This approach is particularly suitable for kinetic studies since it relates the resistivity to only one simple parameter: the number of liquid-like cells which can be considered as defects in the amorphous structure.

II.3 Chemical Relaxation

The broad field of chemical relaxation in alloys, which includes phenomena like ordering, coarsening or phase segregation, spinodal decomposition and nucleation, is of great practical as well as theoretical interest. In its simplest form these phenomena occur when an AB alloy (such as AlZn or CuAu) is quenched from a high temperature, where the system is chemically homogenous to a temperature $T<T_c$ (where T_c is the critical temperature for phase separation or ordering). Immediately after the quench, which is ideally instantaneous, the system is thermodynamically unstable and, therefore, will undergo a process of phase transformation if the atomic mobility is large enough. The same phenomenon also occurs obviously, for an homogenous system which has been quenched originally to a temperature where diffusion is prohibited and subsequently annealed at high temperature. In this case the term chemical relaxation is more appropriate. It is obviously out of the scope of this chapter to discuss in detail all of these phenomena, therefore, we will concentrate mainly on the problem of phase segregation. A good review of some recent results on the kinetics of phase segregation can be found in reference 34. The term "phase segregation" embraces phase segregation of an amorphous phase inside another amorphous phase, formation of a crystalline phase inside an amorphous phase or a crystalline phase inside another crystalline phase. In this research we are primarily interested by the first case: Phase segregation of an amorphous phase inside another amorphous phase. However, most studies, especially those on spinodal decomposition, were performed using crystalline phases. Fig. 2.3.1 and

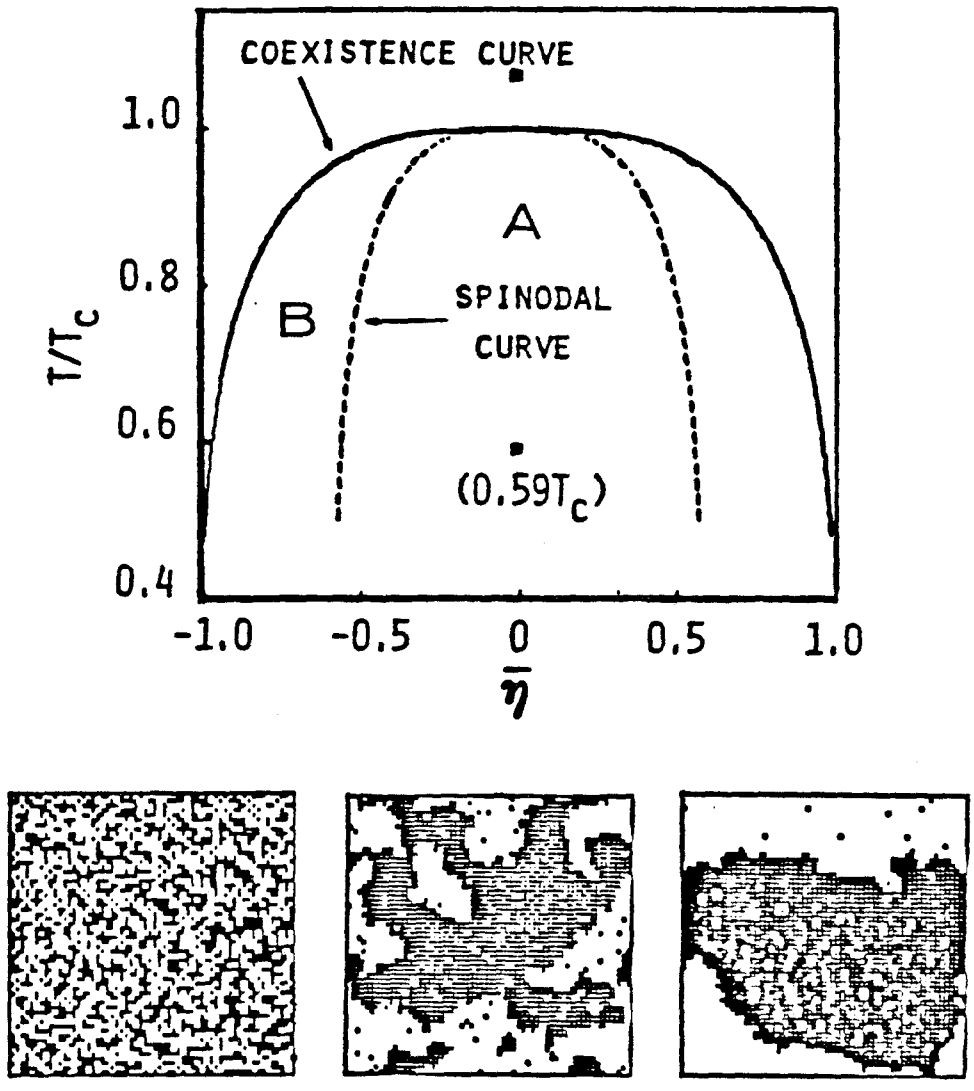

Fig. 2.3.1

Phase diagram for a binary alloy (or the infinite three dimensional Ising model, ref. 36) and the evolution of a high temperature configuration following a quench to a temperature $T = 0.59\ T_c$.

2.3.2 show a computer simulated quench of an Ising model[36] from a temperature above the coexistence curve to a temperature ($T = 0.59T_c$) inside the spinodal region. The alloy is originally at the equiatomic composition. The spinodal curve is defined by the locus of points where the second derivative of the free energy with respect to concentration vanishes. Fig. 2.3.2 shows the evolution with time of the concentration-concentration structure factor during the phase segregation. In the early time, when deviations from uniformity are small, the Cahn-Hilliard[35] linearized theory of spinodal decomposition gives:

$$S(K,t) \approx S(K,0) \exp [2R(K)t]$$
$$R(K) = - MK^2 \left(\frac{\partial^2 f(\bar{c})}{\partial \bar{c}^2} + SK^2 \right) \qquad (2.3.1)$$

where M and S are positive constants respectively related to the diffusion coefficient and the surface tension and c is the average composition of the system. In the spinodal region where $\partial^2 f(\bar{c})/\partial \bar{c}^2 < 0$ (region A is fig. 2.3.1) the system is unstable with respect to long-wavelength fluctuations ($R(K) > 0$). When $\partial^2 f(\bar{c})/\partial \bar{c}^2 > 0$, the metastable region (region B in fig. 2.3.1) the system is stable with respect to small fluctuations but unstable with respect to strong localized fluctuations such as a nucleus, provided an extra activation energy is supplied. This theory predicts the existence of a certain K_{max} (when $\partial^2 f(\bar{c})/\partial \bar{c}^2 < 0$) at which $S(K,t)$ will have its most rapid growth. This describes the initial stages of coarsening but fails to describe the experimental data at all times and, in particular, the shift of $K_{max}(t)$ toward small K values (fig. 2.3.2). Also represented in this figure is $K^3|v(K)|^2$

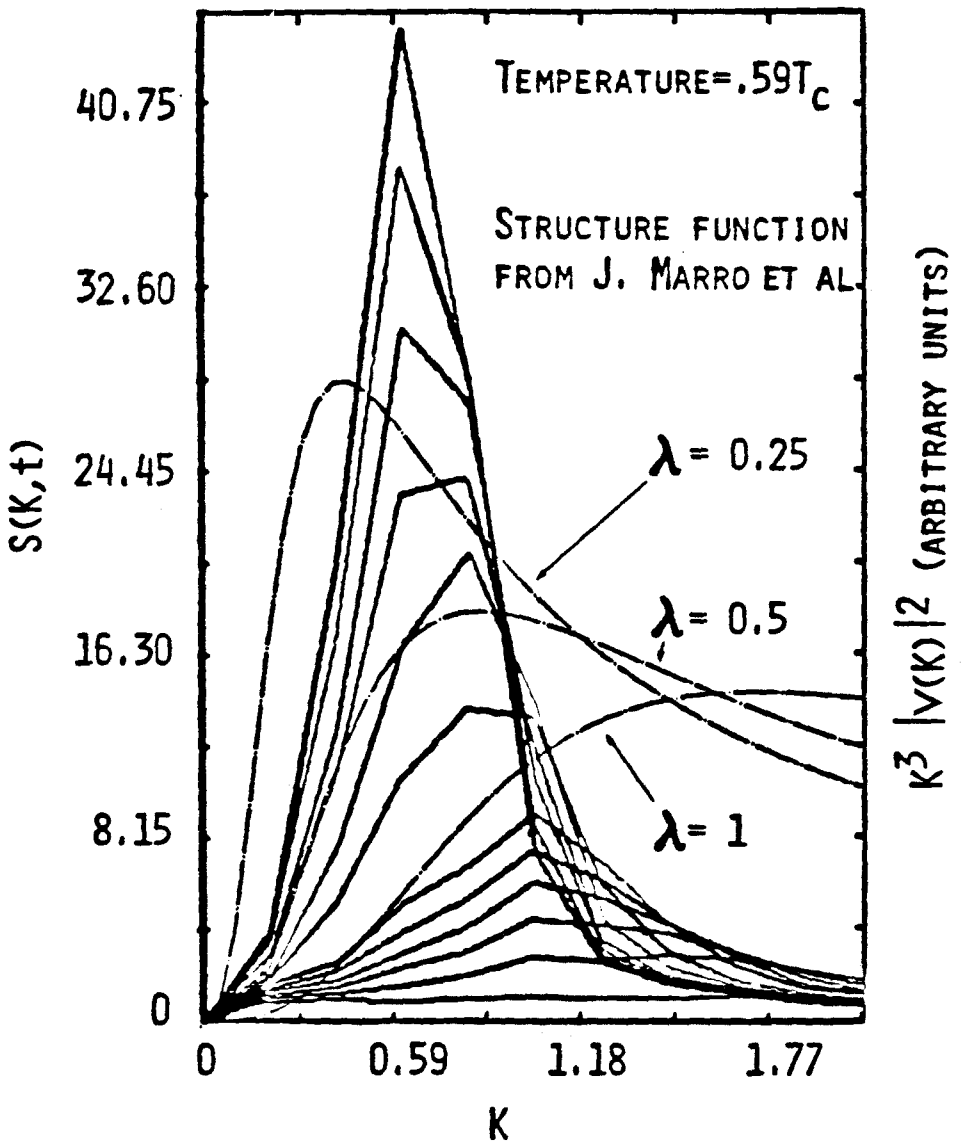

Fig. 2.3.2

Development with time of the structure factor S(K,t) (full line) corresponding to a quench from a temperature above the coexistent curve to a temperature T = 0.59 T_c inside the spinodal region (see fig. 2.3.1) (the data are from ref. 36). Also represented in the figure is the function $K^3|v(K)|^2 = K^3/(1+(K/\lambda)^2)^2$ (dashed lines) for different values of the parameter.

for different screening parameters λ (dashed curve). v(K) is the Fourier transform of a screened Coulomb potential which is given by:

$$v(r) = \frac{Ze^2}{4\pi r} e^{-\lambda r} \qquad v(K) = \frac{Ze^2}{(K^2 + \lambda^2)} \tag{2.3.2}$$

The factor $K^3|v(K)|^2$ was seen in the integrand of equation 2.1.6 for the resistivity. During the phase separation the resistivity goes first to a maximum when the overlap between $K^3|(v(K)|^2$ and S(K,t) is maximum, and then decreases as the peak of the structure factor moves further to the left in fig. 2.3.2.

Such nonlinear behavior in the resistivity is often seen during the age-hardening of supersaturated solid solutions. To my knowledge, one of the first attempts to understand this behavior was due to N.F. Mott[37]. He evoked the wave nature of a beam of electrons and argued that the scattering power of a group of clustered atoms will be greatest when the size of the cluster is comparable to the wave-length associated with the electrons. Typically this latter distance is about four or five inter-atomic distances. Several authors (38-40) afterwards, developed various formalisms to explain this optimum in the resistivity and tried to correlate the resistivity to the size of the scattering entity. I will discuss briefly some of these approaches in the following sections.

A. The Rossiter and Wells Theory

Rossiter and Wells studied the dependence of the electrical resistivity on the chemical short range order in crystalline binary alloy. They introduced a formalism which relates directly the

resistivity to the Cowley short range order parameter. An average potential throughout the lattice is defined as $\bar{u}(r) = c_1 u_1(r) + c_2 u_2(r)$ and the deviation from this average potential can be written as:

$$\begin{aligned} &\text{on a site 1} \qquad v_1 = u_1(r) - \bar{u}(r) = c_2(u_1 - u_2) \\ &\text{on a site 2} \qquad v_2 = u_2(r) - \bar{u}(r) = -c_1(u_1 - u_2) \end{aligned} \tag{2.3.3}$$

The residual resistivity arises from the scattering of nearly free electrons by these fluctuations in the potential and therefore the interference function (eq. 2.1.3) may be written:

$$\begin{aligned} I(K) &= \frac{1}{N} \sum_{i,j} v_i(K) v_j(K) e^{iK\cdot(r_i - r_j)} \\ &= c_1 c_2 (u_1 - u_2)^2 + \sum_{j \neq 0} \langle v_o v_j \rangle e^{iK\cdot R_j} \end{aligned} \tag{2.3.4}$$

where $R_j = r_o - r_j$ and $\langle v_o v_j \rangle$ is an average over all pairs of sites separated by R_j. If we define P_{12}^j as the probability of finding an atom 1 at a distance R_j from an atom 2 we can write:

$$\langle v_o v_j \rangle = c_1 v_1 (P_{21}^j v_2 + (1 - P_{21}^j) v_1) + c_2 v_2 (P_{12}^j v_1 + (1 - P_{12}^j) v_2)$$

$$= c_1 c_2 (u_1 - u_2)^2 (1 - P_{12}^j - P_{21}^j)$$

but since $c_2 P_{12}^j = c_1 P_{21}^j$

$$\langle v_o v_j \rangle = c_1 c_2 (u_1 - u_2)^2 (1 - P_{12}^j / c_1) \equiv c_1 c_2 (u_1 - u_2)^2 \alpha_j$$

where α_j is the Cowley short range order parameter for the atom at

distance R_j from an arbitrary origin. The average of eq. 2.3.4 over all possible directions between K and R_j gives, finally:

$$I(K) = c_1 c_2 (u_1 - u_2)^2 \left(1 + \sum_{j \neq 0} n_j \bar{\alpha}_j \frac{\sin(kR_j)}{KR_j} \right) \qquad (2.3.5)$$

where the summation is now over the n_j atoms is the j^{th} shell and $\bar{\alpha}_j$ is the average value of α_j for this shell. By substitution of 2.3.5 in 2.1.1, the resistivity can be written in terms of the degree of short range order by:

$$\rho = \frac{12\pi\Omega}{he^2 v_f^2} c_1 c_2 \left(\sum_{j=0} n_j \bar{\alpha}_j Y(k_f, R_j) \right) \qquad (2.3.6)$$

where $$Y(k_f, R_j) = \int_0^1 d\left(\frac{K}{2k_f}\right) \left(\frac{K}{2k_f}\right)^3 (u_1 - u_2)^2 \frac{\sin(KR_j)}{KR_j}$$

and $\bar{\alpha}_0 = 1$ by definition

The function $Y(k_f, R_j)$ is a decaying, oscillatory function of R and therefore the predominant contribution to the residual resistivity comes usually from the first term.

$$\rho \approx \rho_0 + \frac{12\pi\Omega}{he^2 v_f^2} c_1 c_2 n_1 \alpha_1 Y(R_1) \qquad (2.3.7)$$

Here, n_1 is the coordination number of the first shell and α_1 is the negative for an ordering process and positive for a clustering process. The value of $Y(R_1)$ can be either positive or negative depending on the value of k_f. In the case of CuTl, which was

discussed briefly in the introduction, the reversible behavior reflects reversible changes in the ordering parameter $\alpha_1(T)$. Both α_1 and $Y(R_1)$ are negative since the resistivity decreases with increasing temperature. For the CuTl system the term $(u_1-u_2)^2$ should be replaced by the difference between the t-matrices of the two elements.

Rossiter and Wells[42] applied their theory to the problem of pre-precipitation during the ageing process and argued that the maximum in the resistivity occurs when the dimensions of the clusters become comparable with the conduction electron mean free path. For larger clusters, the zones could no longer be treated as isolated scatterers and the resistivity decreases because of the reduction in the overall surface scattering at the boundaries of each zone.

Rossiter et al. also discussed the case of spinodal decomposition by replacing the order parameter in eq. 2.3.6 by:

$$\bar{\alpha}_j = \sum_Q a_Q \cos(Q \cdot R_j)$$

where the wavelength of each concentration fluctuation is given by $\lambda = 2\pi/Q$ and the amplitude a_Q is increasing with ageing time. They argued that whether there is Guinier-Preston zone formation or spinodal decomposition the resistivity still exhibits the same general behavior.

B. The Hillel, Edwards and Wilkes Theory

Hillel et al.[43] disagree with Rossiter on the reason for the decrease following the maximum in the resistivity. They considered the theory discussed above, as applied to a crystalline lattice, only

valid in the small zone limit, were the clusters can be assumed to be randomly oriented.

Hillel[44] prefers to attack the problem using a different formalism and proposed that Bragg scattering, due to the microstructure of the zones, leads to the observed increase in resistivity while the decrease, as the Guinier-Preston zones grow in size, is caused by the increasing anisotropy of the relaxation time. Since the microcrystals are coherent with the matrix structure, the Bragg scattering ultimately becomes limited to a vanishingly small fraction of the Fermi surface. In other words, when the number of atoms in the cluster is small, the Bragg peaks are wide and cover the whole Fermi surface, when this number is large, the peaks are extremely narrow and the Bragg scattering decreases.

Hillel considers a very dilute substitutional alloy and uses the elementary transport theory for free electrons to calculate the residual resistivity. As was done in eq. 2.1.5, the square of the scattering matrix element is factorized into structure factor and form factor

$$N|< k'|U|k >|^2 = |u(K)|^2 S(K)$$

where $u(K)$ is the Fourier transform of the difference potential for a single atomic site $u(r) = u_{solute} - u_{solvent}$ and the structure factor is given by:

$$S(K) = \frac{1}{N} \left| \sum_{\substack{\text{solute} \\ \text{atoms}}} e^{iK \cdot r_j} \right|^2 \qquad (2.3.8)$$

Hillel assumes a random arrangement of N_s single solute atoms together

with z clusters, each containing N_c atoms. He neglects all inter-particle interference effects, except when they are within the same zone. All Guinier-Preston zones have internal solute concentration of 100%. Under these conditions, the structure factor becomes:

$$S(K) = N_s/N + z/N\, S_{N_c}(K) \qquad (2.3.9)$$

where $$S_{N_c} = \left| \sum_{\alpha=1}^{N_c} e^{iK\cdot r_\alpha} \right|^2$$

S_{N_c} is the structure factor of a single zone. At this point Hillel[44] uses a simple approximation, which is valid in the early stages of ageing, and consists of taking the spherical average for the cluster's structure factor over all possible orientations $\langle S_{N_c}(K)\rangle = \int \frac{d\Omega}{4\pi} S_{N_c}(K)$. Hillel emphasizes that we cannot expect a decrease in resistivity for large zones in this approximation since the decrease is precisely related to the breakdown of this approximation. If $N_o = N_s + zN_c$ is the total number of solute atoms, equation 2.3.9 can be rewritten as:

$$S(K) = N_o/N + z/N\, (\langle S_{N_c}(K)\rangle - N_c) \qquad (2.3.10)$$

The Debye formula[45] can be used to calculate this average cluster structure factor,

$$\langle S_{N_c}(K)\rangle = N_c + 2\sum_{\ell} \frac{\sin(Kd_\ell)}{Kd_\ell} \qquad (2.3.11)$$

where the summation is over all interatomic distances. Fig. 2.3.3

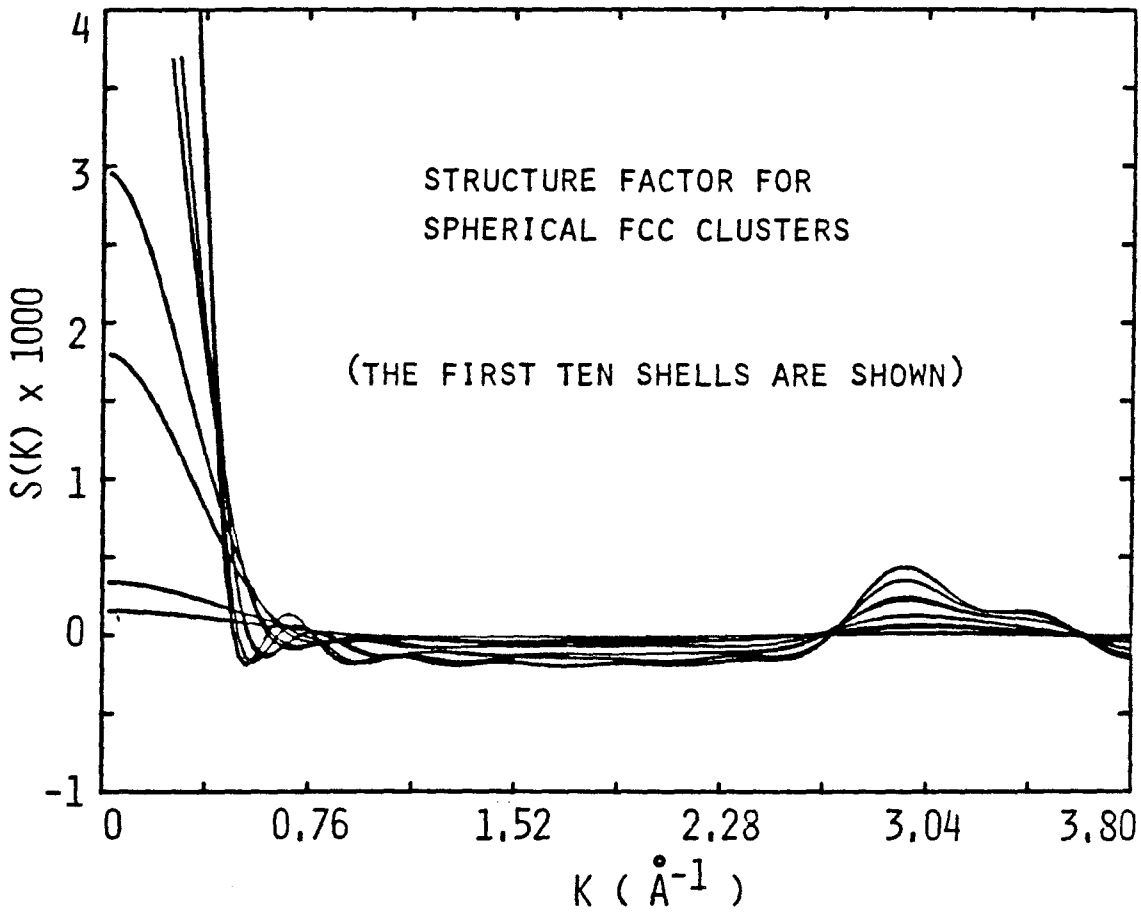

Fig. 2.3.3

Structure factor S(K) for spherical fcc clusters. The hard sphere atomic radius is taken to be 1.3 Å. The first ten shells are represented.

shows the results for an fcc spherical microcrystal. The first 10 shells are represented in the figure and this corresponds to a maximum of about 200 atoms in the cluster. Note the formation of a Bragg peak around $3\mathring{A}^{-1}$.

C. Application to Nucleation in Topologically Random Structures.

When the host lattice is topologically disordered, the previous assumption of randomly oriented Guinier-Preston zones is valid even for very large clusters. This makes the Hillel formalism particularly suitable to treat the problem of nucleation in very dilute topologically random structures. An ideal system would be for instance a binary metallic glass containing a few percent of a ternary element which would have the tendency to segregate at low temperatures.

The electrical resistivity of metallic glasses shows, quite often, anomalous behavior around the crystallization temperature. For example, fig. 2.3.4 represents the normalized resistance trace taken at a heating rate of $10^{o}C/min.$ for a $Pd_{64}Y_{36}$ amorphous alloy. Up to $370^{o}C$, the resistivity is almost constant, it decreases slightly by about 2% near $385^{o}C$ and then increases by about 10%, reaching a maximum around $403^{o}C$.

To understand such behavior let us apply the previous model to the problem of nucleation of fcc microcrystals in a random structure. From eq. 2.1.6, eq. 2.3.10 and 2.3.11 the resistivity during

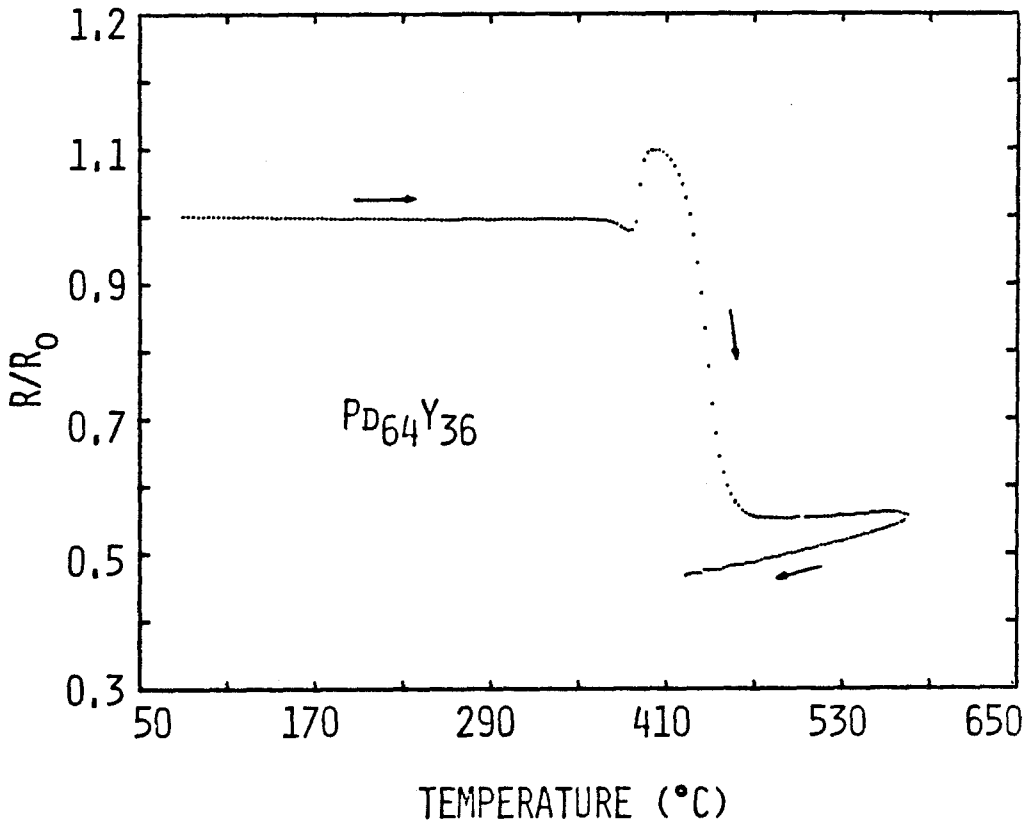

Fig. 2.3.4

Normalized resistance trace taken at a heating rate of 10°C/min. for $Pd_{64}Y_{36}$ metallic glasses.

clustering can be written as:

$$\rho = \frac{12\pi\Omega}{he^2v_f^2}\frac{N_o}{N}\int_0^1 d\left(\frac{K}{2k_f}\right)\left(\frac{K}{2k_f}\right)|(u_1-u_2)|^2\left(1+\frac{2z}{N_o}\sum_{\ell}\frac{\sin(Kd_\ell)}{Kd_\ell}\right) \qquad (2.3.12)$$

where $N_o/N = c$ is the concentration of solute atoms and $z/N_o = r$ is the ratio between the number of clusters and the number of solute atoms. Most of the metallic glasses involve transition metal elements and therefore $(u_1-u_2)^2$ should strictly be the difference between the solute and the solvent t-matrices. However, since we are looking only for qualitative results, we will use a screened Coulomb potential with a same screening parameter, λ , for both constituents. From eq. 2.3.2:

$$(u_1 - u_2)^2 = \left[\frac{\Delta Ze^2}{(K^2+\lambda^2)}\right]^2 \qquad (2.3.13)$$

where ΔZ is the difference in the atomic number. This expression is a monotonically decreasing function of K which takes relatively small values near $K = 2k_f$. Since the major contribution to the integral 2.3.12 comes from the region near $2k_f$, where the function $\langle S_{N_C}(K)\rangle - N_C$ has a peak, the use of a screened Coulomb potential can severely underestimate $\Delta\rho$, as it was pointed out in[43]. Moreover, in topologically random systems, the electron mean free path is usually very small. In order to take into account the finite electronic mean free path, we can apply the Pippard-Ziman approximation which consists in using a lower cut-off in the integral 2.3.12 . Assuming a Gaussian probability distribution for the electron mean free path, we can

replace eq. 2.3.12 by:

$$\rho \propto \int_0^{2k_f} \frac{1}{\sigma\sqrt{2\pi}} \exp\left(-\frac{(K - K_c)^2}{2\sigma^2}\right) \left\{ \int_K^{2k_f} F(k)dk \right\} dK \qquad (2.3.14)$$

$K_c = 2\pi/\ell$ where ℓ is the average electronic mean free path and F(k) is the integrand of eq. 2.3.12 . Through integrating by parts, eq. 2.3.14 can be rewritten as:

$$\rho \propto \int_0^{2k_f} H(K)F(K)dK$$

where $$H(K) = 1/2 + 1/2 \text{ erf } ((K - K_c)/\sqrt{2}\sigma) \qquad K > K_c$$

$$= 1/2 - 1/2 \text{ erf } ((K - K_c)/\sqrt{2}\sigma) \qquad K < K_c$$

The excess resistivity can therefore be written as:

$$\Delta\rho = \frac{24\pi\Omega(\Delta Z)^2 e^2}{hv_f^2} \text{ cr} \int_0^1 d\left(\frac{K}{2k_f}\right)\left(\frac{K}{2k_f}\right)^3 \frac{H(K)}{(K^2+\lambda^2)^2} \sum_{\ell} \frac{\sin(Kd_\ell)}{Kd_\ell} \qquad (2.3.15)$$

Fig. 2.3.5 shows the calculated excess resistivity $\Delta\rho/\rho_o$ during the growth of fcc microcrystals in a topologically random structure using eq. 2.3.15 and the parameters given in Table II.3.1

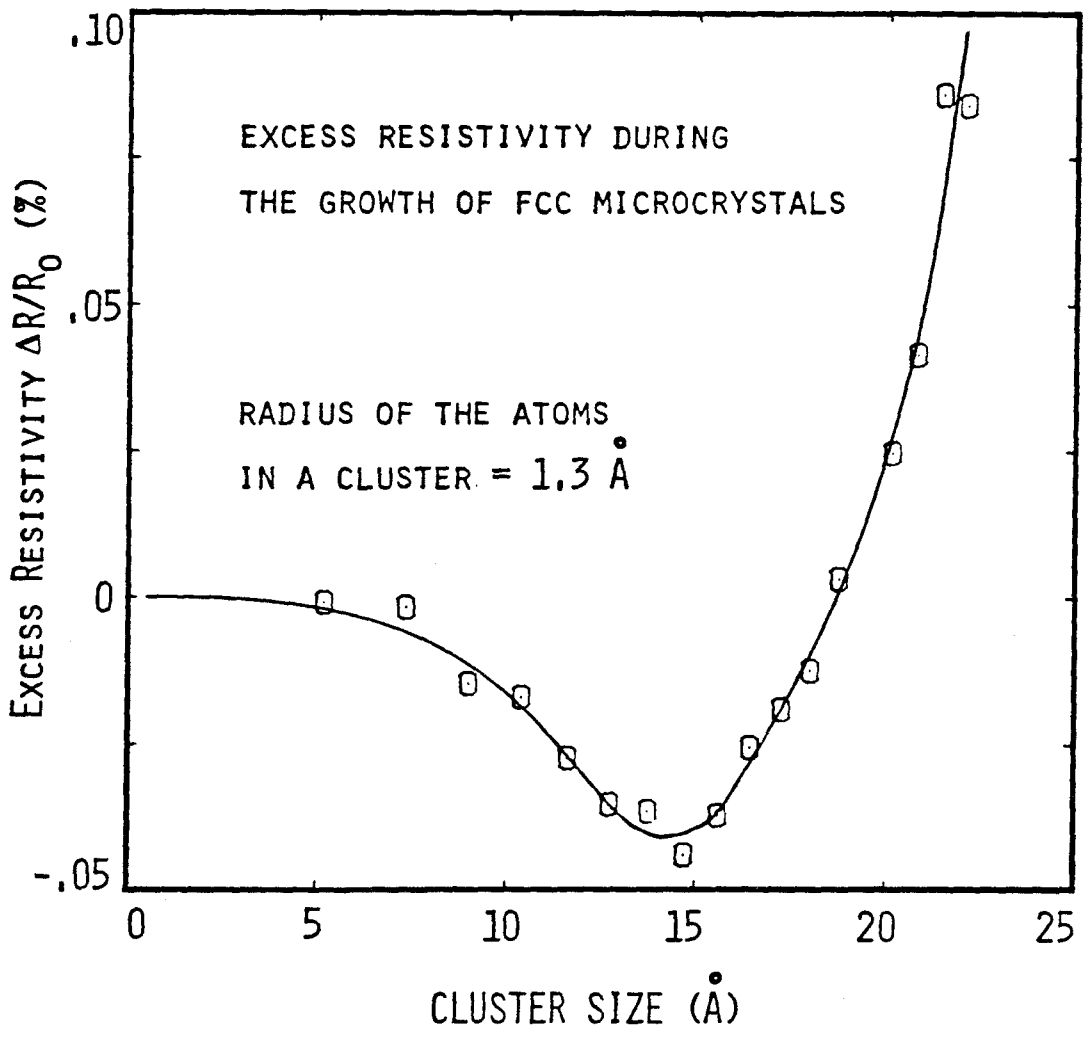

Fig. 2.3.5

Calculated excess resistivity during the growth of fcc microcrystals in a topolotcally random structure. The excess resistivity is plotted vs the size of the zones. All the parameters relevant to this calculation can be found in Table II.3.1 and II.3.2.

TABLE II.3.1

Parameters used for calculating the excess resistivity during the growth of fcc microcrystals in a topologically random structure.

Packing density of the matrix (atoms / Å^3)	=	.06
Number of free electrons per atom	=	1.9
Screening length (Å)	=	0.5
Radius of the atoms in a cluster (Å)	=	1.3
Electronic mean free path (Å)	=	3.0
Root mean square deviation of the distribution (Å)	=	1.5
Number of clusters / Number of solute atoms	=	10^{-4}

Table II.3.2 gives, for a given cluster diameter, the number of atoms in the zone.

TABLE II.3.2

Size and number of atoms for several fcc spherical microcrystals.

# of Shells	# of Atoms	Cluster Diameter (Å)
1	13	5.2
5	79	11.63
10	201	16.44
15	381	20.80
20	495	23.83

Because of the screened Coulomb potential this excess resistivity is very small. For transition metal elements, however, eq. 2.1.15

indicates that we should expect large excess resistivity whenever the difference in the d-phase shift η_2 of the two constituents is large. In the Cu-Zr system, for instance, the phase shifts at the Fermi energy for $Cu_{60}Zr_{40}$ are[46] $\eta_2(Cu)=2.996$ and $\eta_2(Zr)=0.488$ and we will show that, indeed, a relatively large excess resistivity is observed during phase separation in this system.

I would like to emphasize at this point that the previous formalism is also valid for the growth of a topologically random cluster, i.e. in the case of nucleation of an amorphous phase inside another amorphous phase. The only difference is that the width of the Bragg peak near $2k_f$ is larger. The formation and the growth of amorphous zones with boron concentration close to 25% was found, for instance, in $Fe_{40}Ni_{40}B_{20}$ metallic glasses during ageing[47]. An anomalous excess resistivity is associated with the growth of these clusters[48].

C. The Case of Spinodal Decomposition

The previous formalisms described to this point, are mainly concerned with the description of the resistivity during the initial growth of localized fluctuations. They are, therefore, more appropriate for the treatment of nucleation. When an alloy is quenched below the critical temperature for demixing into the spinodal region, however, the early stages of phase separation occurs via long range compositional fluctuations. Binder et al.[49] discussed in detail the behavior of the resistivity in this case using the time dependent concentration-concentration correlation function given from both linear[50] and nonlinear[51] theories of spinodal decomposition

and from computer simulations[36].

Binder uses eq. 2.1.6 for the resistivity together with a screened Coulomb potential (eq. 2.3.13) for the difference in potential between the two constituents. The structure factor S(K,t) given by eq. 2.3.8 is then time dependent. As given before, the linearized theory of spinodal decomposition predicts that[50]:

$$S(K,t) = S(K,0)\exp(-Da^2K^2(K^2 - K_c^2)t) \qquad (2.3.16)$$

where, in terms of the parameters in eq. 2.3.1, $K_c = \left[-\frac{1}{S}\frac{\partial^2 f}{\partial \bar{c}^2}\right]^{\frac{1}{2}}$ is the critical wave number for growth, $D = 2MS/a^2$ is a diffusion constant and, a is the lattice spacing. Let ξ be the correlation length for the fluctuation of concentration above the critical temperature and before the quench (i.e. $g_{cc}(r) = \frac{\beta}{4\pi}\frac{e^{-r/\xi}}{r}$). Therefore, if we assume an infinite cooling rate:

$$S(K,0) = \frac{\beta}{[K^2+\xi^{-2}]} \qquad (2.3.17)$$

Using eq. 2.3.17 and 2.3.16 to calculate the excess resistivity during the early stages of phase separation we obtain when $Kc \ll \lambda$, K_f, $1/\xi$ the following results:

$$\Delta\rho(t) - \Delta\rho(0) = \frac{3\Omega(\Delta Z)^2e^2}{hv_f^2(2k_f)^4\lambda^4}\pi^{3/2}\beta\xi^2K_c^2\exp(\gamma t)\,\mathrm{erf}(\gamma t) \qquad (2.3.18)$$

where $\gamma = 1/4Da^2K_c^4 = \frac{M}{2S}\left(\frac{\partial^2 f}{\partial \bar{c}^2}\right)^2$

This equation predicts that the excess resistivity increases linearly with time for small times ($\gamma t \ll 1$). We will see in section IV that

this is actually the case for the Cu-Zr system during the early stage of phase segregation. For larger times the linearized theory of spinodal decomposition fails to describe the experimental S(K,t) and the exponential growth in either S(K,t) or $\Delta\rho$ has to be discarded. In this regime fluctuations interact and macroscopic grains form. The shift in the peak of the structure function with time (fig. 2.3.2) is associated with an increase in the dimensions of the phase separated regions. Binder[49] showed, from a scaling assumption, that the excess resistivity, in this regime, decreases like the inverse mean radius of the precipitated zones

$$\Delta\rho(t) - \Delta\rho(\infty) \propto q_m(t) \propto t^{-1/3}$$

We have seen that, whether we decide to describe the early stage of decomposition via nucleation or spinodal decomposition both can give to an increase in the resistivity. The physical reason for the decrease is more controversial but it is, in any case, associated with the shift of the structure function toward small K values and the increase in the size of the precipitated zones. Using the experimental structure factor obtained from X-ray scattering analysis to calculate the excess resistivity, J. Mimault et al.[52] found a maximum in resistivity only in the case of spinodal decomposition. The reason for this discrepancy can be related to the finite quenching rate in real experiments. These authors actually found in their samples quenched into the nucleation region, small precipitates which were formed almost instantaneously during the quench.

III. EXPERIMENTAL CONSIDERATIONS

The alloys used in this study were prepared by melting the appropriate amounts of the constituent elements on a water cooled silver boat under an argon atmosphere. The purity of the starting materials was better than 99.9%. Ingots, of typically 2 or 3 grams were melted several times to insure homogeneity.

Two quenching techniques were used in this study to prepare amorphous alloys. $Cu_{73}Ti_{27}$, $Pd_{64}Y_{36}$, $Cu_{100-x}Zr_x$ and $(Zr_{1-x}Hf_x)_{62}Ni_{38}$ were obtained in forms of ribbons by the melt-spinning technique[53]. In this technique a jet of molten metal is projected onto a rotating copper wheel turning at approximately 10,000 RPM. The sample in contact with the Cu surface solidifies, then comes off as a ribbon of about 2mm in width, 30um in thickness and several feet in length. The cooling rate achieved by this technique is estimated to be on the order of 10^6K/min. The $(Mo_{0.6}Ru_{0.4})_{100-x}B_x$ and $(Zr_{62}Ni_{38})_{99.8}Fe_{0.2}$ amorphous samples were produced by the Piston and Anvil method[54]. The melted alloy is ejected from a quartz tube in the form of a droplet which is caught between a rapidly moving piston and an anvil whose surfaces are both made of a CuBe alloy. The samples prepared this way were in the form of foils approximately 1cm in diameter and 40um thick.

After preparation, all samples were checked for crystalline inclusion using X-ray diffraction and CuK_α radiations. Samples whose diffraction pattern consisted of a smooth featureless band and no sharp Bragg reflections were considered as amorphous and kept for further studies.

A. The resistivity measurements

The resistivity measurements were done using a standard four point dc method. The samples were either, ribbons of typically 2cm long or, strips cut with a wire saw from an as quenched foil. Hewlett-Packard 6177c Dc current source was used together with a 3490A Hewlett-Packard multimeter to measure the voltage drop across the sample. Typical current and measured voltage were 10mA and 5mV respectively. An error of less than .04% on the normalized resistance can be achieved this way. The digital output of the voltmeter was fed into a PDP 11/23 "Minc" computer which was used to control the experiment. With the help of a D/A output module on the Minc, for each data point, the current was reversed and the voltage averaged in order to eliminate any thermal induced voltage. A real time display of the resistance on the screen of a terminal was provided, and found very useful in determining an appropriate time to quench the sample from a specific state. The temperature of the furnace could also be controlled by the computer. Two different heating modes were often used: constant heating rate (typically 10°C/min.) or constant annealing temperature. With careful adjustment of the feedback parameters in the program, temperature fluctuations could easily be limited to the order of 1%.

For the Mo-Ru-B system, Pt wires were spot-welded on the sample to make the electrical contact. The measurements were performed in a vertical furnace in a slight over-pressure of helium. The chamber was evacuated and back-filled with He several times before the

measurements.

For the other systems a special arrangement has been built in order to facilitate sequential annealing and quenching experiments. A quartz tube going through a vertical furnace is attached to the top of a dewar. The probe can slide freely on a vertical axis inside the quartz tube. A high vacuum valve and an O-ring seal at each end of the tube permits measurements in any type of atmosphere. As before a slight over-pressure of helium is usually employed in this case. Fig. 3.1 shows a picture of the experimental arrangement. The system is particularly suited to measurement of the residual resistivity at low temperature after various annealing performed at high temperature.

The tip of the probe is made out of a single piece of nickel to provide rapid heat transfer. Usually the temperature of the sample reaches its equilibrium value in less than 10 min. The sample sits on quartz slide and pressure contacts are made via a set of four Cu clamps. A Pt-PtRh thermocouple is used to monitor the temperature and resides in a Cu block located at one end of the sample. Mullite rods are used to isolate the wires inside the probe. Because of their zero thermal coefficient of expansion mullite rods are very resistant to thermal shock. Fig. 3.2 shows a picture and a schematic design of the tip of the resistivity probe. A reel on which a long piece of ribbon can be mounted is attached to the end of the probe for annealing purposes. This way, the resistivity can be accurately correlated with other types of measurements like X-ray diffraction.

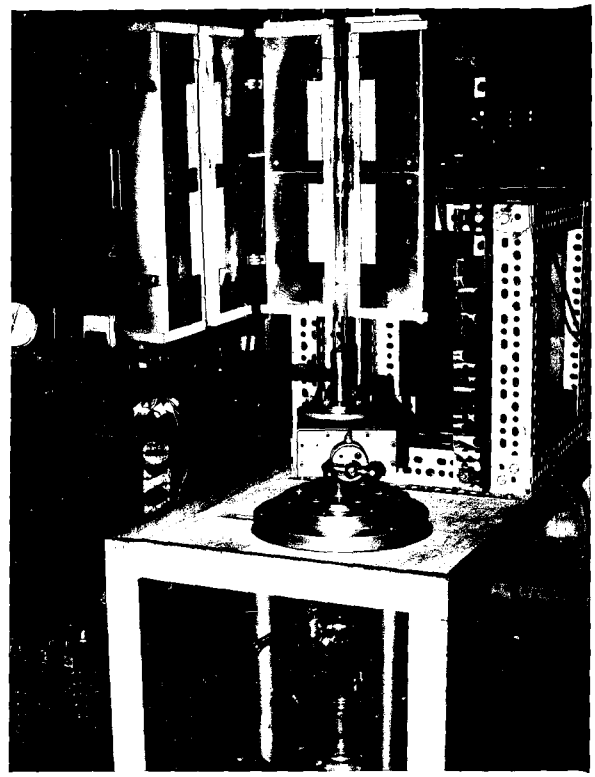

Fig. 3.1

Picture of the experimental setup.

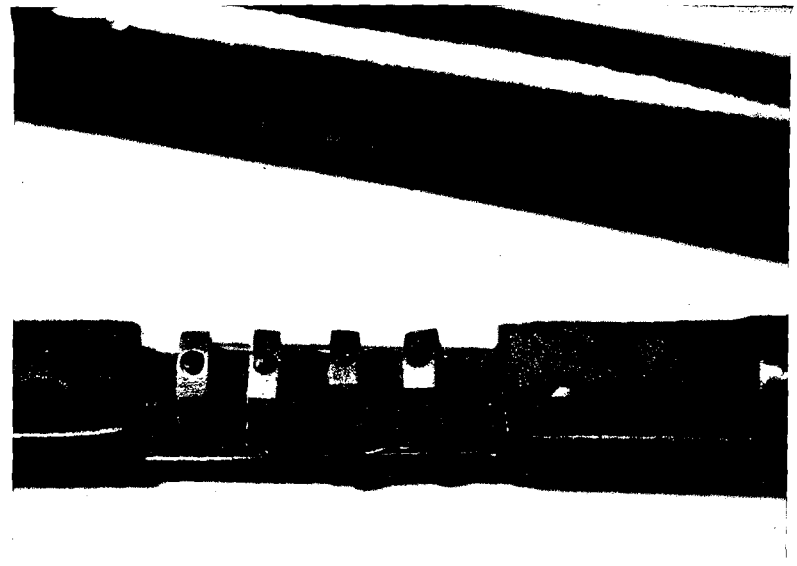

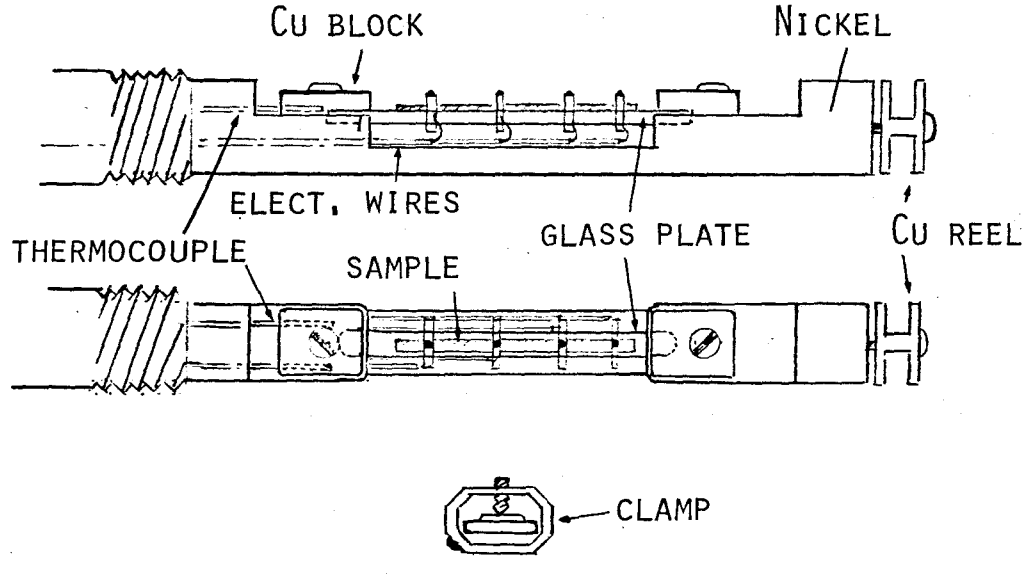

Fig. 3.2

Picture and schematic design of the tip of the resistivity probe.

B. The Structural Measurements

The aim of this research is to understand the behavior of the resistivity in terms of structural changes. Several type of structural investigations were performed. They include: X-ray diffraction, Mossbauer experiments, transmission electron microscopy low temperature superconductivity measurements and finally Differential Scanning Calorimetry (DSC). I will describe briefly in the following each of these experiments and I refer the reader to the experimental section corresponding to each alloy studied in chapter IV for more details.

X-ray diffraction:

In order to calculate the Radial Distribution Function (RDF), detailed X-ray studies were performed on several samples in the reflection geometry using a GE XRD-5 scanning diffractometer or a Phillips Norelco diffractometer. The samples were prepared by stacking several layers of ribbons together with thinned Duco cement on a glass plate. The sample were thick enough to eliminate any scattering from the substrate and to simplify corrections for sample absorption. Molybdenum K_α radiation (λ = 0.7107 Å) was used with a LIF focussing crystal monochromator placed in the diffracted beam to eliminate scattering contributions from other energies. A typical run was done by scanning in angles from 10° to 80° in steps of 0.25° and from 80.5° to 150° in steps of 0.5°. The interference function can be measured, this way, for K values up to 17 $Å^{-1}$. A time interval of 7 min. was chosen for each step in order to reduce the statistical error to less than one percent on the average. A micro-processor controlled

the experiment and stored the recorded intensity digitally. The data obtained were then transfered to a PDP 11/23 computer for analysis. After correction for background, polarization, absorption and Compton scattering, the data are normalized using the "high angle method"(55). Convergence factors ranging from 0.005 to 0.015 were used to calculate the Fourier transform in specific cases. The details of the RDF calculation and the data handling are given in (56).

Mossbauer Experiment:

Mossbauer experiments were performed at room temperature on $(Zr_{62}Ni_{38})_{99.8}Fe_{0.2}$ alloys using a $Co^{57}(Rh)$ source in constant acceleration mode. An old Mossbauer drive was first rebuilt in order to do so. The new electronic feedback system can now achieve an error signal of less than 1% of the reference signal. I would like to emphasize that without the help of Vladimir Matijasevic during the reconstruction of the drive this experiment would probably have not been possible. A Canberra multichannel analyzer was used to collect the data. Fig. 3.3 shows a sketch of the experimental setup and the drive electronics. A complete explanation of the details of the drive can be found in (57).

Amorphous foils quenched by the Piston and Anvil technique were used directly as absorbers. Because of the very small concentrations of iron in the sample, Fe enriched in the Mossbauer isotope (Fe^{57}) was used to make the ingot but even so, collection of a typical spectrum required roughly two weeks. The photons are detected by a $Kr(CO_2)$ proportional counter. Before each measurement, the drive was calibrated using the splitting of the inner two lines of the magnetic hyperfine spectrum of Fe^{57} in metallic Fe. The analysis was performed

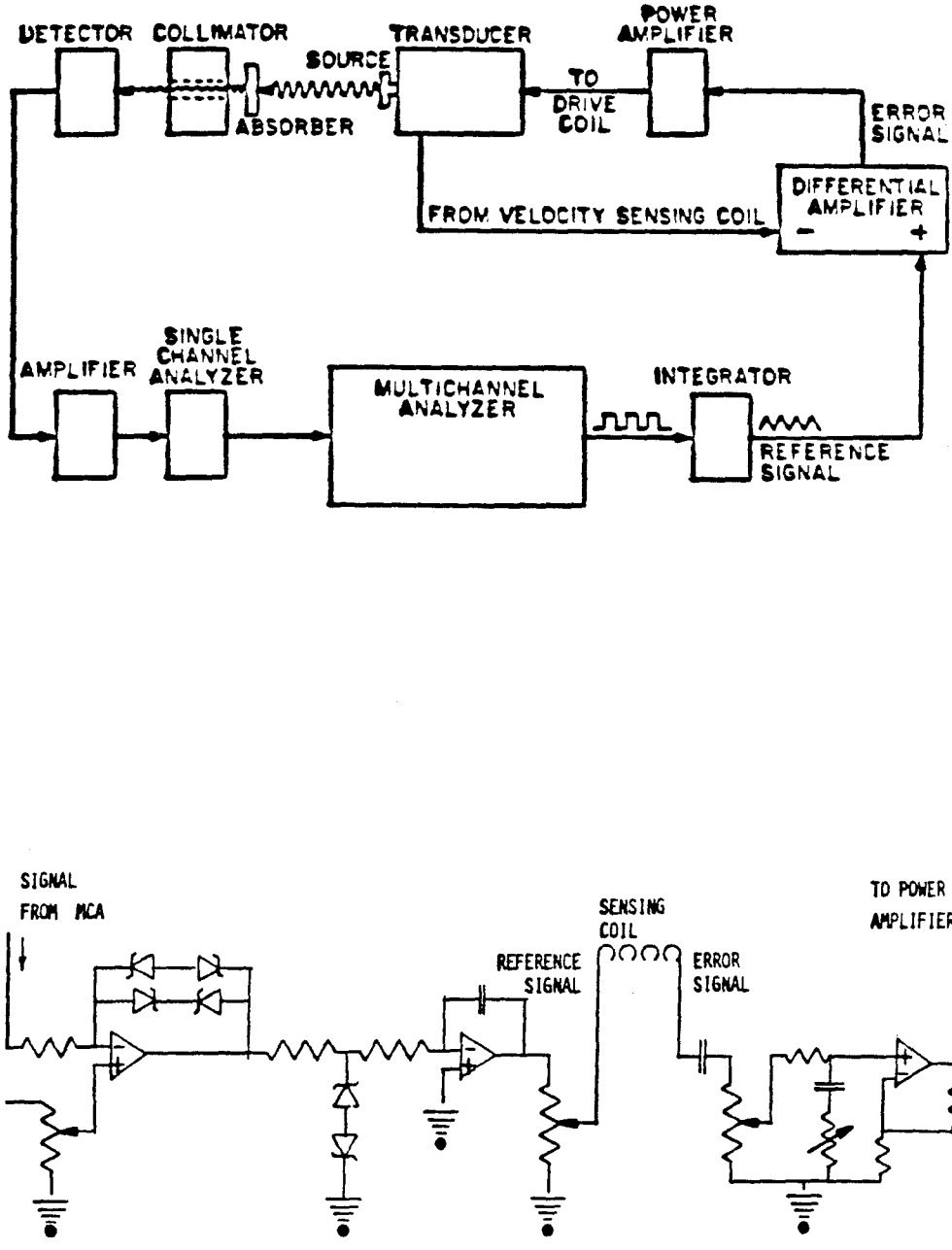

Fig. 3.3

Mossbauer experimental setup and the drive electronics.

by fitting n independent Lorentzian lines with variable width and height, where n is the lowest even number of lines needed to obtain a visually good fit. I am grateful to Carl Unruh for providing me with his program and helping me to perform this analysis.

Transmission Electron Microscopy:

A series of $Cu_{100-x}Zr_x$ and $(Hf_{1-x}Zr_x)_{62}Ni_{38}$ alloys were studied under a transmission electron microscope. For Cu-Zr we used a Siemens ELMISKOP I, whereas for Hf-Zr-Ni a Phillips 300 electron microscope was used. Typical magnification in this last case is 210,000. Prior to the experiment the samples were electro-polished using a 550B Jet Thinning Instrument (South Bay Tech. Inc.) and kept in methanol until the time of the experiment to prevent oxidation. For Cu-Zr a solution of 20% nitric acid, 20% glycerin, 60% methanol was used at -30°C. For Hf-Zr-Ni we used a solution 80% methanol, 20% perchloric acid at -15°C. I am very grateful to Michael Atzmon and Pat Koen for their help with these measurements.

Low temperature superconductivity measurements were performed on $Zr_{62}Ni_{38}$ alloys. In order to measure the upper critical field, a magnetic field produced by a superconducting NbTi solenoid was applied normal to the direction of the current in the sample. The critical field was determined by plotting the resistance of the sample as a function of the applied field. H_{c2} is defined as the mid-point of the resistive transition. The temperature was maintained constant using a pressure control valve over the He bath. The temperature was calculated using the vapor pressure over the liquid. The superconductivity transition temperature was obtained by extrapolating

the graph of H_{c2} versus T to vanishing field. $\left.\frac{dH_{c2}}{dT}\right|_{T_c}$ is just the slope of the curve at $T=T_c$.

DSC measurements were obtained on a commercially available unit (Perkins-Elmer DSC-1) at the Jet Propulsion Laboratory. In these measurements the temperature of the sample is increased at a uniform rate and the heat evolved during various transformations is recorded. A scanning rate of 20K/min. was used.

IV. RESULTS AND DISCUSSIONS

IV.1 $Cu_{100-x}Zr_x$

[This section is essentially an article with the same title by Robert Schulz, Konrad Samwer and W. L. Johnson published in Journal of Non-Crystalline Solids 61 & 62 (1984) 997.]

KINETICS OF PHASE SEPARATION IN $Cu_{50}Zr_{50}$ METALLIC GLASSES

ABSTRACT

An excess resistivity above the usual topological relaxation contribution is seen in $Cu_{50}Zr_{50}$ glassy alloy upon annealing at temperatures far below the glass transition. This excess resistivity is correlated with the appearance of a well defined two step crystallization when the annealed sample is heated through T_c at a rate of 15°C/min. X-ray diffraction suggests that phase separation is taking place and is responsible for this anomalous resistivity behavior. Results from transmission electron microscopy are consistent with this interpretation.

1. INTRODUCTION

Evidence for phase separation in vapor quenched Cu-Zr amorphous alloy has been reported[1]. The phase separation occurred during synthesis and the composition of the two amorphous phases are identifiable with those of ordered crystalline phases $CuZr_2$ and Cu_3Zr. It is believed that the phase separated structure represents a lower free energy state for this noncrystalline alloy system and is a result of the enhanced kinetics found in vapor quench film. The authors also believe that phase separation could be achieved in liquid quenched material by extended annealing at temperatures considerably below T_g and T_c of the two resulting amorphous phases.

Recently Altounian et al.[2] suggest that the equiatomic CuZr does not exist as a single phase in the crystalline state and show in

fact that the crystallization products of the amorphous $Cu_{50}Zr_{50}$ is a mixture of $Cu_{10}Zr_7$ and $CuZr_2$, and not CuZr as it was previously reported[3]. The crystallization temperature of $Cu_{10}Zr_7$ and $CuZr_2$ glassy alloys are respectively ~360°C and ~455°C as measured by the onset of the resistivity drop at T_c for a heating rate of about 10°C/min. Fig. 4.1.1 shows the main and the second band of the radial distribution function for Cu-Zr glasses across the concentration range. Fig. 4.1.2 shows that the average nearest neighbor distance undergoes an abrupt change around the equiatomic composition. If $Cu_{50}Zr_{50}$ phase segregates into Cu rich and Cu poor zones, we should expect the formation of a split first peak in the X-ray pattern during annealing.

In this section we report measurements of electrical resistivity, X-ray diffraction and TEM in order to find phase separation in $Cu_{50}Zr_{50}$ at temperature below 360°C.

2. EXPERIMENTAL

The ingots were prepared by RF induction melting the appropriate amounts of Cu and Zr on a silver boat. Amorphous ribbons were obtained by the melt-spinning technique under reduced helium pressure. The samples were stored under vacuum and used within a few days after preparation.

All measurements of resistivity and X-ray diffraction with annealing temperature have been done on the same ribbon to avoid fluctuation in properties from sample to sample. The kinetics of phase separation appears to be very sensitive to the state of relaxation of the amorphous alloy. The resistivity was measured using

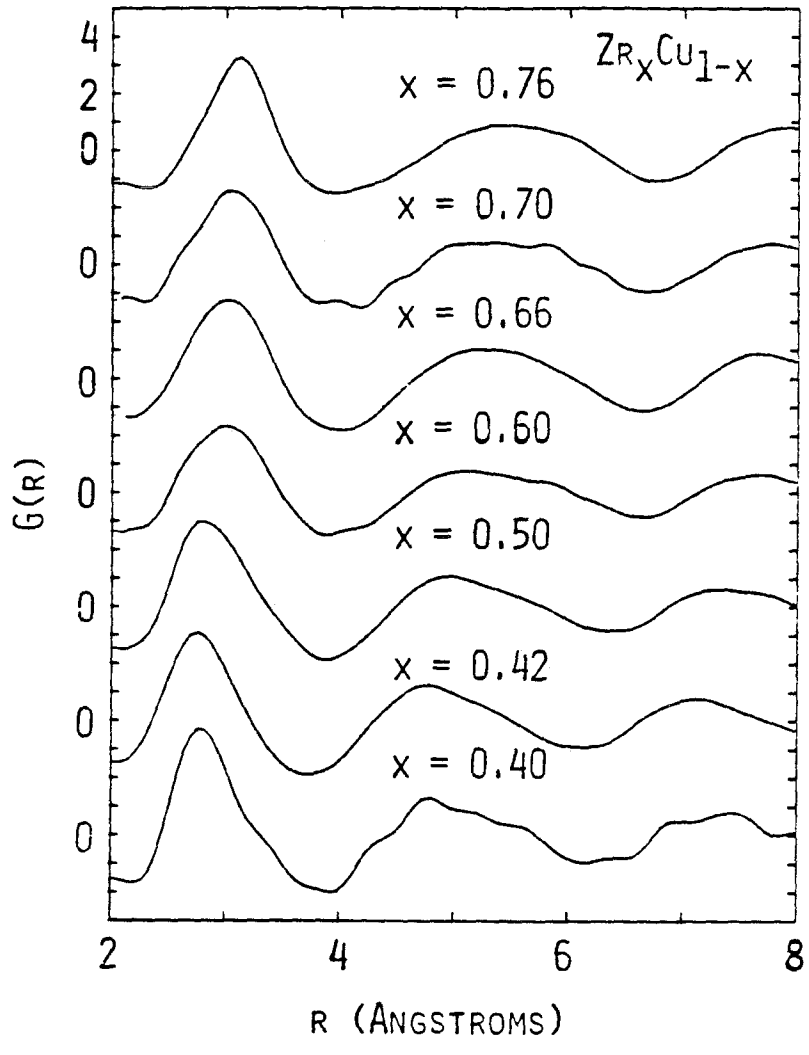

Fig. 4.1.1

The main and the second band of the radial distribution function for the Cu-Zr system across the concentration range.

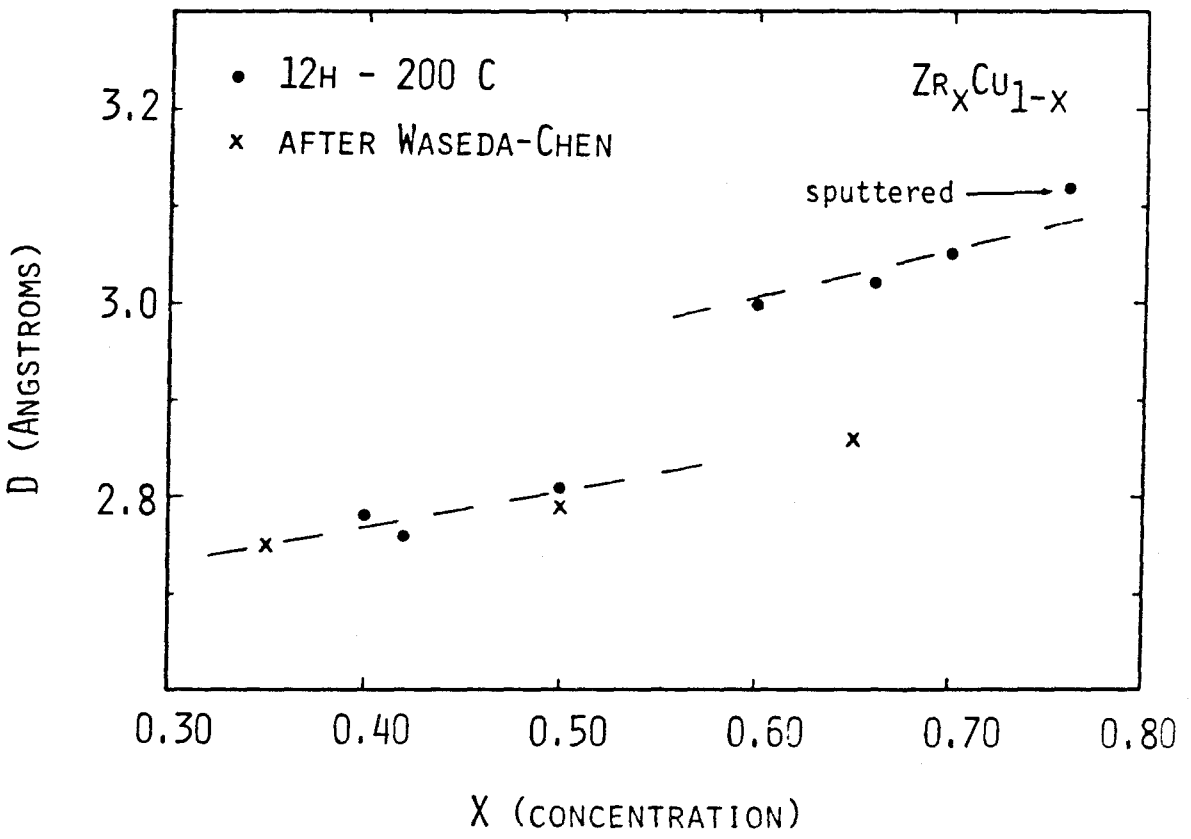

Fig. 4.1.2

Average nearest neighbor distances vs Zr concentration for $Cu_{100-x}Zr_x$ metallic glasses.

a four points computerized DC method described in[4]. Special care has been taken against oxidation of the samples during the experiment. Measurements of the scattered X-ray intensity were performed in the reflection geometry using MoK_{α} radiation on a Norelco diffractometer. The analytical procedure used to compute the pair correlation function was described elsewhere (5). Samples for electron microscopy were electropolished in a 20% nitric acid, 20% glycerin, 60% methanol solution at -30°C.

3. RESULTS AND DISCUSSION

Using the Ziman theory to describe the electrical resistivity of an amorphous alloy and the free volume model, Kelton et al.[6] relate the kinetics of the resistivity changes to the kinetics of the viscosity changes upon annealing in PdSi. The resistivity vs time, in terms of viscosity, can be written as:

$$\frac{\Delta\rho}{\rho_0} \propto 1 - \frac{c}{c + \ell n(\dot{\eta}/\eta_0\ t\ \exp(-c) + 1)} \qquad (4.1.1)$$

where c is a constant depending on the quenched-in free volume. Fig. 4.1.3a and b are typical representation of such topological relaxation for $Cu_{50}Zr_{50}$. As the temperature is increased further, chemical relaxation occurs and departure from this model can be seen in fig. 4.1.3c and d. At the annealing temperature of 300°C, the excess resistivity above the usual free volume relaxation increases initially linearly with time, then bends over. This is in agreement with Binder et al.[7] who describe the time-dependent resistivity in phase separation kinetics in simple binary systems like Al-Zn. Using a

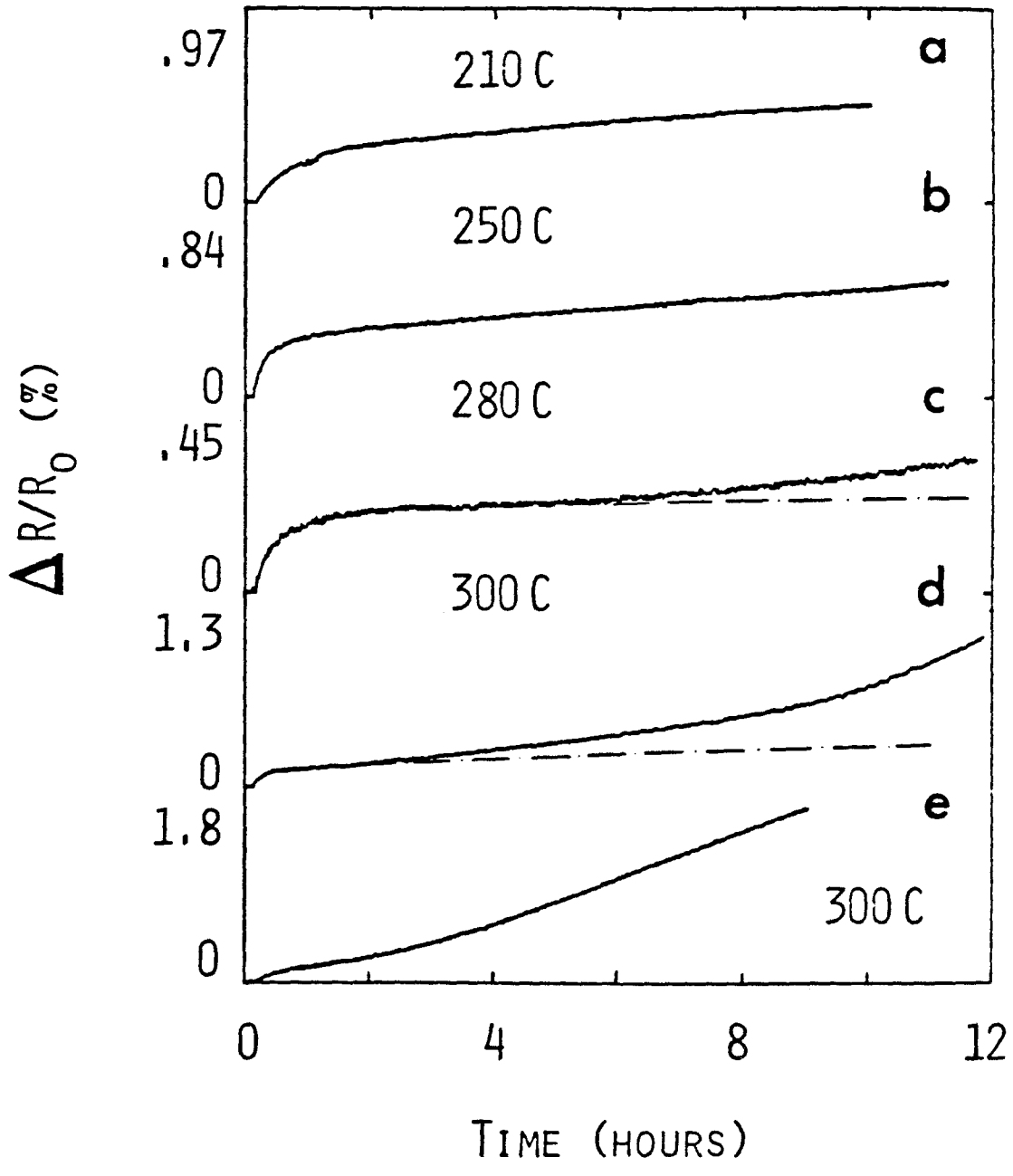

Fig. 4.1.3

Relative change with time of the electrical resistance of $Cu_{50}Zr_{50}$ in isothermal annealing $R_o = R(t=0)$.

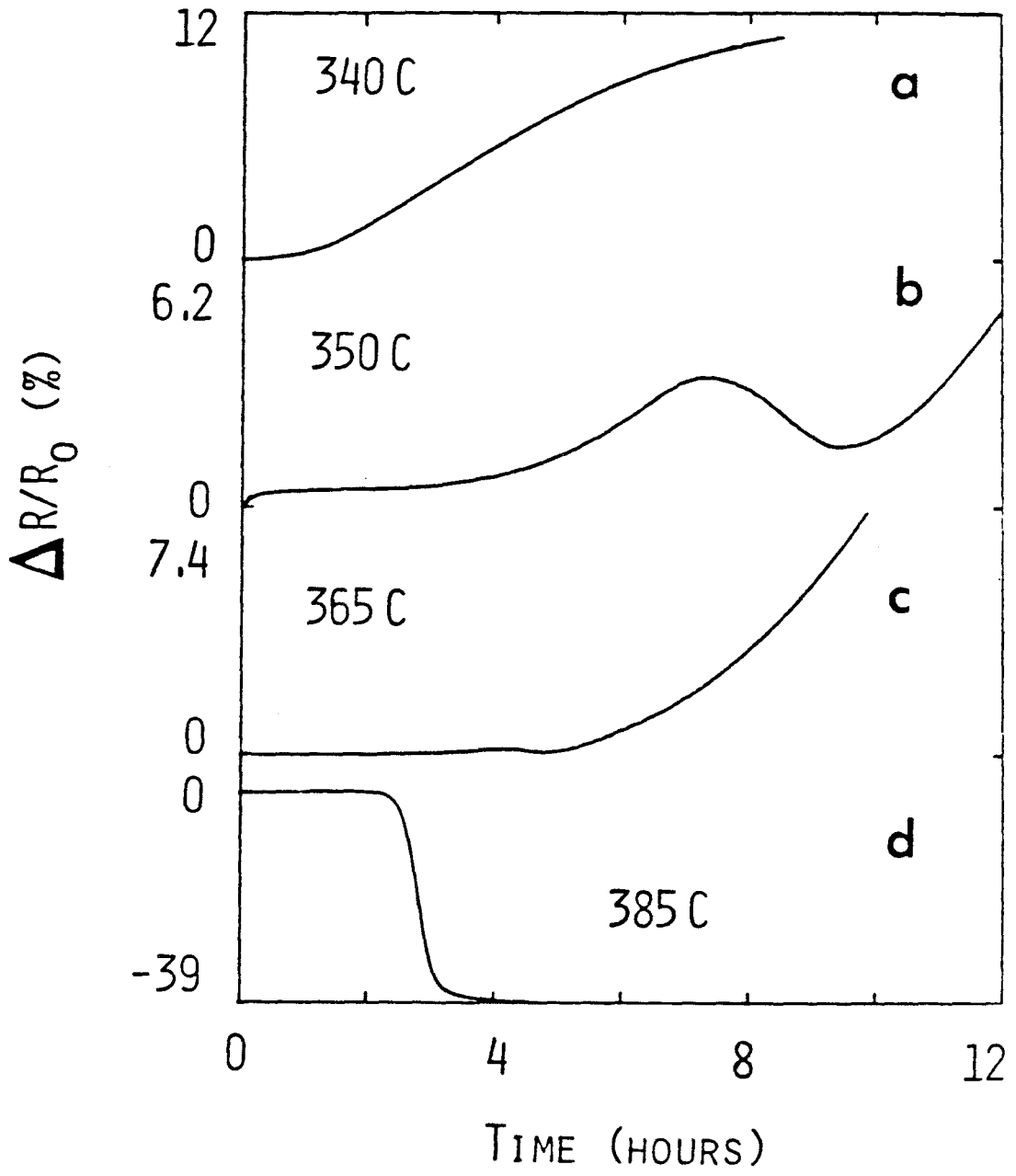

Fig. 4.1.4

Relative change with time of the electrical resistance of $Cu_{50}Zr_{50}$ in isothermal annealing $R_o = R(t=0)$.

general expression for the excess resistivity and the linear theory of spinodal decomposition they predict an excess resistivity which, at small times increases linearly in time with a slope related to the diffusion coefficient D:

$$\Delta\rho(t) - \Delta\rho(0) \propto K_c^2 \exp(Da^2K_c^4\, t/4)\, \mathrm{erf}(Da^2K_c^4\, t/4) \qquad (4.1.2)$$

a is the lattice spacing and K_c is the critical wave number. If we assume this expression valid for the Cu-Zr system, D would be the diffusion coefficient of Cu. Fig. 4.1.3e shows the relative changes in resistivity for a sample initially annealed 10h. at 210°C. The change in the slope of the excess resistivity could reflect the change in the diffusion coefficient of Cu upon free volume relaxation, which in our case, seems to increase contrary to the usual observation seen in other systems[8]. While the early stage of phase separation occurs via nucleation or spinodal decomposition for later times macroscopic grains form (Guinier Preston zones) and due to the interaction between fluctuations, the resistivity reaches a maximum and then decreases (Fig. 4.1.4b). High angle X-ray diffraction shows no trace of crystals while this process is happening (Fig. 4.1.5). Fig. 4.1.6 shows the crystallization behavior for samples initially annealed ~11h. at different temperatures. For T_a < 280°C no excess resistivity vs time is seen during annealing and all the crystallization curves fall on the same trace, characteristic of topologically relaxed structures. Crystallization is taking place in almost a single step. The small shoulder corresponds to the small subpeak seen in a DSC scan of an as-splat $Cu_{50}Zr_{50}$ alloy[3]. For T_a > 280°C we observe the onset of the excess resistivity and a well defined two step crystallization.

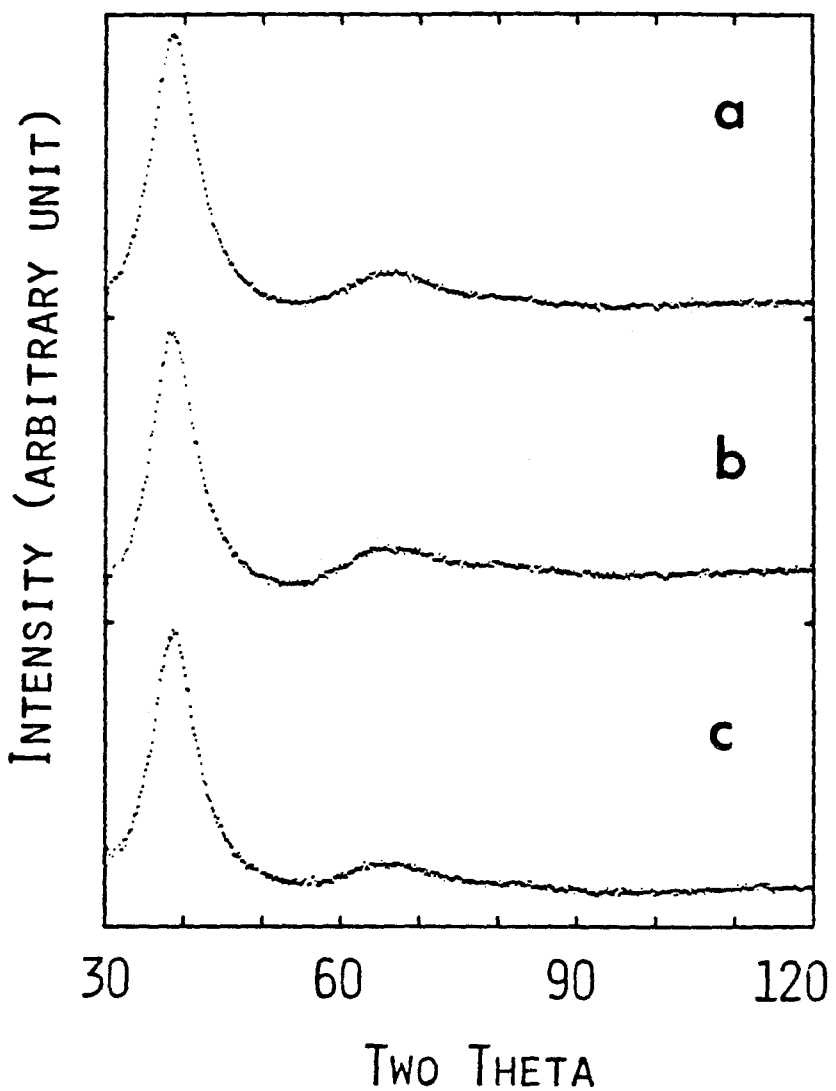

Fig. 4.1.5

High angle X-ray scans with CuK_{α} radiation for CuZr (a) as quenched (b) annealed 10h. at 300°C (c) annealed 10h. at 350°C.

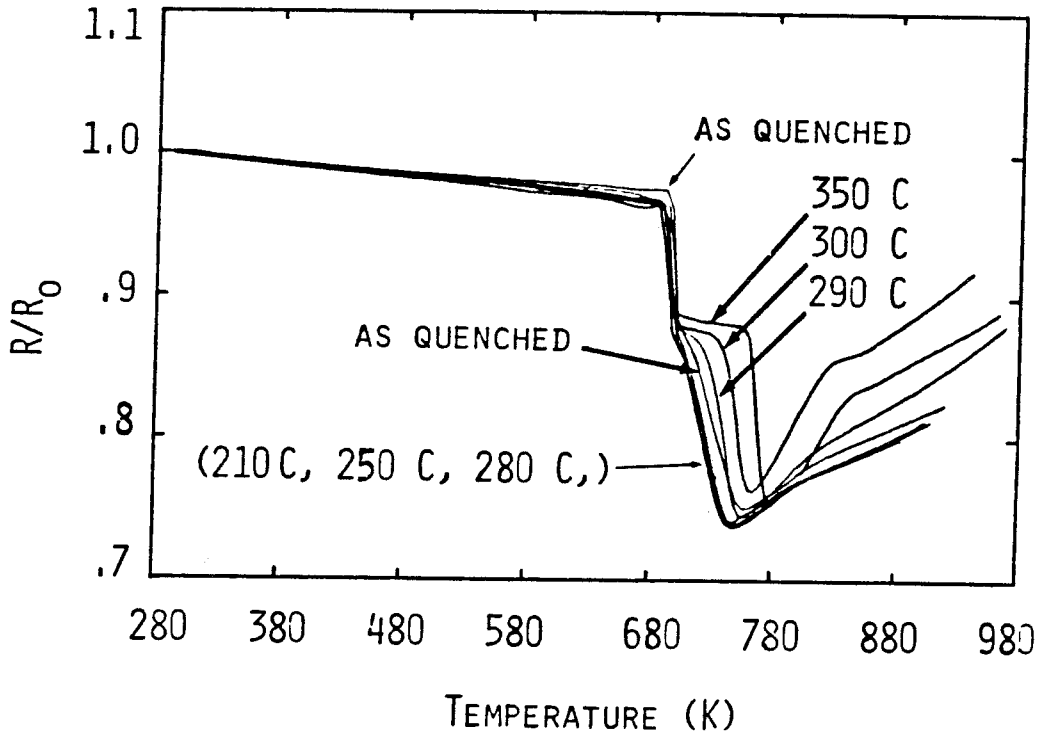

Fig. 4.1.6

Change in the electrical resistance with temperature of $Cu_{50}Zr_{50}$ for different pre-annealed conditions. R_o = R(T=300K).

After the first step X-ray diffraction shows the presence of $CuZr_2$ plus a few faint lines due to $Cu_{10}Zr_7$. The second step is associated with the crystallization of $Cu_{10}Zr_7$ in agreement with[2] (fig. 4.1.7). Note that for annealing temperature > 365°C, which corresponds to the crystallization temperature of glassy $CuZr_2$ alloys, the resistivity maximum is not seen and the amorphous phase separation is by-passed by precipitation of $CuZr_2$ crystallites. These are responsible in fig. 4.1.4c for the increase in resistivity as it was in the case of Fe-P-C[9]. At 385°C crystallization takes place in less than 3h. Fig. 4.1.8 represents the main peak of the interference function of $Cu_{50}Zr_{50}$ after different annealing treatments. The peak shifts to higher q values, gets wider (in contrast to the usual relaxation behavior described by Egami[10]), and becomes more asymmetric. Also represented are the main band of as quenched $CuZr_2$ and $Cu_{10}Zr_7$ glassy alloys. The figure suggests that the annealed $Cu_{50}Zr_{50}$ might be composed of a mixture of amorphous $CuZr_2$ and $Cu_{10}Zr_7$. Fig. 4.1.9 shows the radial distribution function of $Cu_{50}Zr_{50}$ at different annealing stages. The positions of the maxima are tabulated in Table IV.1.1. The second band consists of two subpeaks, nearly resolved, and a shoulder at high r values. We note, in the second band of the as quenched $Cu_{50}Zr_{50}$, that the first subpeak is less intense than the second one. This is typical of an unrelaxed Bernal structure and is in agreement with the results obtained by Chen[11]. Upon relaxation, the first subpeak increases in intensity and the second decreases. This is also consistent with computer model of relaxation of Bernal structures[12]. The inability to resolve the first split-peak of the second band after annealing might be partly

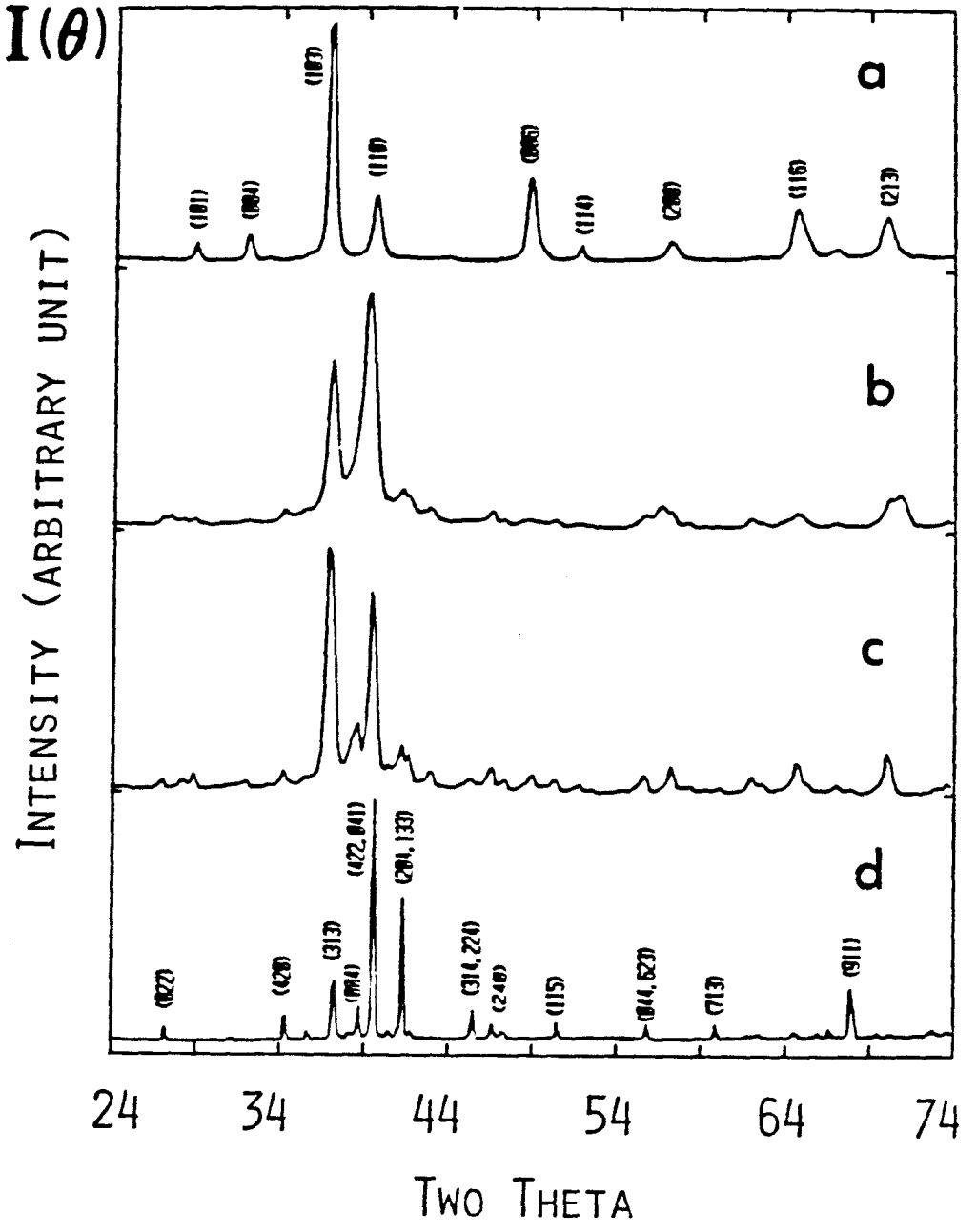

Fig. 4.1.7

X-ray diffraction pattern of (a) $CuZr_2$ crystalline powder (b) CuZr annealed 12h. at 350°C then quenched after the first resistivity drop (c) same sample quenched after the second resistivity drop (d) $Cu_{10}Zr_7$ crystalline powder.

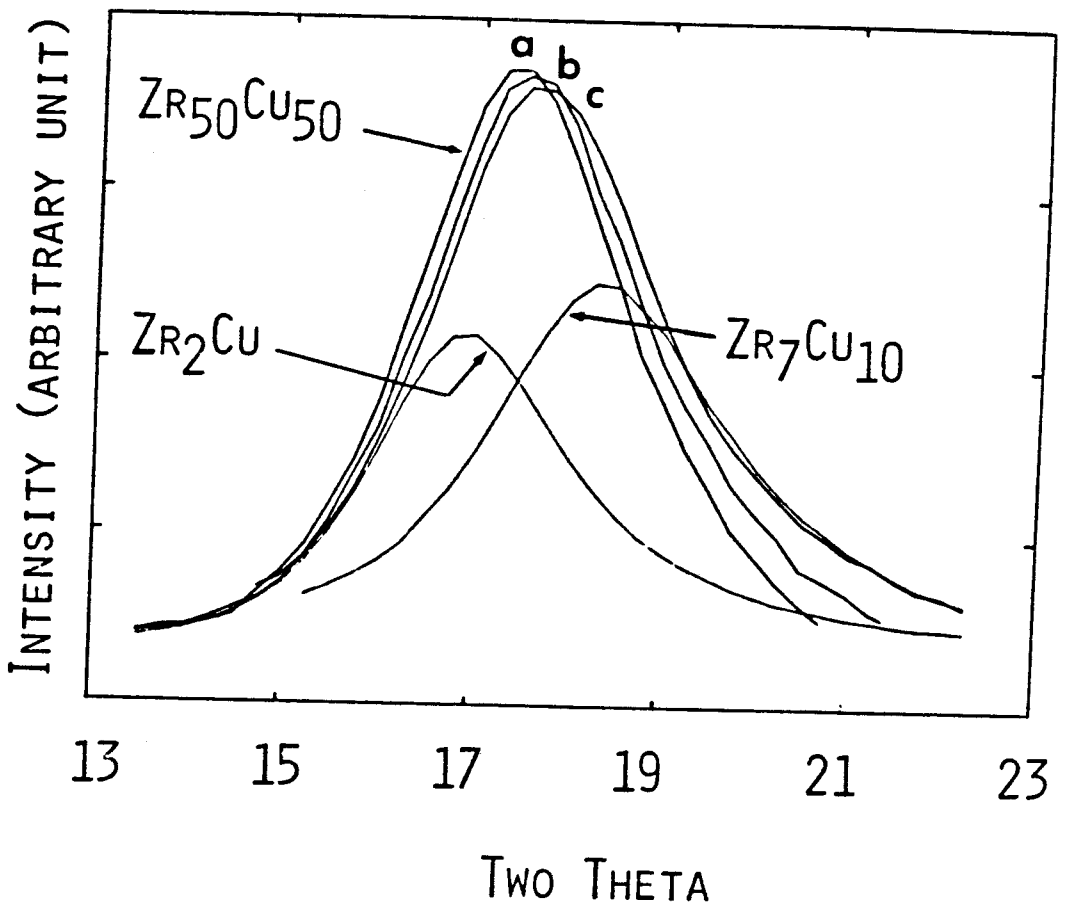

Fig. 4.1.8

X-ray diffraction scans with Mok_α ratiation for CuZr, $Cu_{10}Zr_7$ and $CuZr_2$ (a) as quenched (b) annealed at 210°C for 10h. (c) sample b annealed at 300°C for 9h.

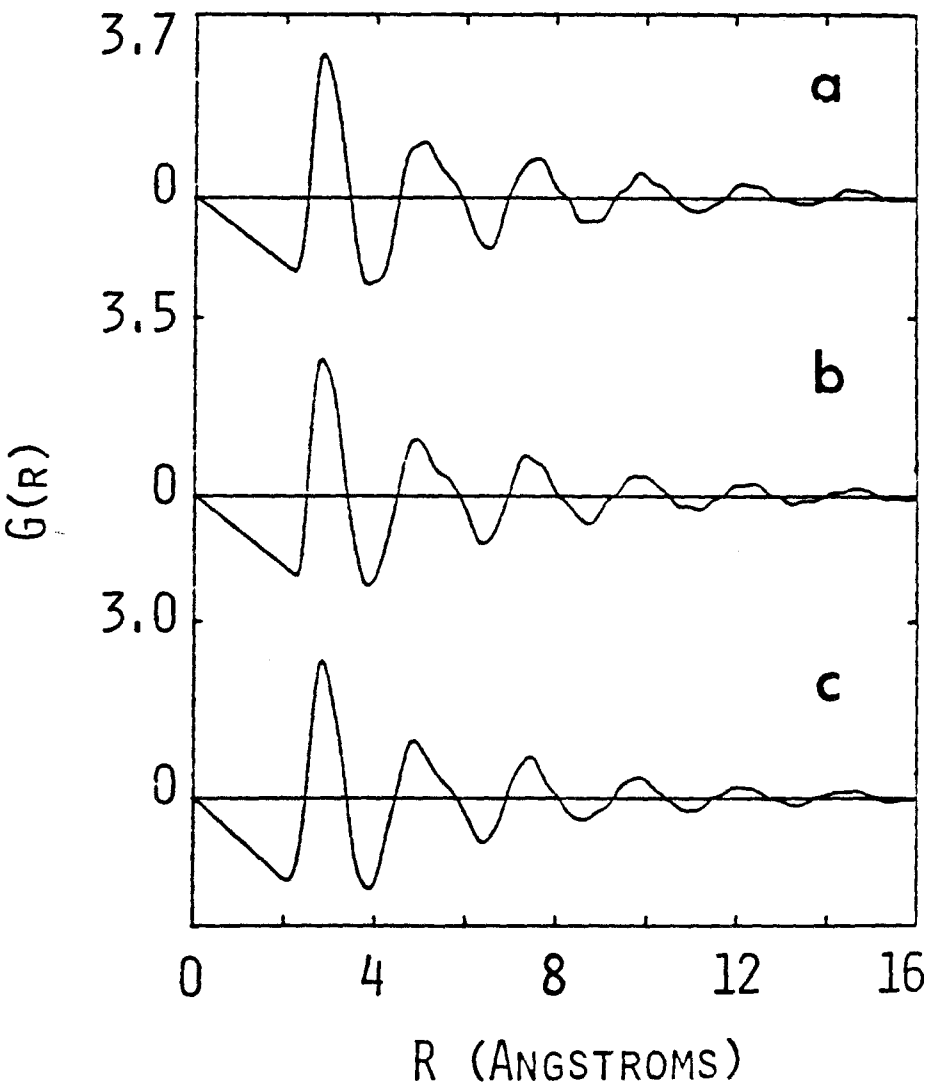

Fig. 4.1.9

Pair distribution functions for $Cu_{50}Zr_{50}$. (a) as quenched (b) annealed at 210°C for 9h. (c) sample b annealed at 300°C for 9h.

due to the relatively high convergence factor (.017) used to calculate G(r) due to the poor statistics at high angle. The second band shows a more pronounced shoulder at large r than reported in[11] for $Cu_{50}Zr_{50}$. This shoulder is due to the second band of the Zr-Zr partial pair distribution function. Fig. 4.1.10 shows G(r) of glassy $Cu_{10}Zr_7$ and $CuZr_2$. The first maximum occurs respectively at R = 2.76Å and R = 3.02Å. Fig. 4.1.11 represents $\Delta G(r) = G(r)_{annealed} - G(r)_{as\ quenched}$. The first peak is mainly due to the formation of $Cu_{10}Zr_7$, the little bump at ≃2.9Å is due to unchanged $Zr_{50}Cu_{50}$ remaining in the matrix and the shoulder at ≃3.3Å is caused by the formation of $CuZr_2$. This suggests that one fit the annealed G(r) of $Cu_{50}Zr_{50}$ to a linear combination of $Cu_{50}Zr_{50}$, $CuZr_2$ and $Cu_{10}Zr_7$. Fig. 4.1.12 shows a least square fit with 5.2% of $CuZr_2$, 26.9% of $Cu_{10}Zr_7$ and 67.8% of CuZr. The crosses correspond to experimental data points. This good fit suggeststhat the following reaction is taking place in the amorphous structure

$$\text{amorphous ZrCu} \rightarrow \text{amorphous } Cu_{10}Zr_7 + \text{amorphous } CuZr_2 \quad (4.1.3)$$

Fig. 4.1.13 shows (a) TEM of as-quenched ZrCu and (b) annealed 11h. at 210°C and 9h. at 300°C. The diffraction pattern of the annealed sample shows only a broad diffuse band (c). Those results suggest phase separation on a scale of a few 100A.

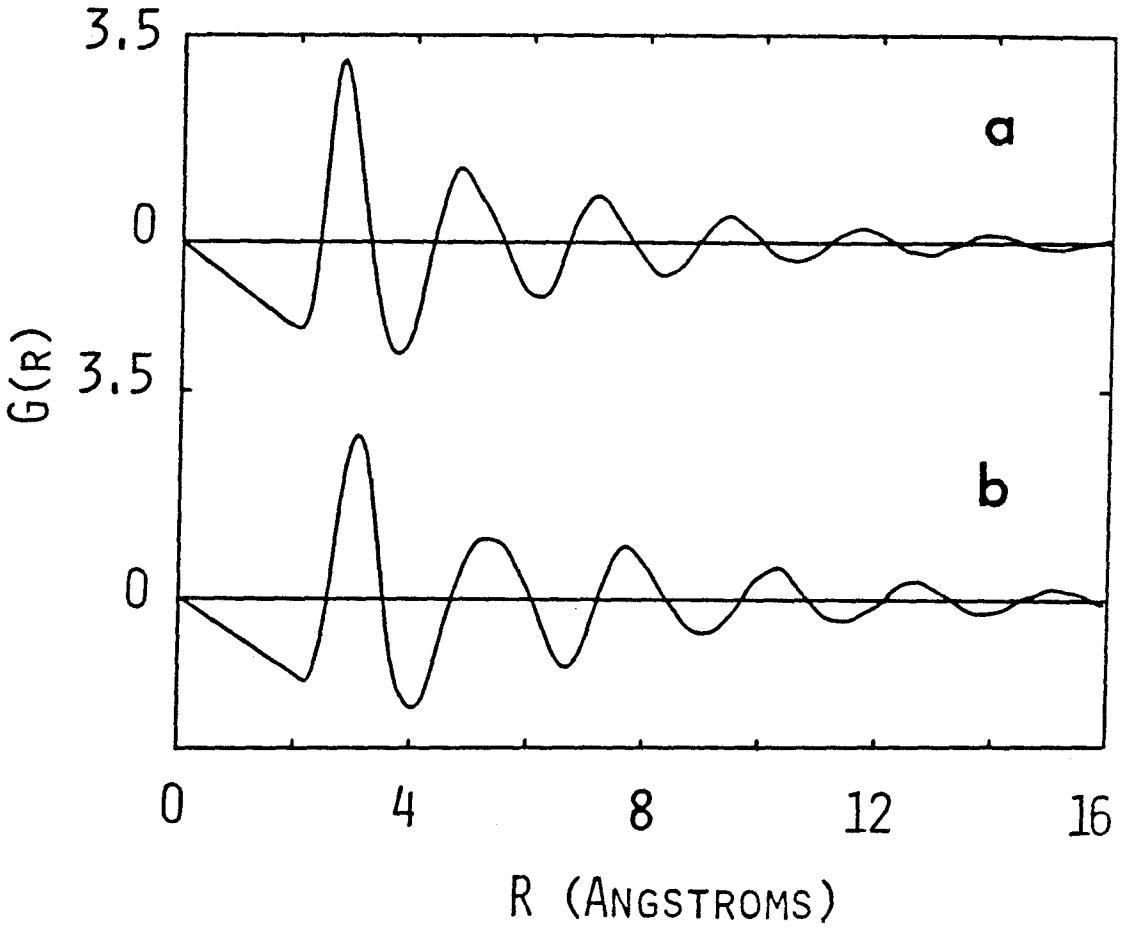

Fig. 4.1.10

Pair distribution function for (a) $Cu_{10}Zr_7$ (b) $CuZr_2$.

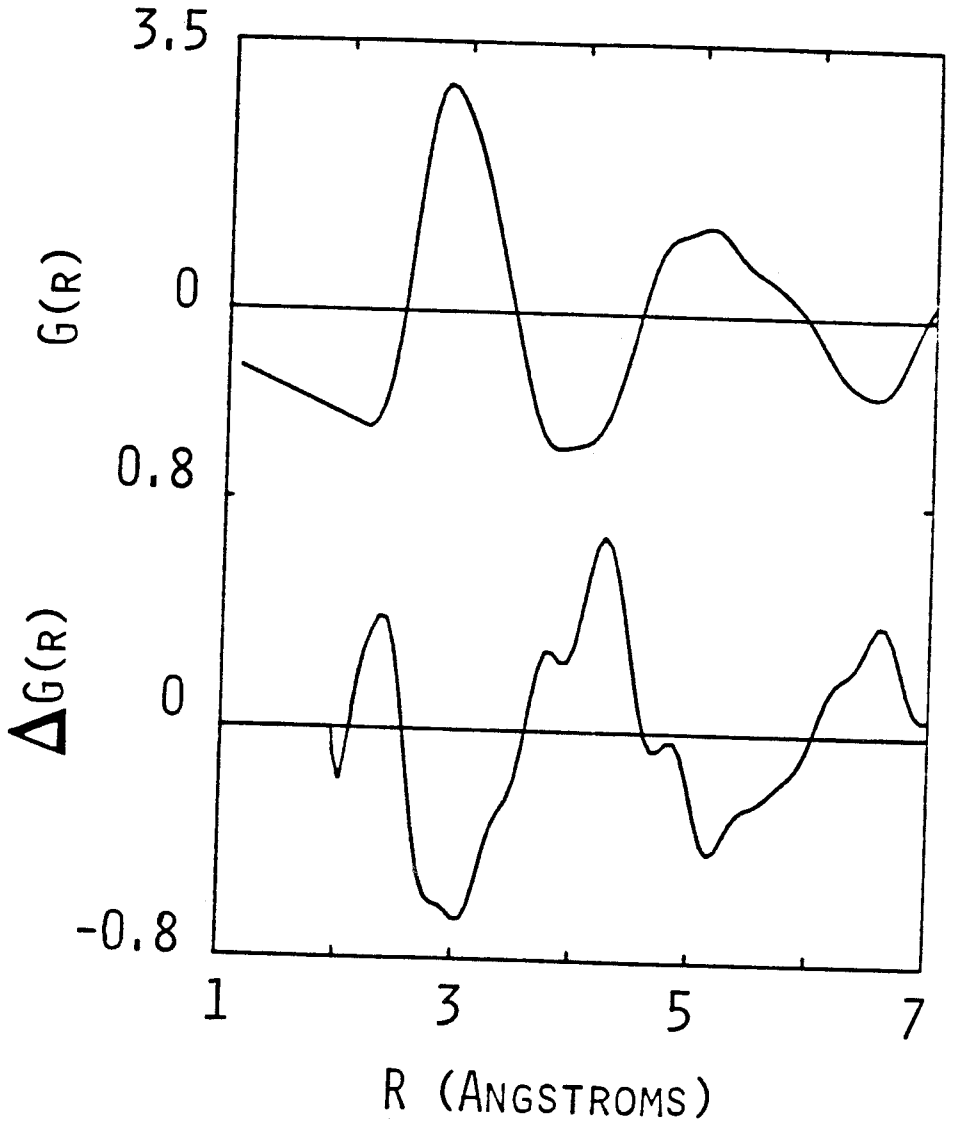

Fig. 4.1.11

Pair distribution for as quenched $Cu_{50}Zr_{50}$ and the ΔRDF between the annealed $Cu_{50}Zr_{50}$ at 300°C for 9h. and the as quenched sample.

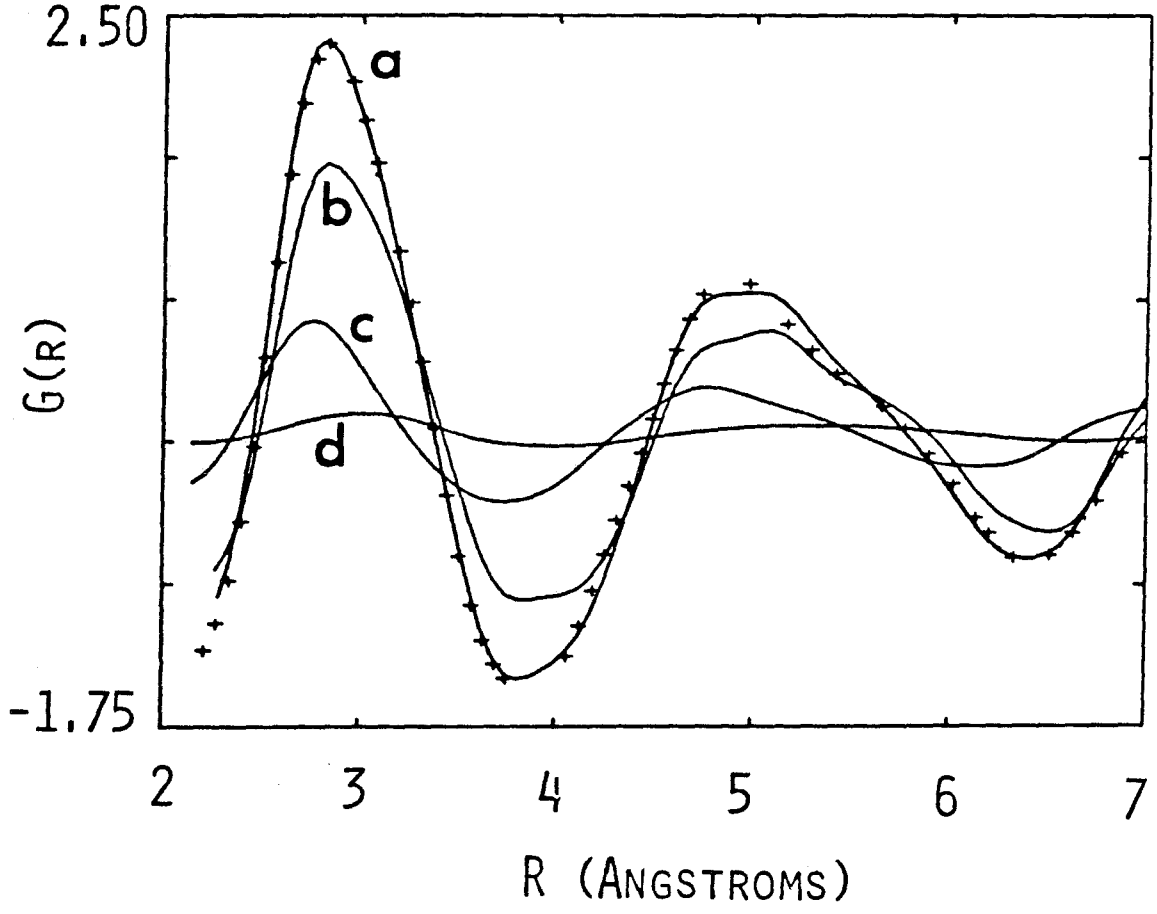

Fig. 4.1.12

The full curve (a) which represents the sum of three G(r) [(b) (67.8% $Zr_{50}Cu_{50}$), (c) (26.9% Zr_7Cu_{10}) and (d) (5.2% Zr_2Cu)] corresponds to a least square fit to the data for the annealed $Zr_{50}Cu_{50}$ (cross points).

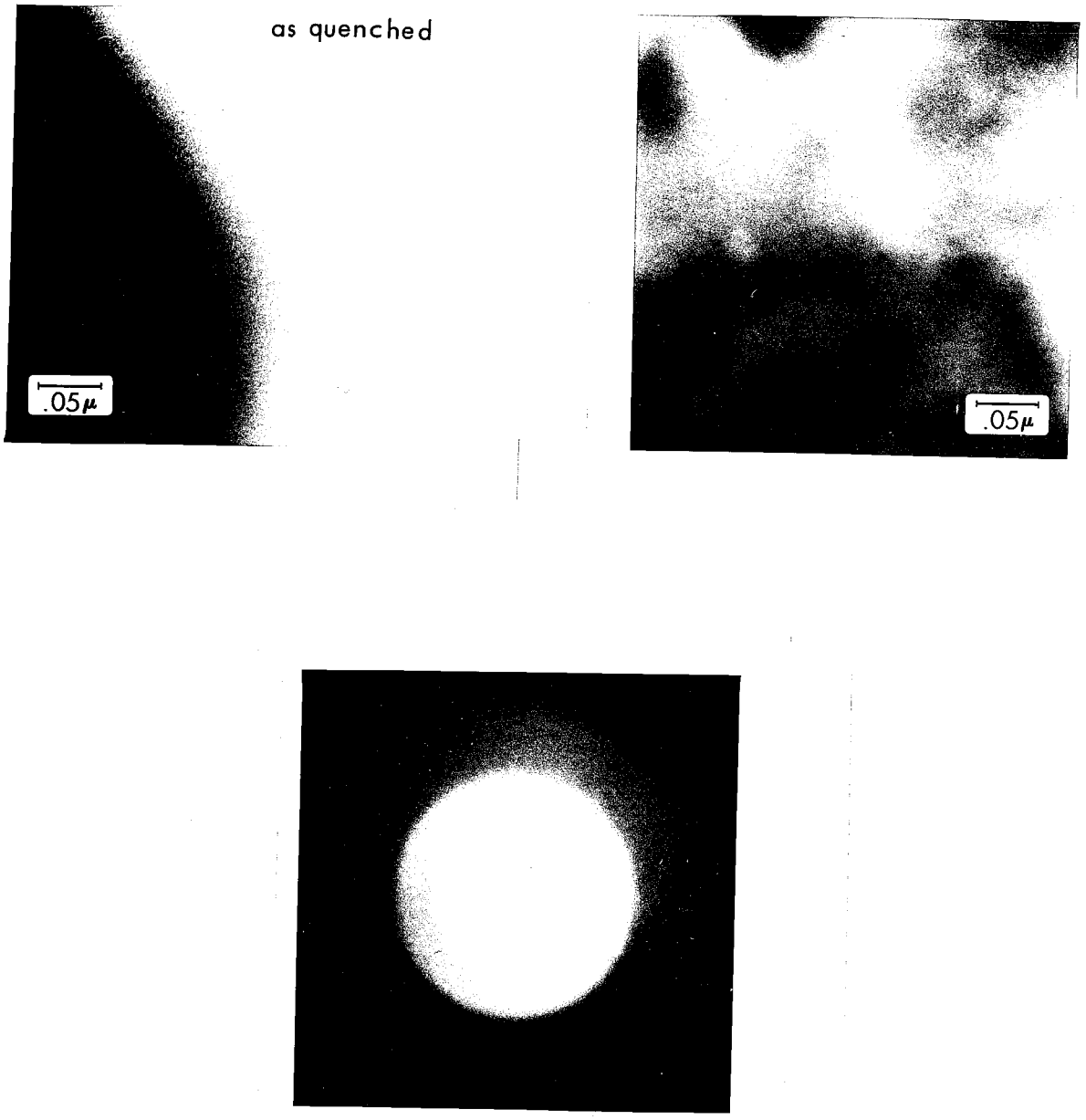

Fig. 4.1.13

(a) TEM of as quenched ZrCu (b) annealed 11h. at 210°C and 9h. at 300°C (c) diffraction pattern of the annealed sample.

Table IV.1.1

G(r) parameters for $Cu_{50}Zr_{50}$ metallic glasses (a) as-quenched (b) annealed 11h. at 210°C and (c) subsequently annealed 9h. at 300°C.

Alloy	R_1(Å)	R_2/R_1	R_2'/R_1	C.N.	Alloy	R_1(Å)	R_2/R_1	C.N.
a	2.83	1.73	1.79	13.02	Zr_2Cu	3.02	1.73	13.00
b	2.81	1.74	-	12.43		-	-	-
c	2.83	1.68	-	12.85	Zr_7Cu_{10}	2.76	1.73	12.01

ACKNOWLEDGEMENT:

The authors would like to thank Michael Atzmon for his help with the TEM results, Angela Bressan for typing this manuscript and the National Research Council of Canada for a fellowship during which this work was carried out.

*Permanent Address: I. Physikalisches Institut, Bunsen str. 9, D-3400 Gottingen, West Germany.

Work supported by the Department of Energy, Proj. Agree. No. DE-AT03-81ER10870 under Contract DE-AM03-76SF00767.

REFERENCES

1. T.W. Barbee, Jr., R.G. Walmsley, A.F. Marshall, D.L. Keith, and D.A. Stevenson, Appl. Phys. Lett. 38 (1981) 132.

2. Z. Altounian, Tu Guo-hua, and J.O. Strom-Olsen, J. Appl. Phys. 53 (1982) 4755.

3. R.L. Freed and J.B. Vander Sander, J. Non-Cryst. Solids 27 (1978) 9.

4. M. Mehra, R. Schulz, and W.L. Johnson, J. Non Cryst. Solids 61 & 62 (1984) 859-864.

5. G.S. Cargill, Sol. State Phys. 30 (1975) 227.

6. K.F. Kelton and F. Spaepen, Proc. 4th Int. Conf. on Rapidly Quenched Metals (Sendai 1981) p. 527.

7. G. K. Binder and D. Stauffer, Z. Physik B 24 (1976) 407.

8. H.S. Chen, L.C. Kimmerling, J.M. Poate, and W.L. Brown, Appl. Phys. Lett. 32 (1978) 461.

9. P.K. Rastogi and Pol Duwez, J. Non-Cryst. Solids 5 (1970) 1.

10. D. Srolovitz, T. Egami, and V. Vitek, Phys. Rev. B 24 (1981) 6936.

11. H.S. Chen and Y. Waseda, Phys. Stat. Sol. 51 (1979) 593.

12. L.v. Helmendahl, J. Phys. F 5 (1975) L141.

IV. RESULTS AND DISCUSSIONS

IV.2 $(Mo_{0.6}Ru_{0.4})_{100-x}B_x$

ELECTRICAL RESISTIVITY AND STRUCTURAL CHANGES UPON RELAXATION AND CRYSTALLIZATION OF $(Mo_{0.6}Ru_{0.4})_{100-x}B_x$ METALLIC GLASSES

ABSTRACT

Crystallization of $(Mo_{0.6}Ru_{0.4})_{100-x}B_x$ glasses takes place in three steps. The first step, corresponds to the precipitation of the sigma phase Mo_5Ru_3 which decomposes at higher temperatures. The second step is associated with the formation of an hcp solid solution of Mo in Ru, and in the last step the remaining amorphous matrix crystallize in an fcc boride.

Detailed electrical resistivity measurements taken below the crystallization temperature reveal an excess resistivity above the usual linear temperature dependence predicted by the Ziman theory. The increase in resistivity is associated with the onset of long range compositional inhomogeneity (spinodal decomposition) and the decrease with the beginning of crystallization. The electrical behavior for samples pre-annealed for 12 hours at various temperatures suggest that boron migration is partly responsible for this excess resistivity. The linear relationship between the conductivity and the density of states across the concentration range, and the fact that upon annealing $(Mo_{0.6}Ru_{0.4})_{82}B_{18}$ the maximum in the excess resistivity is associated with a minimum in the density of states, indicates that Mott's model is not applicable and suggests that the d electrons are important in the conduction. The changes in the radial distribution function during annealing at 525°C are also reported in this section.

1. INTRODUCTION

It is well known that electrical resistivity measurements form a sensitive probe for the experimental investigations of relaxation and crystallization processes in metallic glasses. Both topological (free volume annihilation) and chemical relaxation (ordering, phase separation...) influence the electrical resistivity. The problem arises in the interpretation of the data, in other words when we try to assign a specific mechanism or structural transformation to a particular feature in the electrical resistivity.

Reversible changes are usually considered as chemical ordering[1] and irreversible changes as topological relaxation[2]. The latter has been studied extensively. P. Allia et al.[3] use a theory based on the Ziman approach to the resistivity and the microscopic model for structural relaxation proposed by Srolovitz, Egami and Vitek[4] to explain the free volume dependence of the electrical resistivity. They usually attributed the increase of resistivity in their low temperature isothermal measurements to changes in compositional short range order (clustering of Mo atoms in the case of Fe-Ni-Mo-B for instance) and the decrease at high temperature to topological relaxation[5]. Their results however, are in disagreement with those of A.K. Bhatnagar et al.[6]. Kelton and Spaepen assign the increase as well as the decrease of the resistivity in Pd-Si-V to free volume relaxation and not the clustering of vanadium atoms. The reason for many of these disagreements is the lack of direct structural informations correlated with the resistivity measurements.

The effect of chemical relaxation on the electrical transport in metallic glasses, on the other hand, is poorly understood. Even when

atomic clustering[7] and phase separation[8-10] had been observed in metallic glasses, their effects on the electrical resistivity were never carefully investigated in the amorphous state until recently[11]. In the crystalline state however, the behavior of the resistivity during Guinier-Preston zone formation, spinodal decomposition etc. is well known[12-15].

Considerable work has already been done on the effect of annealing on the structure of $(Mo_{0.6}Ru_{0.4})_{100-x}B_x$ metallic glasses[16-18]. It has been suggested that upon annealing at temperature sufficiently high to permit the diffusion of boron over atomic distances, but low enough to prevent crystallization, this glass phase separates into boron-rich and boron-poor zones. Thus Mo-Ru-B represents an ideal candidate to study the effect of chemical segregation on the electrical properties of this glass. This section reports electrical resistivity and high angle X-ray diffraction measurements upon annealing $(Mo_{0.6}Ru_{0.4})_{100-x}B_x$ for x=14,18 and 22 and interprets the results in terms of phase separation caused by diffusion of boron in the amorphous matrix.

II. EXPERIMENTAL

The ingots were prepared by Rf induction melting the different constituents on a silver boat in an argon atmosphere. The ingots were remelted several times to insure homogeneity. The rapidly quenched amorphous alloys were obtained by the "piston and anvil" technique[19]. The foils were typically 40μm in thickness and 1.5 to 2 cm in diameter. They were examined by a high angle X-ray diffractometer using CuK_α radiation and only the foils showing a broad

band with no resolvable Bragg peaks were kept for further study. The detailed diffraction studies of the crystalline phases obtained from the amorphous samples by heating through the crystallization temperature were performed on the same X-ray diffractometer by scanning at 0.05°C intervals. The X-ray data used in computing the RDF were obtained in the transmission geometry on a Norelco scanning goniometer using MoK_{α} radiation and a focussing LIF monocromator. The details of the data handling and RDF calculation were described elsewhere[20,21]. The resistivity was measured using a four point dc method with Pt leads spot welded on to the samples, also described elsewhere[11].

III. RESULTS and DISCUSSION

There is now much evidence to believe that alloys with low boron content (x<18) have predominantly one type of local structure while those with high boron content (x>18) have a distinct, second type of local structure[17,22,23]. We then expect different crystallization behavior as we go through the concentration range. Fig 4.2.1 shows the normalized electrical resistivity for x=14, 18 and 22 as we heat the samples through the crystallization temperature at a heating rate of about 15°C/min. For the low boron concentration alloys we find a three step process, the first two becoming almost a single step for x=22. A shoulder is nevertheless distinguishable. Table IV.2.1 gives the crystallization temperatures and the relative percentage drop of the first two steps.

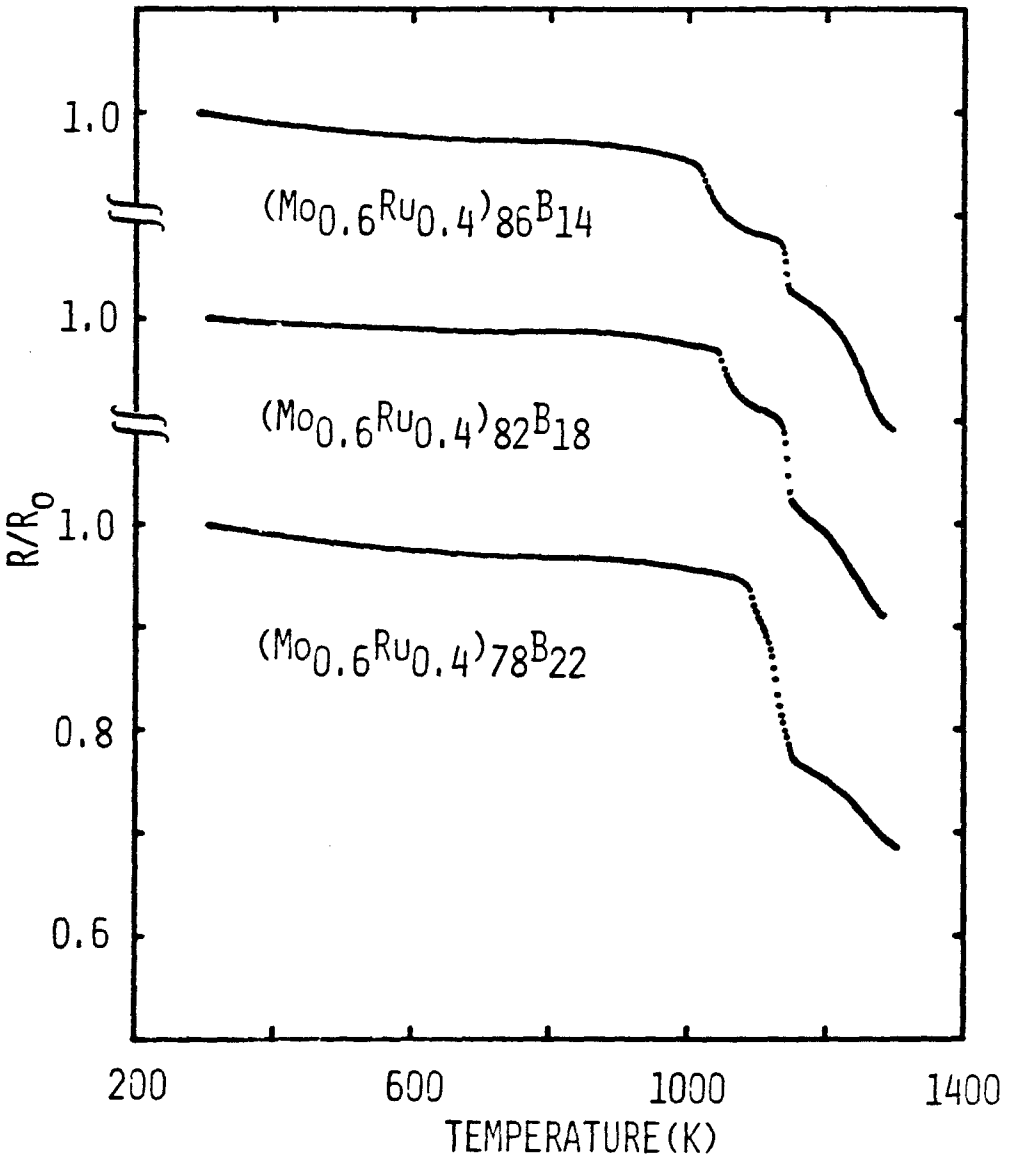

Fig. 4.2.1

Resistance traces obtained at a heating rate of 15°C/min. for x=14, 18 and 22. (R_o = room temperature resistance).

Table IV.2.1

Crystallization temperatures and the percentage drop of the resistivity during the first two steps of the crystallization.

Alloys	T1(°K)	% drop	T2(°K)	% drop
x=14	1020	60	1135	40
x=18	1045	45	1135	55
x=22	1085	27	1120	73

It is clear from the data in the table that the first transition around 1020K is characteristic of primary crystallization from glasses with low boron concentration and the second around 1130K, from glasses with a high boron content. In order to analyze the crystalline phase corresponding to each step we applied to a foil of $(Mo_{0.6}Ru_{0.4})_{86}B_{14}$ the heat treatment indicated by the arrows shown in fig. 4.2.2 and took an X-ray scan after each quench. Fig. 4.2.3 represents the results for quenches from 1075K, 1170K and 1300K. The crystalline phase identified after the first step is the boron free sigma phase Mo_5Ru_3. During the second step an hcp solid solution of Mo in Ru appears in the structure and from the peaks position we estimate the Mo concentration at about 36%. In the final step the Ru hcp phase grows, the sigma phase disappears almost completely and an fcc boride of lattice parameter a=7.81Å can be identified.

Thus in glasses of low boron concentration, there is first primary crystallization of the sigma phase, Mo_5Ru_3, which transforms at higher temperature into an hcp Ru. The remaining amorphous state crystallizes into a boride phase. In a high boron concentration glass, crystallization takes place by first a formation of an hcp solid solution of Mo in Ru and then the crystallization of an fcc boride.

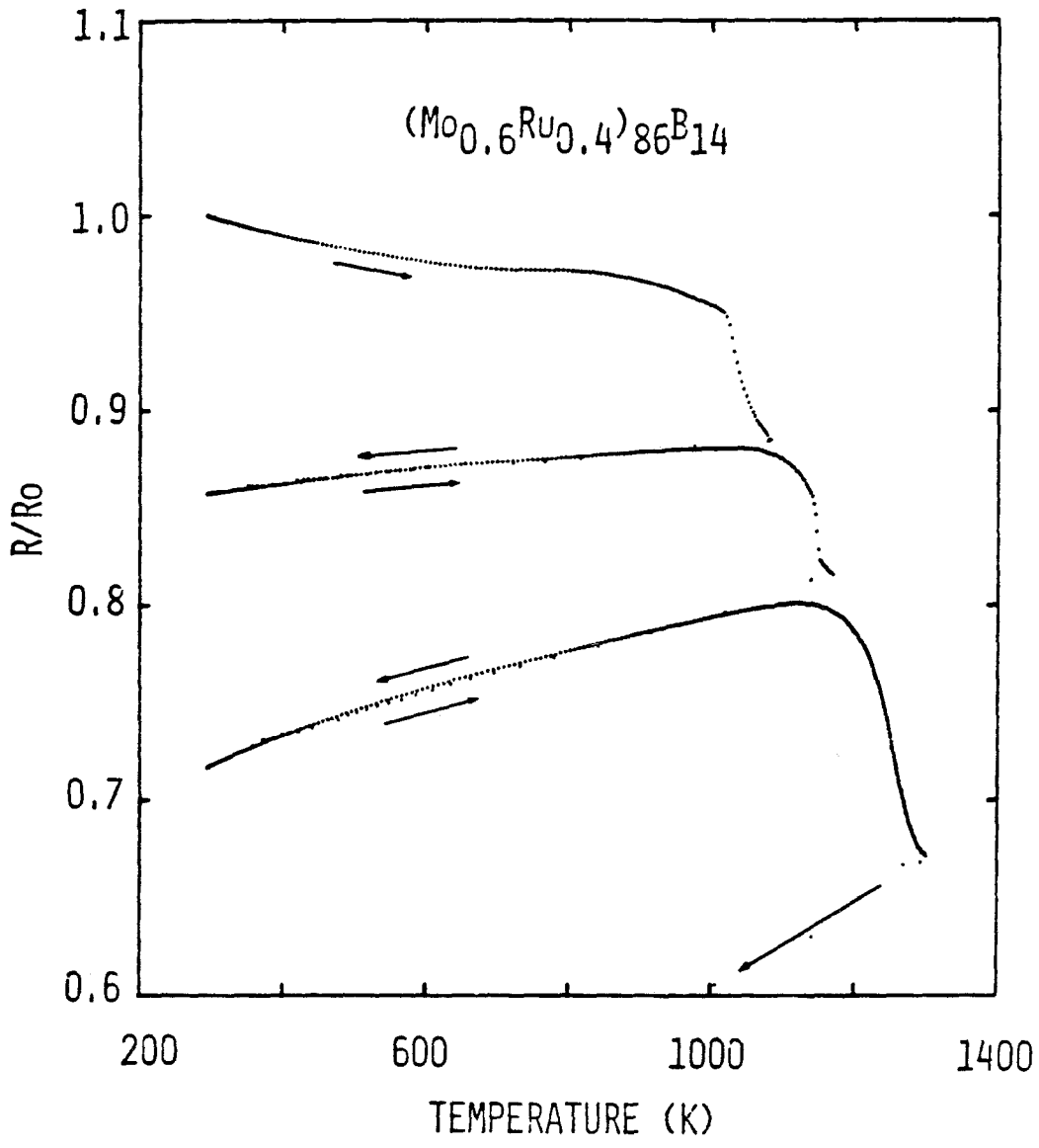

Fig. 4.2.2

The heat treatment, monitored by resistance changes, applied to $(Mo_{0.6}Ru_{0.4})_{86}B_{14}$ for the crystallization study.

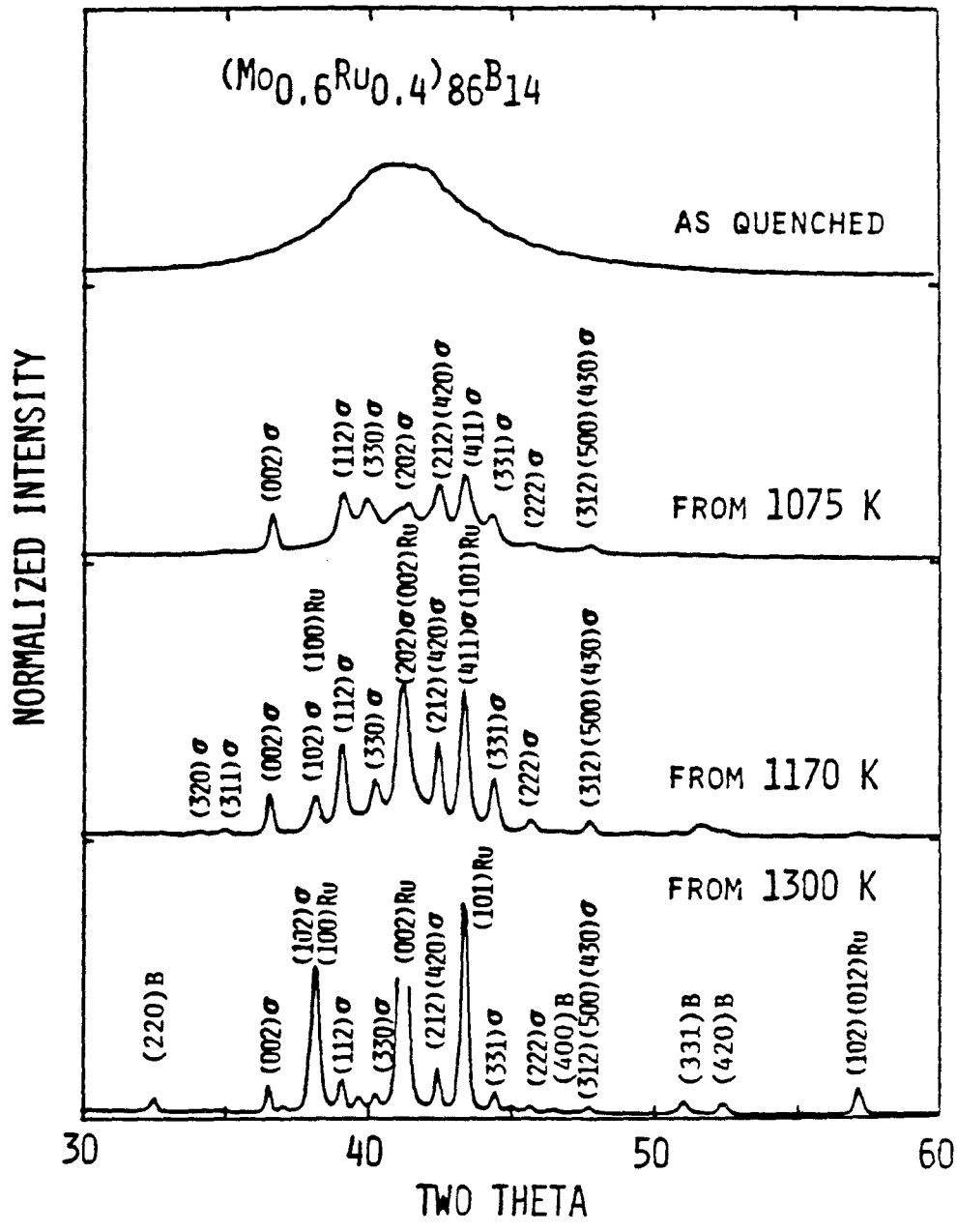

Fig. 4.2.3

X-ray scan (CuK_α radiation) of the crystalline phases obtained after each quench shown in fig. 4.2.2 .

As mentioned earlier in the case of $(Mo_{0.6}Ru_{0.4})_{78}B_{22}$ the first two transitions occur in a broad single step. However, if we anneal the sample for 12h. at 500°C we recover a well defined two step process typical of crystallization of low boron phases, fig. 4.2.4. This is what we would expect if annealing induced phase separation by diffusion of boron in the amorphous matrix occurred.

Fig. 4.2.5 shows an enlargement of the resistivity scans just before crystallization. Up to around 600K the resistivity varies almost linearly with T as it is found to in many metallic glasses at high temperatures ($T > \theta_d$) and as is predicted by the Ziman-Faber theory in the Debye approximation[24,25]. Around 800K, region "a" on the plot, a plateau or a departure from the linear temperature dependence is observed. Then the resistivity falls again first slowly in region "b" then rapidly as crystallization proceeds. C.C. Koch et al.[16] studied the small angle scattering on an $(Mo_{0.6}Ru_{0.4})_{82}B_{18}$ and found three regions of interest (fig. 10 in ref. 16). For low temperature annealing (<450°C) little difference is observed in the scattering intensity from that of the as-cast condition. For higher annealing temperatures or longer times (region II) peaks in the I(K) curves, which can be assumed to represent a "pseudo-Bragg peak" attributed to a periodicity in the scattering entity are observed. For the duration of a resistivity scan, typically two hours, this region corresponds to the plateau "a" in fig. 4.2.5. After still higher annealing temperatures or longer times (region III in ref. 16) the peaks in I(K) disappear and the curves can be fitted to the Guinier and Porod law of discrete scatterers. Some crystalline precipitates can be observed by TEM in this region of the temperature-time diagram

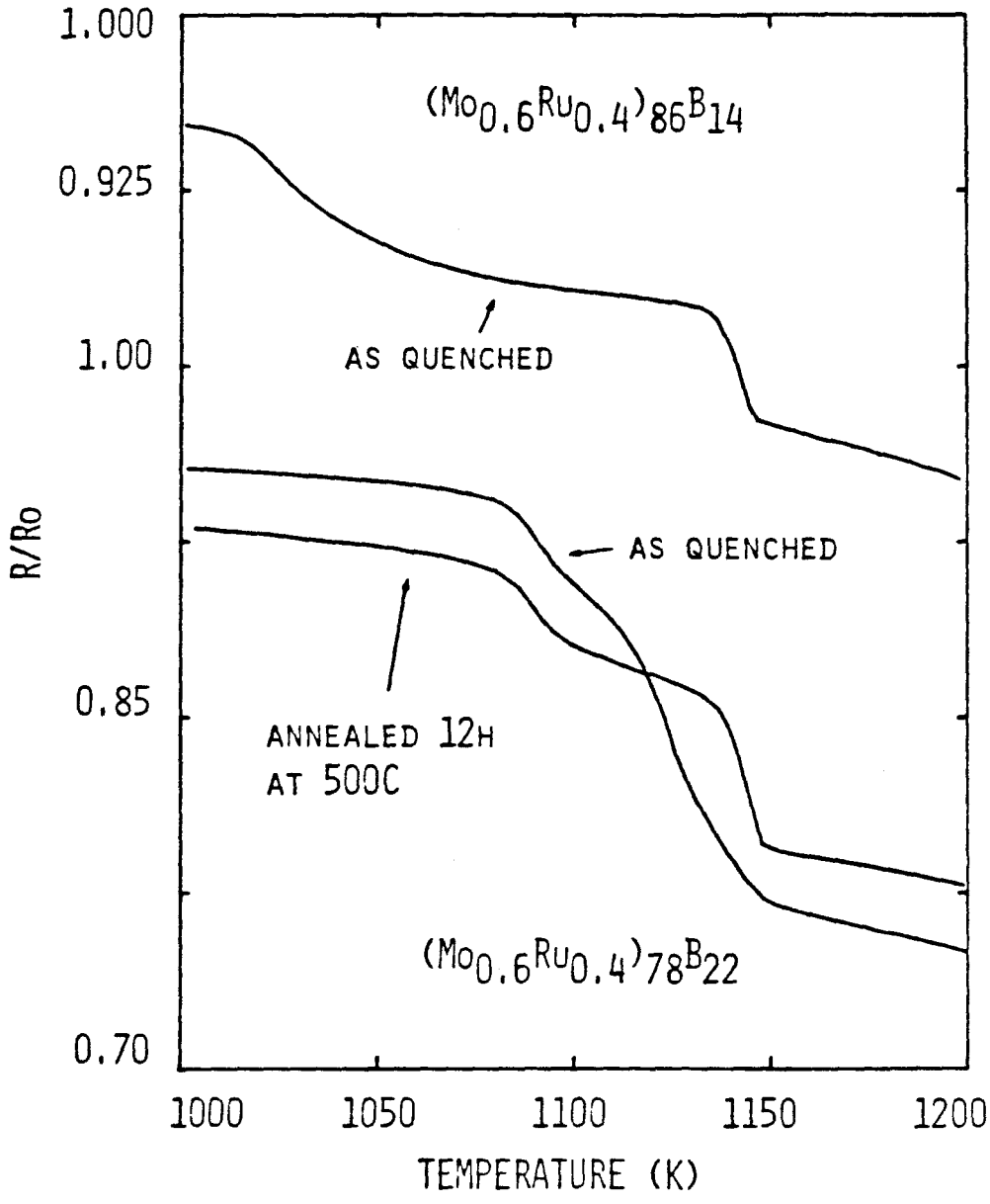

Fig. 4.2.4

Enlargement of the resistance traces around the crystallization temperature.

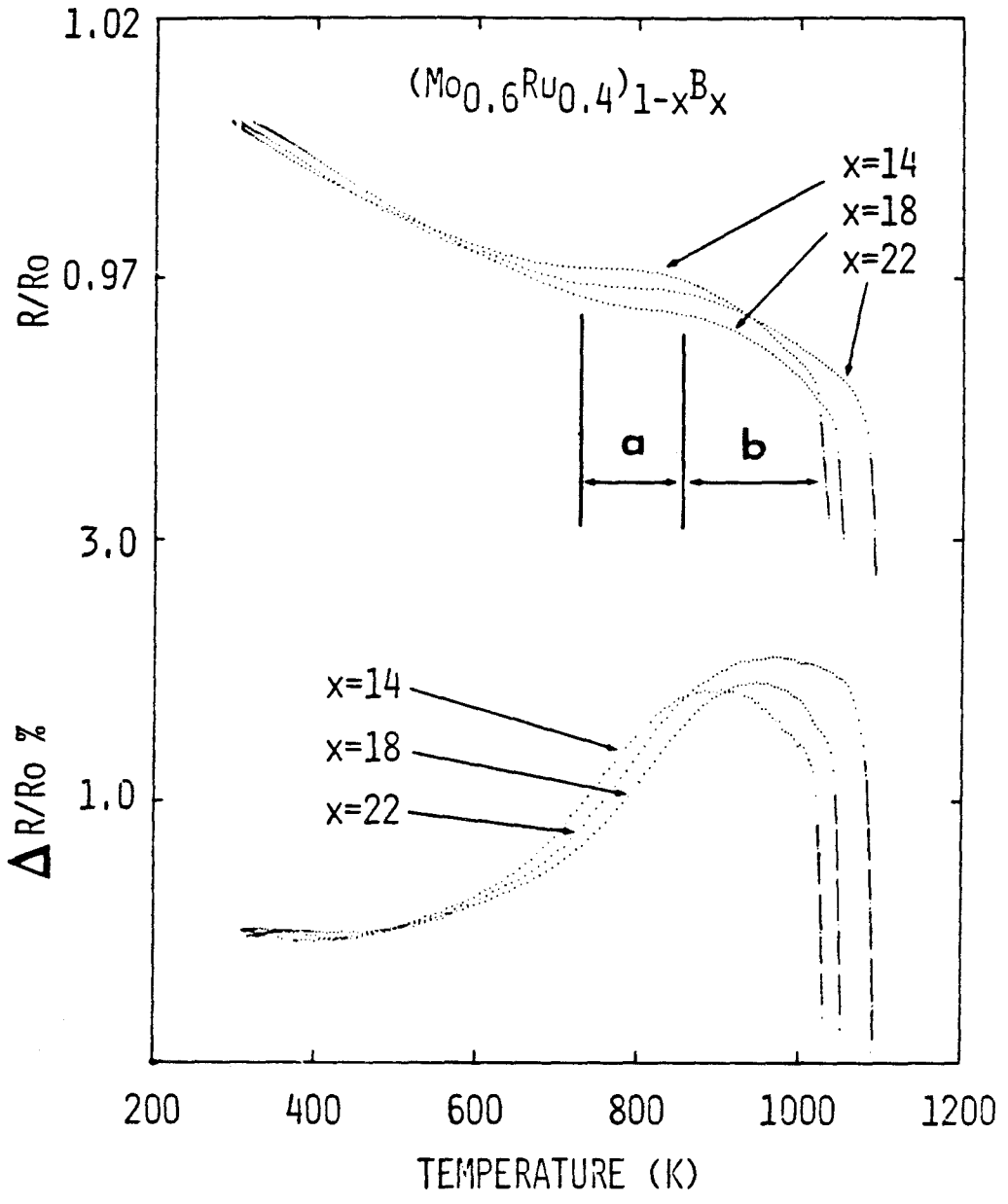

Fig. 4.2.5

Enlargement of the resistance traces below the crystallization temperature fo x=14, 18, 22. (Region "a" and "b" correspond to the region II and III in fig. 10 of ref. 4.2.16). The lower plot represents the excess resistivity above the linear temperature dependence characteristic of the low temperature region.

which correspond to region "b" on our resistivity scan. The lower portion of fig. 4.2.5 shows the excess resistivity above the linear temperature dependence due to thermal scattering. The increase in the excess resistivity seems then related to spinodal decomposition in the amorphous matrix caused by boron diffusion and the decrease, to the onset of crystallization. Such maximum in the excess resistivity is well known in the crystalline state.

Mimault et al.[15] explain the connection between the anomalous initial increase of the electrical resistivity and the presence of a peak in the X-ray small angle scattering for an Al-Zn system when quenched into the spinodal region. Recently Schulz et al.[11] found similar behavior in the amorphous state during phase separation of a $Cu_{50}Zr_{50}$ metallic glass. For Cu-Zr the increase of resistivity due to topological relaxation and the increase due to chemical segregation are well separated in time during isothermal measurements. This is not the case for $(Mo_{0.6}Ru_{0.4})_{82}B_{18}$ as we can see in fig. 4.2.6. At low temperature (<450°C) only topological relaxation (free volume annihilation) is observed. The full lines represents the best fit of the data using the Kelton-Spaepen model for topological relaxation[26]. At higher temperature both topological and chemical relaxation contribute to increase the resistivity over about the same time interval. The decrease of the resistivity at 600°C after two hours is due to the onset of crystallization and coincides with the boundary between region II and region III in fig. 10 of ref. 16. Note that an increase of the electrical resistivity has been also reported during isochronal annealing of amorphous $(Mo_{0.6}Ru_{0.4})_{82}B_{18}$ films[18].

From fig. 4.2.5 it seems that there is no correlation between the

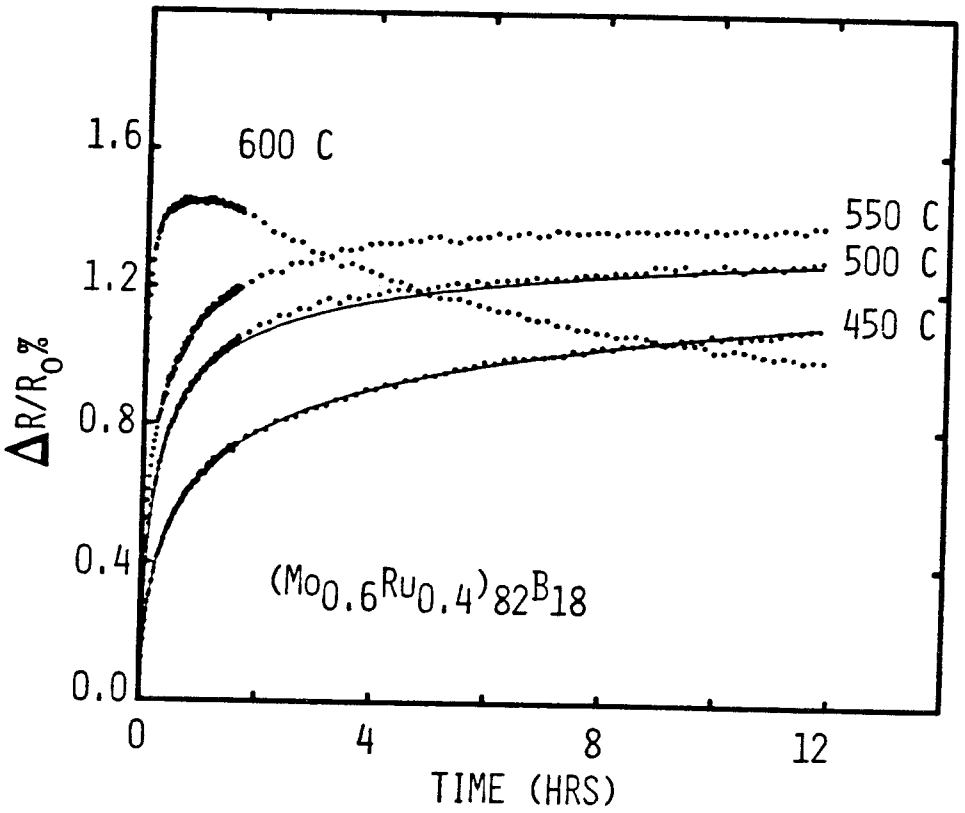

Fig. 4.2.6

Percent change in resistance as a function of annealing time at various temperatures. The solid lines are fit to the Kelton-Spaepen theory.

excess resistivity observed during a scan and the boron concentration of the glass. Fig. 4.2.7, however, shows that this anomalous behavior of the resistivity is very sensitive to the state of relaxation and that annealing has a slightly different effect on boron 14 and boron 22 glasses. If spinodal decomposition is responsible for this resistivity anomaly, topological relaxation or free volume annihilation should slow down the diffusion[27] of boron and thus affect the behavior. Johnson and Williams[23] have calculated the effective boron volume $\bar{V}_b$ across the concentration range. They found that it decreased linearly with increasing boron concentration up to a value close to the effective volume of boron in a close packed metallic arrangement (V_b^o) near the upper limit of compositions for which a glass can be made (i.e. x_m=24). If we consider $\bar{V}_b - V_b^o$ as a structural excess volume we can write an effective free volume associated with the boron atom in terms of a thermal free volume and this structural term[17].

$$V_f = \alpha(T_f - T_o)\,\Omega + \beta(x_m - x)\,\Omega \qquad (x < x_m) \qquad (4.2.1)$$

T_f is the fictive temperature associated to the quench and T_o an appropriate reference temperature at which the thermal free volume is effectively zero. Ω is the average atomic volume and α, β are constants. The diffusion of boron in the matrix depends on this free volume. In the as quenched condition the thermal term is large and masks, any effect of the structural component on the excess resistivity (fig. 4.2.5). If we anneal out the free volume at low temperature however, we can reduce the thermal term to $\alpha(T_a - T_o)\Omega$, T_a

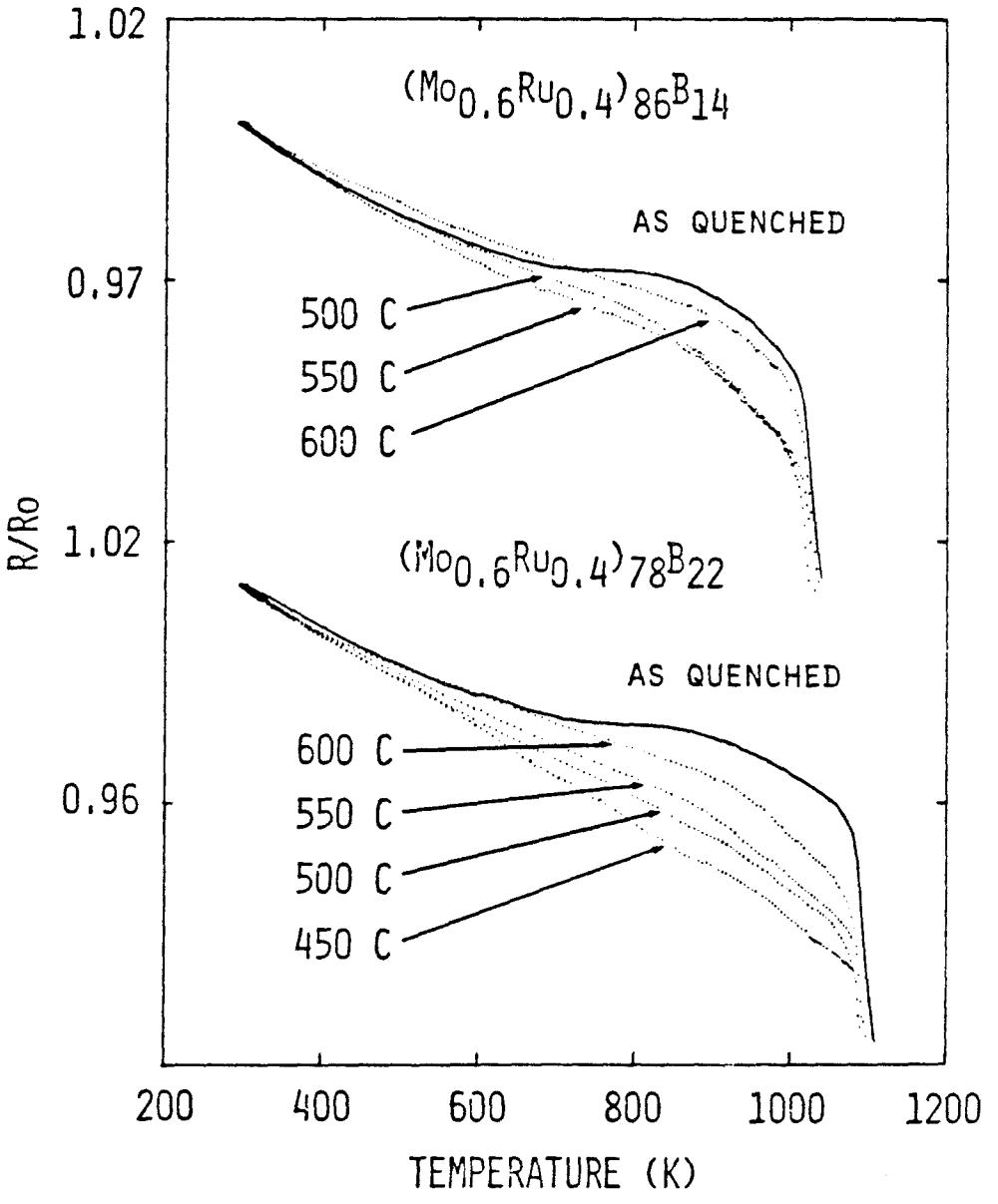

Fig. 4.2.7

Enlargement of the resistance traces below the crystallization temperature for x=14 and 22 annealed previously 12h. at various temperatures.

is the annealing temperature, and thus observe the effect of the concentration on the resistivity bump. Fig 4.2.7 shows that in the case of $(Mo_{0.6}Ru_{0.4})_{78}B_{22}$ for which the structural component vanishes ($x \approx x_m$), the resistivity anomaly completely disappears after annealing for 12h. at 450°C. The effective boron free volume vanishes preventing its diffusion, and the resistivity varies linearly all the way up to the crystallization temperature. For higher annealing temperatures, followed by a quench to room temperature, we observe the gradual effect of the increase in the quenched-in thermal free volume $\alpha(T_a-T_o)\Omega$, the resistivity anomaly becoming more significant at higher annealing temperature. For $(Mo_{0.6}Ru_{0.4})_{86}B_{14}$ the structural component is not negligible ($x \ll x_m$) and low temperature annealing is not sufficient to stop the diffusion of boron as we can see in fig. 4.2.7.

Unlike in the crystalline state, the very short electronic mean free path (3-4Å) in these glasses cast doubt on an approach using the Ziman scattering theory for resistivity and small angle X-ray scattering data from spinodal decomposition theory to theoretically explain the resistivity anomaly observed here. Fig. 4.2.8 compares the excess resistivity with the change in the density of states in terms of the reduced annealing temperature. T_{cr} is the crystallization temperature corresponding to the onset of the drastic drop in the measured property. We see that the maximum in the resistivity corresponds to a minimum in the density of states. Based on a correlation between the fractional change in magnetic susceptibility and resistivity upon crystallization, Z. Altounian et al.[28] suggest that s-d scattering which is proportional to the d density of states

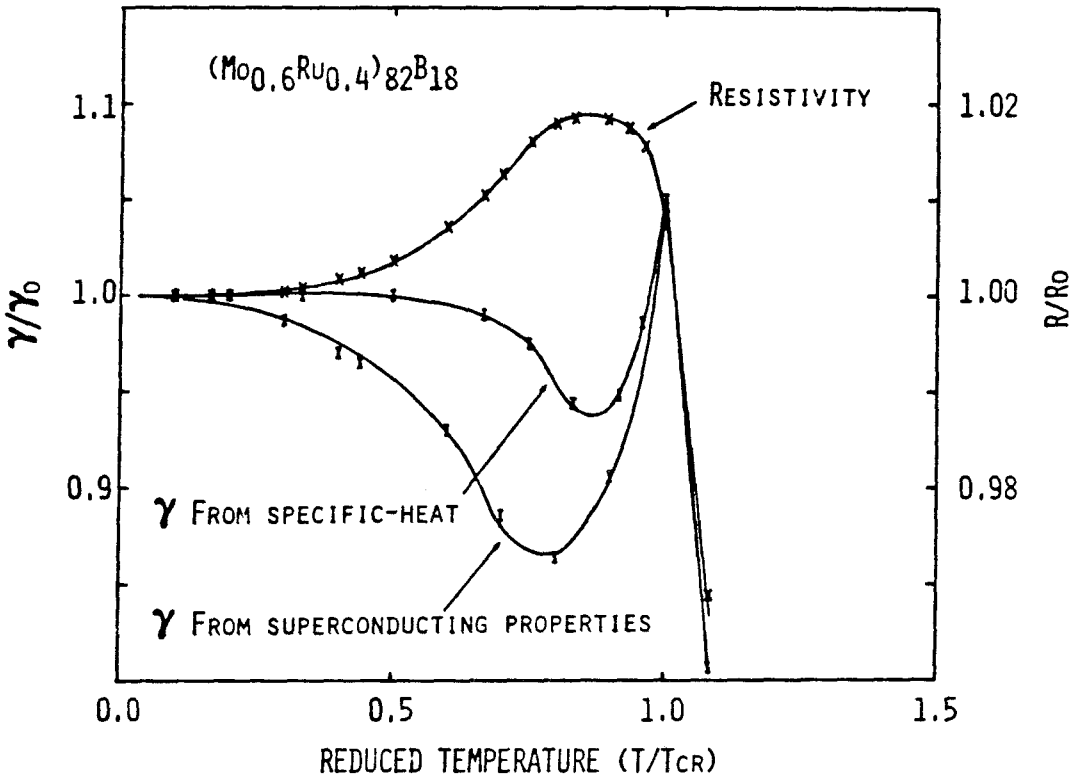

Fig. 4.2.8

Correlation between the excess resistivity and the change in the density of states (from 4.2.16) vs the reduced annealing temperature. T_{cr} is the crystallization temperature (^{o}C) corresponding to the onset of the drastic drop in the measured property.

makes an important contribution to the resistivity for Cu-Zr and Ni-Zr glasses. Our results on Mo-Ru-B show that even if resistivity and density of states are correlated during crystallization they behave in opposite directions in the amorphous state. Recently L.E. Ballentine et al.[29] have calculated the conductivities of several liquid transition metals characterized by strong scattering and s-d hybridization using the Kubo formula and clusters of 365 atoms whose pair distribution functions agree with the measured values. They treated the s and d states on an equal footing in order to evaluate the relative contributions of the s and d states to the conductivity. They found that although the diffusivity of d states is less than that of s states, the d states dominate conductivity because of their much greater density. They wrote[29]:

$$\sigma = \frac{e^2}{\Omega} [D_s N_s(E_f) + D_d N_d(E_f)] \qquad (4.2.2.)$$

Where N_s and N_d are the s and d partial densities of states and D_s, D_d the respective diffusivity. The sd contribution to the conductivity was found to be negligible For liquid La, Cr, Mn and Fe the d states contribute about 85% of the conductivity.

If this is also the case in $(Mo_{0.6}Ru_{0.4})_{100-x}B_x$ glasses we can write in a first approximation:

$$\sigma \approx \frac{e^2}{\Omega} D_d N_d(E_f) \qquad (4.2.3)$$

The average electronic diffusivity $D = 1/3 v_f \ell$ (where v_f is the average group velocity at the Fermi surface and ℓ, the average electron mean free path) is related to the critical field gradient

by[30]:

$$\left.\frac{dH_{c2}}{dT}\right|_{T_c} = \frac{4k_B c}{\pi e D} \qquad (4.2.4)$$

If the electrons involved in the superconductive pairing are also the ones responsible for the conductivity in the normal state, it follows from 4.2.3 and 4.3.4 that:

$$N_d(E_f) = \left(\frac{\pi\Omega}{4ek_B c}\left.\frac{dH_{c2}}{dT}\right|_{T_c}\right)\sigma \qquad (4.2.5)$$

It as been shown[23] that for $(Mo_{0.6}Ru_{0.4})_{100-x}B_x$ the critical field gradient does not vary with the concentration to within experimental uncertainty. A plot of the density of states vs the conductivity for different concentrations gives, therefore, a straight line as seen in Fig 4.2.9. An analog relationship is also observed for a $(Zr_2Ni)_{100-y}B_y$ metallic glasses[31]. The increasing slope at high boron concentration is associated with a general increase of $\left.\frac{dH_{c2}}{dT}\right|_{T_c}$. These results indicate that the Mott model for s-d scattering is not applicable in these glasses and suggest instead a d-band conduction. More evidence for d band conduction in metallic glasses will be presented in chapter V.

The right explanation of this resistivity anomaly must then be the following: Annealing induces phase separation into boron-rich and boron-poor zones. This spatial variation in the metalloid concentration affects the density of states at the Fermi level $N_d(E_f)$ and thus the conductivity in a d-band conduction picture.

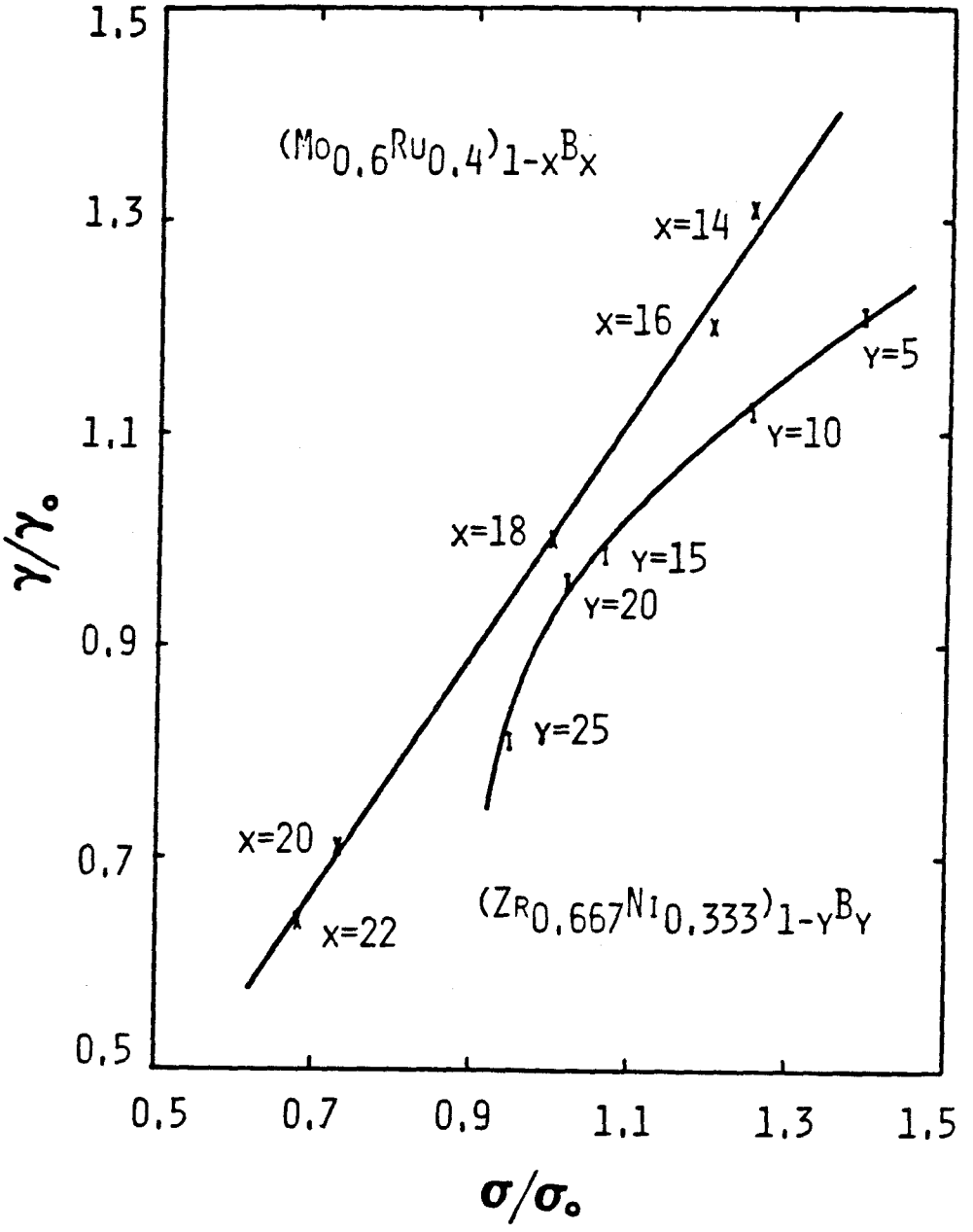

Fig. 4.2.9

Normalized specific heat coefficient vs conductivity for $(Mo_{0.6}Ru_{0.4})_{100-x}B_x$ (ref. 4.2.22 and 4.2.23) and $(Zr_2Ni)_{100-y}B_y$ glasses (ref. 4.2.31). The normalization constants correspond to x=18 and y=0 respectively.

Fig. 4.2.10 shows the changes in the radial distribution function after 2h. and 11h. annealing at 525°C and Table IV.2.2 lists the parameters obtained from the G(r).

Table IV.2.2

G(r) parameters after several heat treatments.

Alloy	Heat Treatment	R_1	R_2	R_2/R_1	C.N.
x=14	As quenched	2.79	4.62	1.66	15.3
	2h	2.78	4.64	1.67	15.7
	11h	2.79	4.59	1.65	15.1
x=22	As quenched	2.76	4.61	1.67	14.1
	2h	2.76	4.57	1.66	13.8
	11h	2.79	4.63	1.66	14.0

The first band remains almost unchanged. The first peak in the second band tends to split into two subpeaks located for x=14 around 4.30Å and 4.82Å (i.e. centered around the maximum corresponding to the as quenched condition) and for x=22, around 4.12Å and 4.57Å (i.e. centered at lower distance than the maximum corresponding to the as quenched condition). The result is then a broad first peak in the second band for x=14 and a sharp peak with a shoulder at small R value for x=22. The second peak of the second band increases slightly in intensity in both cases, mainly on the large distance side. Such behavior of the second band upon annealing is unusual for topological relaxation alone[2].

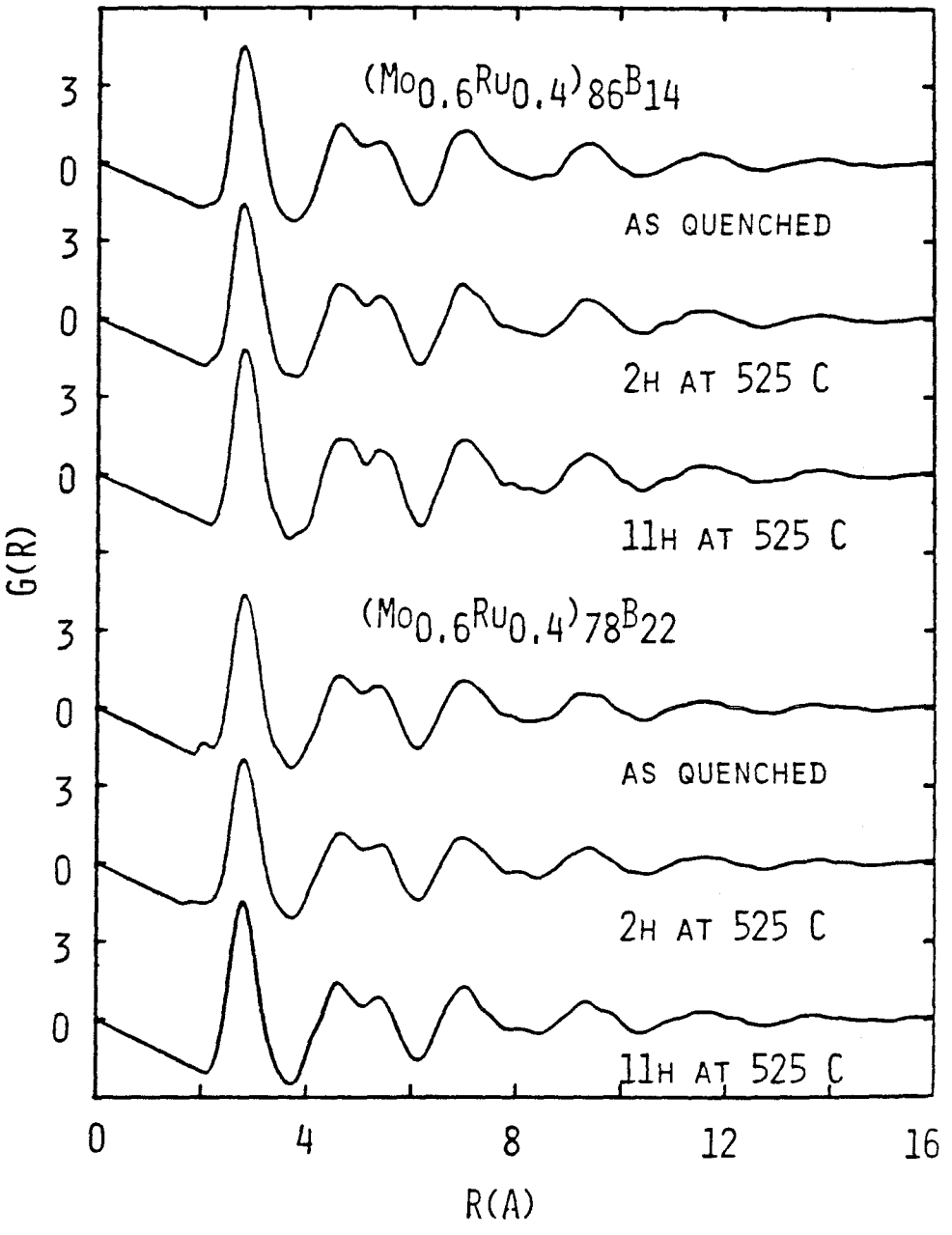

Fig. 4.2.10

Reduced radial distribution functionsfor x=14 and 22 annealed for different times at 525°C.

CONCLUSION

1. Primary crystallization of a boron free phase, hcp solid solution of Mo in Ru for high boron concentration glasses and sigma phase Mo_5Ru_3, which then decomposes at higher temperature into the hcp Ru for low boron concentration is responsible for the two first steps in the resistivity drop around the crystallization temperature. In the final step, the remaining boron-rich amorphous matrix crystallizes into an fcc boride.

2. The anomalous excess resistivity above the usual linear temperature dependence predicted by the Ziman theory at high temperature is explained in terms of phase separation caused by long range diffusion of boron which affects the density of states at the Fermi level and thus the number of carriers in a d band conduction model.

3. The changes in the radial distribution function upon annealing at 525°C cannot be explained by topological relaxation alone. Some types of chemical relaxation probably caused by phase separation must occur as well.

REFERENCES

1. M. Balanzat, Scripta Metal 14 (1980) 173 - 178 and E. Balanzat, C. Malry and J. Hillairet, J. de Phys. 41, C8 (1980) 871 - 874.

2. M. Marcus, Acta Metall. 27 (1979) 879.

3. P. Allia, R. Sato Turtelli and F. Vinal, Solid State Comm. 43, 11 (1982) 821 - 824.

4. D. Srolovitz, T. Egami and V. Vitek, Phys. Rev. 8, 24, 12 (1981) 6936 - 6944.

5. P. Allia, D. Andreone, R. Sato Turtelli and F. Vinal, J. Appl. Phys. 53 (1982) 12.

6. S. Venkataraman, K.V. Reddy, U.N. Virataswaroop, G.V. Rao and A.K. Bhatnagar, J. Non Cryst. Solids Proc. of the 5th Intl. Conf. on Liquid and Amorphous Metals (Aug. 1983)

7. H.S. Chen and S.Y. Chuang, Appl. Phys. Lett. 31 (1977) 4.

8. C.P. Chen and D. Turnbull, J. Non Cryst. Solids 17 (1975) 169.

9. J.L. Walter, D.G. Legrand and F.E. Luborsky, Mater. Sci. Eng. 29 (1977) 161.

10. J .Piller and P. Haasen, Acta Met. 30 (1982) 1.

11. R. Schulz, K. Samwer and W.L. Johnson, J. Non Cryst. Solids, 61 & 62 (1984) 997-1002.

12. P.L. Rossiter and P. Wells, Phil. Mag. 24 (1971) 425; J. Phys. C: Solid State Phys. 4 (1971).

13. A.J. Hillel, J.T. Edwards and P. Wilkes, Phil. Mag. 32 (1975) 189; Phil. Mag. 35, 5 (1977) 1221 - 1229.

14. K. Binder and D. Stauffer, Z. Physik B 24 (1976) 407 - 415.

15. J. Mimault, J. Delafond, A. Junqua, A. Naudon and J. Grille, Phil. Mag. B 38, 3 (1978) 255 - 270.

16. C.C. Kock, D.M. Kroeger, J.S. Lin and J.O. Scarbrough, Phys. Rev. B 27 (1983) 3.

17. M.Mehra, R. Schulz and W.L. Johnson, J. Non Cryst. Solids, 61 & 62 (1984) 859-864.

18. L. Soldner, H. Adrian and G. Saemann-Ischenko, Appl. Phys. Lett. (In press).

19. P. Pietrokowsky, Rev. Sci. Instrum. 34 (1963) 445.

20. A. Williams, PhD Thesis, California Inst. of Tech., Pasadena Ca. (1981)

21. G.S. Cargill III, Sol. St. Phys. 30 (1975) 227.

22. S. Hopkins and W.L. Johnson, Solid State Comm. 43, 7 (1982) 537.

23. W.L. Johnson and A.R. Williams, Phys. Rev. B 20 (1979) 1640.

24. P.J. Cote and L.V. Meisel, Phys. Rev. Lett. 39, 2 (1977) 102; Phys. Rev. B 16, 6 (1977) 2978.

25. S.R. Nagel, Phys. Rev. B 16, 4 (1977) 1694.

26. K.F. Kelton and F. Spaepen, Proc. 4th Intl. Conf.on Rapidly Quenched Metals (Sendai 1981), eds. T. Masumoto and K. Suzuki, pp. 527-530

27. H.S. Chen, L.C. Kimerling, J.M. Poate and W.L. Brown, Appl. Phys. Lett. 32(8) (1978) 15.

28. Z. Altounian, Tu Guo-hua and J.O. Strom-Olsen, J. Appl. Phys., 53(7) (1982) 4755 and Z. Altounian, Tu Guo-hua and J.O. Strom-Olsen (preprint)

29. L.E. Ballentine, S.K. Bose and J.E. Hammerberg, J. Non Cryst. Solids, 61 & 62 (1984) 1195-1200.

30. E. Helfand and N.R. Werthamer, Phys. Rev. Lett. 13 (1974) 686; Phys. Rev. 147 (1966) 288.

31. A. Mak and W.L. Johnson, Phys. Rev. Lett. 89A (1983) 353.

IV. RESULTS AND DISCUSSIONS

IV.3 $(Zr_{1-x}Hf_x)_{62}Ni_{38}$

THE EARLY STAGE OF CRYSTALLIZATION OF $(Zr_{1-x}Hf_x)_{62}Ni_{38}$ METALLIC GLASSES

ABSTRACT

This section reports a directly observable correlation between the chemical short range order and the electrical resistivity in metallic glasses . The phase transition corresponding to the first exotherm observed in a DSC scan on $(Zr_{1-x}Hf_x)_{62}Ni_{38}$ is peculiar in a sense that, contrary to usual metallic glasses, this transition is associated with an increase in electrical resistivity and X-ray diffraction taken just after the DSC peak shows only the broad diffuse band characteristic of the glassy phase. Electrical resistivity, differential scanning calorimetry, low temperature superconducting measurements, high angle X-ray diffraction, transmission electron microscopy and Mossbauer spectroscopy are used to study this transition in detail.

1. INTRODUCTION

$(Zr_{1-x}Hf_x)_{62}Ni_{38}$ represents an attractive system in the field of metallic glasses for many reasons. First of all, it can be made amorphous over a very wide range of composition[1] and contrary to the better known Cu-Zr system it is more stable and not as sensitive to oxygen contamination. Second, this glass is probably the ideal candidate for the isomorphic substitution technique[2] which consists of gradually replacing Zr by Hf in the amorphous matrix and using the different X-ray patterns to deconvolute the data into partial pair

distribution functions of the different constituent elements, Zr-Zr, Zr-Ni and Ni-Ni. This technique is based on the assumption that we can replace Zr by Hf without influencing the structure of the glass. In fact Zr and Hf are similar in many aspects, they form a continuous series of solid solution, they have similar Goldshmitt radii, electronegativity etc.. A study of the stability and the crystallization process of this system for different Zr to Hf ratio constitutes then a good test for the validity of this technique.

Buschow et al.[3] were the first to observe the peculiar behavior associated with the first DSC peak in Zr-Ni and Hf-Ni systems near 38% Ni. Similar observations were reported recently by Z. Altounian et al.[1] on the same system. The former authors suggest that the first transition in those amorphous alloys is a transition within the amorphous state and comprises mainly short range atomic rearrangement. Y.D. Dong et al.[4] on the other hand claim from X-ray diffraction analysis, that for this composition the first exotherm arises from the crystallization of $NiZr_2$ and the second, from crystallization of NiZr from the nickel enriched glass. Summarizing the results of several authors[1,4,5] on Zr_xNi_{1-x} we conclude that for $x>66$ (up to 78) a single sharp exotherm arises from the simultaneous formation of the equilibrium phases αZr and $NiZr_2$. For $60<x<66$ we observed two distinct exotherms which for $x>62$-63 can be identified as crystallization of first $NiZr_2$ then NiZr. For $x<60$ (down to 50) initial crystallization of ZrNi followed almost instantaneously by the crystallization of Zr_2Ni from the Zr enriched glass explains the asymmetric single DSC peak, with a shoulder at high temperature observed in this range. Between 60 and 62-63 the nature of the first

exotherm changes from crystallization of NiZr to crystallization of $NiZr_2$ and it is in this range that the high angle X-ray pattern remains broad after the exotherm without any resolvable Bragg peaks. It is the purpose of this section to study this peculiar transition in this range of concentration.

EXPERIMENTAL

The ingots were prepared by rf induction melting the appropriate amount of each constituents on a silver boat in an argon atmosphere. They were melted several times to ensure homogeneity. Glassy ribbons of typically 30μm in thickness, 2mm in width and several feet long were prepared by melt-spinning. They were examined by high angle X-ray diffraction using CuK_α radiation. Only the samples showing a broad band characteristic of amorphous samples were kept for further study. For each composition all measurements were done on the same ribbon to eliminate fluctuations in the free volume content. The electrical resistivity was measured using a four point dc method with pressure contact. The probe is free to move on a vertical axis inside of a quartz tube, which goes through a furnace before being fixed at the top of a dewar. The system can achieve very fast heating or cooling rates. The measurements were done in a slight over-pressure of helium. Other details are described in[6]. The DSC traces were obtained using a Perkin -Elmer DSC-1 under argon atmosphere at a heating rate of 20°C/min. Superconductivity down to around 1.6K was studied through changes in the electrical resistance. The critical field was determined by plotting the resistance of the sample as a function of the magnetic field at a constant temperature maintained using a pressure control valve over the He bath. The temperature

was calculated using the vapor pressure of the helium. Samples for X-ray diffraction were prepared by stacking three layers of ribbons together with Duco cement on a glass slide. The data were obtained in the reflection geometry on a Norelco Scanning Goniometer using MoK_{α} radiation and focussing LIF monocromator. The details for data correction and RDF calculations were described elsewhere(7). For transmission electron microscopy the specimens were thinned by jet polishing using 80% methanol and 20% perchloric acid at -15°C. Samples for Mossbauer spectroscopy were prepared by introducing 0.2% of enriched Fe^{57} in Zr-Ni as a probe element. The experiments were performed at room temperature on foils obtain by the "piston and anvil" technique. The source used was Co^{57}(Rh) and the experiments were done in the constant acceleration mode.

RESULTS AND DISCUSSION

Fig.4.3.1 shows the DSC traces and the changes in resistance as we heat the samples through the crystallization temperature at 15K/min. The DSC data were corrected for the difference in heating rate. Table IV.3.1 gives the temperatures corresponding to the onset of the two exotherms and the corresponding relative changes in electrical resistance for each transition.

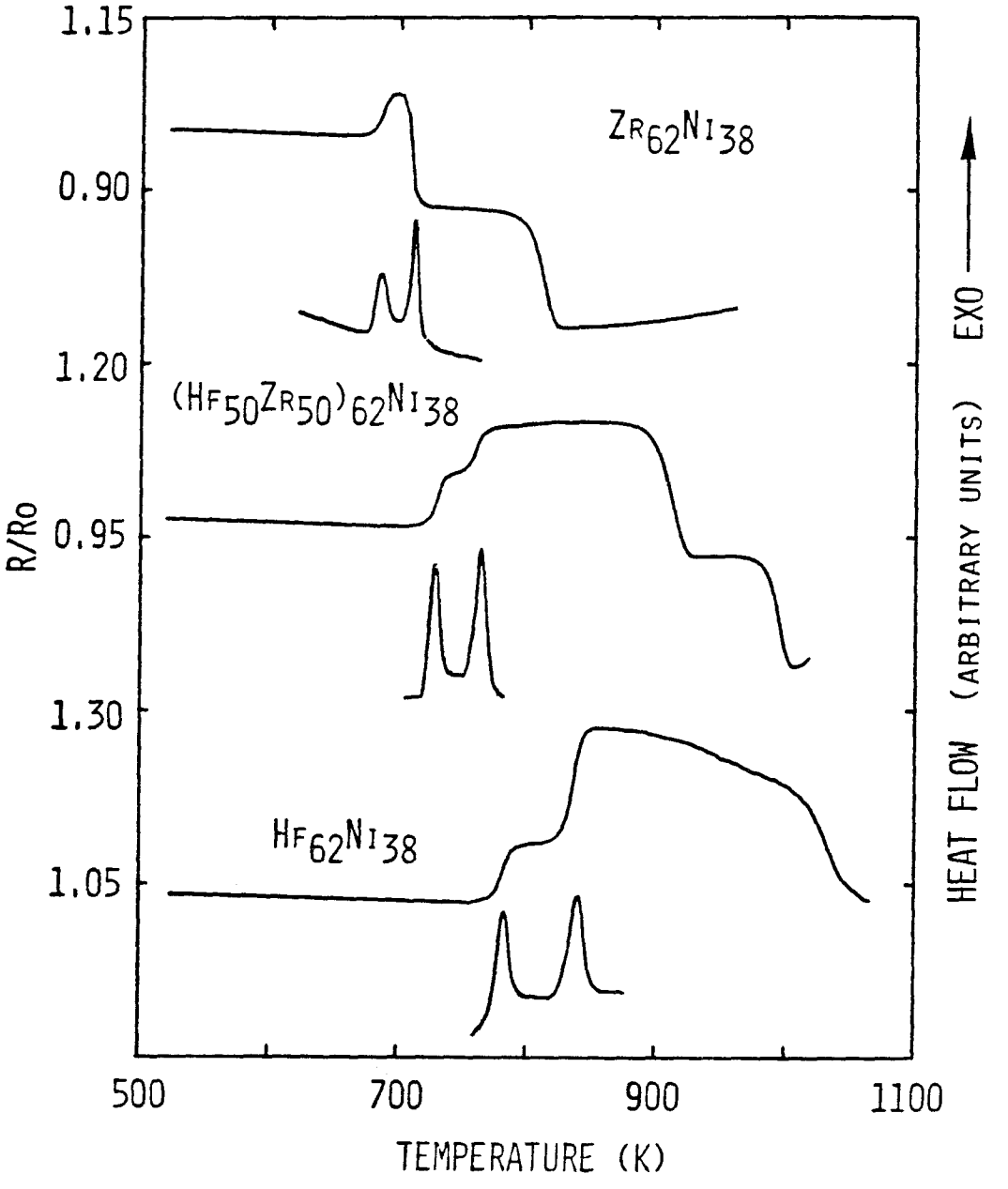

Fig. 4.3.1

Resistance and DSC traces on $Zr_{62}Ni_{38}$, $(Hf_{0.5}Zr_{0.5})_{62}Ni_{38}$ and $Hf_{62}Ni_{38}$.

TABLE IV.3.1

Temperatures of the exotherms and the relative change in electrical resistance for each transition.

ALLOYS	T1(K)	%	T2(K)	%
$Zr_{62}Ni_{38}$	675	+6.2	700	-16.7
$(Hf_{0.5}Zr_{0.5})_{62}Ni_{38}$	730	+7.8	750	+ 6.5
$Hf_{62}Ni_{38}$	775	+8.5	825	+16.8

We see in this table that Hf increases the stability of the glass by moving the peaks position to higher temperatures. Generally, the resistance decreases on crystallization since the crystalline state has much greater atomic order. In our case however, the first transition is accompanied by an increase of resistivity by roughly the same amount in all three alloys. An increase of resistivity upon crystallization has been seen also in few other systems: CuZr in the vicinity of $Cu_{10}Zr_7$[8], Zr_3Rh and Zr_3Fe[9]. Altounian et al.[8] explained this behavior from the fact that the density of states at the Fermi level increases upon crystallization which implies an increase of resistivity within the framework of the s-d scattering model. Large changes in the resistivity can be observed after the second exotherm, the resistance decreases by 17% in the case of $Zr_{62}Ni_{38}$ and increases by 17% in the case of $Hf_{62}Ni_{38}$. Bragg peaks corresponding to the equilibrium phases ZrNi and Zr_2Ni or HfNi and Hf_2Ni can now be observed from high angle X-ray scattering contrary to samples quenched just after the first exotherm. This large difference in behavior between the Zr and the Hf based alloys brings some doubts on the validity of the isomorphic substitution technique in this system.

Fig. 4.3.2a shows an enlargement of the resistivity scan below the crystallization temperature. Below 400-450 K the resistivity varies, roughly, linearly with the temperature, in agreement with the Ziman-Faber theory which predicts linear dependence of the resistivity[10,11] above the Debye temperature, due to phonon scattering. The linear dependence is represented on the figure by the dashed line for the case of $Zr_{62}Ni_{38}$. Above 400-450K a departure from the linear behavior can be observed in all three cases. Fig. 4.3.2b represents the excess resistivity above the phonon contribution. Such behavior has been seen in a number of metallic glasses[12,13,14]. J. Hillairet et al.[15] believe that the increase in resistivity reflects an evolution towards an "equilibrium state" of chemical short range order. They propose the existence of ordered domains but they do not specify the exact nature of this equilibrium state.

Based on an original idea from Mott[16], Pol Duwez et al.[17] suggest that microcrystalline precipitates are responsible for the additional increase in resistivity above the linear increase in amorphous Fe-P-C. Those precipitates would act as additional scattering centers for the conduction electrons in a manner similar to that found in the early stage of Guinier-Preston zones formation in supersaturated crystalline solid solutions. In many cases however, microcrystalline precipitates can not be found and all those interpretations then become speculation due to the lack of structural measurements coupled to the resistivity behavior.

Recently, two of us[18] showed, that the excess resistivity observed in $(Mo_{0.6}Ru_{0.4})_{100-x}B_x$ is correlated with the formation of domains of high and low boron concentration within the amorphous

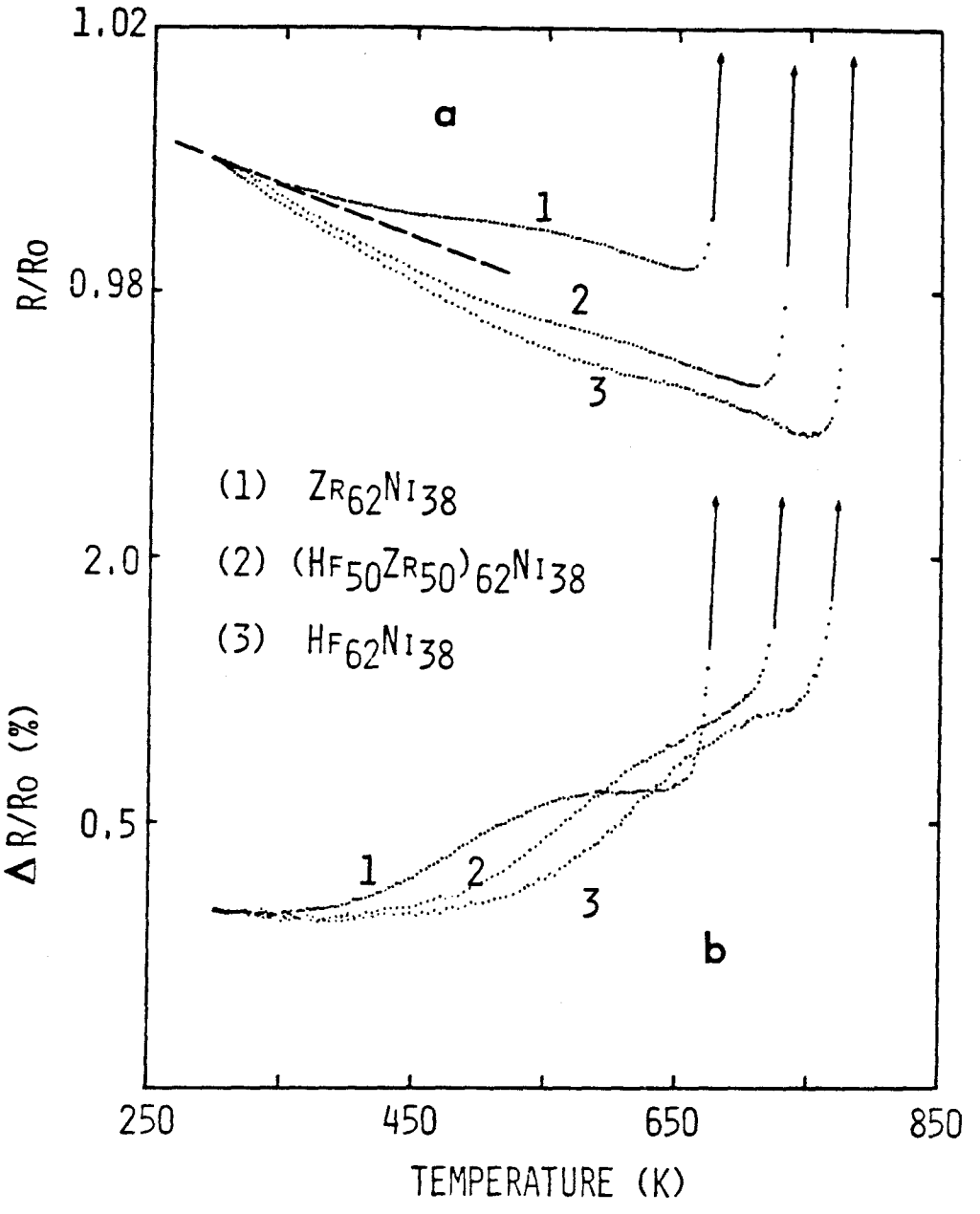

Fig. 4.3.2a & b

Enlargement of the resistance traces below the crystallization temperature. The dashed line represents the extrapolated linear dependence at low temperature.

Excess resistivity above the linear dependence obtained from a least square fit of the data at low temperature.

matrix. In $Cu_{50}Zr_{50}$ we showed that the anomalous resistivity behavior is due to phase separation into Cu rich and Cu poor zones of concentration close to $Cu_{10}Zr_7$ and $CuZr_2$ respectively[19]. From low temperature specific heat Kroeger et al.[20] observed phase separation and chemical short range ordering in Zr-Ni glasses between 60 and 66 At% Zr. They have found in a glass of 61.2 At% Zr, showing no evidence of phase separation as quenched, that annealing one hour at 200°C induced phase separation into two phases of concentration near Zr_3Ni_2 and Zr_2Ni. A heat treatment as low as 150°C for 30 min, produced great changes in the volume fraction of these two phases in a glass of 62.9 At% Zr which was already phase separated as-cast. The lowest annealing temperature at which they report phase separation (~150°C or 423K) coincides with the onset of the resistivity increase in fig. 4.3.2. We then conclude that the excess resistivity observed in $(Zr_{1-x}Hf_x)_{62}Ni_{38}$ is caused by phase separation. We also see in fig. 4.3.2b that Hf based glasses are more stable against phase separation into Hf_3Ni_2 and Hf_2Ni than Zr based glasses.

In order to study the structural transformation which takes place during the first exotherm, we heat the samples to different locations within the crystallization range at a heating rate of 15°C/min. then quench rapidly to room temperature. The full lines in fig. 4.3.3 represent the radial distribution functions for as quenched a) $Zr_{62}Ni_{38}$ b) $(Hf_{0.5}Zr_{0.5})_{62}Ni_{38}$ and c) $Hf_{62}Ni_{38}$. The results are very similar to the ones reported by Wagner and Lee[21] on $(Zr_{1-x}Hf_x)_{65}Ni_{35}$. The reduced radial distribution function exhibits a split first peak. The first maximum at r_1'=2.69Å decreases in height with increasing Hf content and corresponds to Ni-(Zr,Hf) neighbors.

The second at $r_1''=3.20\text{Å}$ becomes larger in height with increasing Hf concentration and it corresponds to Zr-Zr neighbor pairs.

The dashed lines show the reduced radial distribution function after the heat treatment represented in the onset of each figure. For $Zr_{62}Ni_{38}$ (fig. 4.3.3a) the sample has been quenched just at the onset of the second exotherm (or at the onset of the resistivity drop). The height of the first peak is reduced by about 13% which indicates a reduction in the number of unlike neighbors (Zr-Ni) and the second peak increases by about 6% reflecting an increase in the number of Zr-Zr neighbors. $(Zr_{0.5}Hf_{0.5})_{62}Ni_{38}$ (fig. 4.3.3b) has been quenched in between the two exotherms or right at the maximum of the first resistivity increase. The changes in the first band are similar to the previous case (reduction in the first peak by ~15% and increase of the second peak by ~5%) which strongly suggests that Hf behaves like Zr during the first phase transition. Finally we quenched $Hf_{62}Ni_{38}$ at the onset of the first exotherm. The two sub-peaks of the main band are now better resolved compared to the as quenched sample and the respective height of each peak remains unchanged contrary to the previous cases. The shoulder at large r of the second band is also better defined and slightly more intense. Those are typical of topological relaxation and do not reflect any change in the chemical short range order. We then conclude that the increase of resistivity during the first exotherm is due to a reduction in a number or Zr-Ni neighbors and an increase in the number or Zr-Zr neighbors. In $Zr_{65}Ni_{35}$, Wagner et al.[21] found a Warren chemical short-range order parameter of -0.04 indicating a slight preference for unlike neighbors in the first coordination shell. The following values were

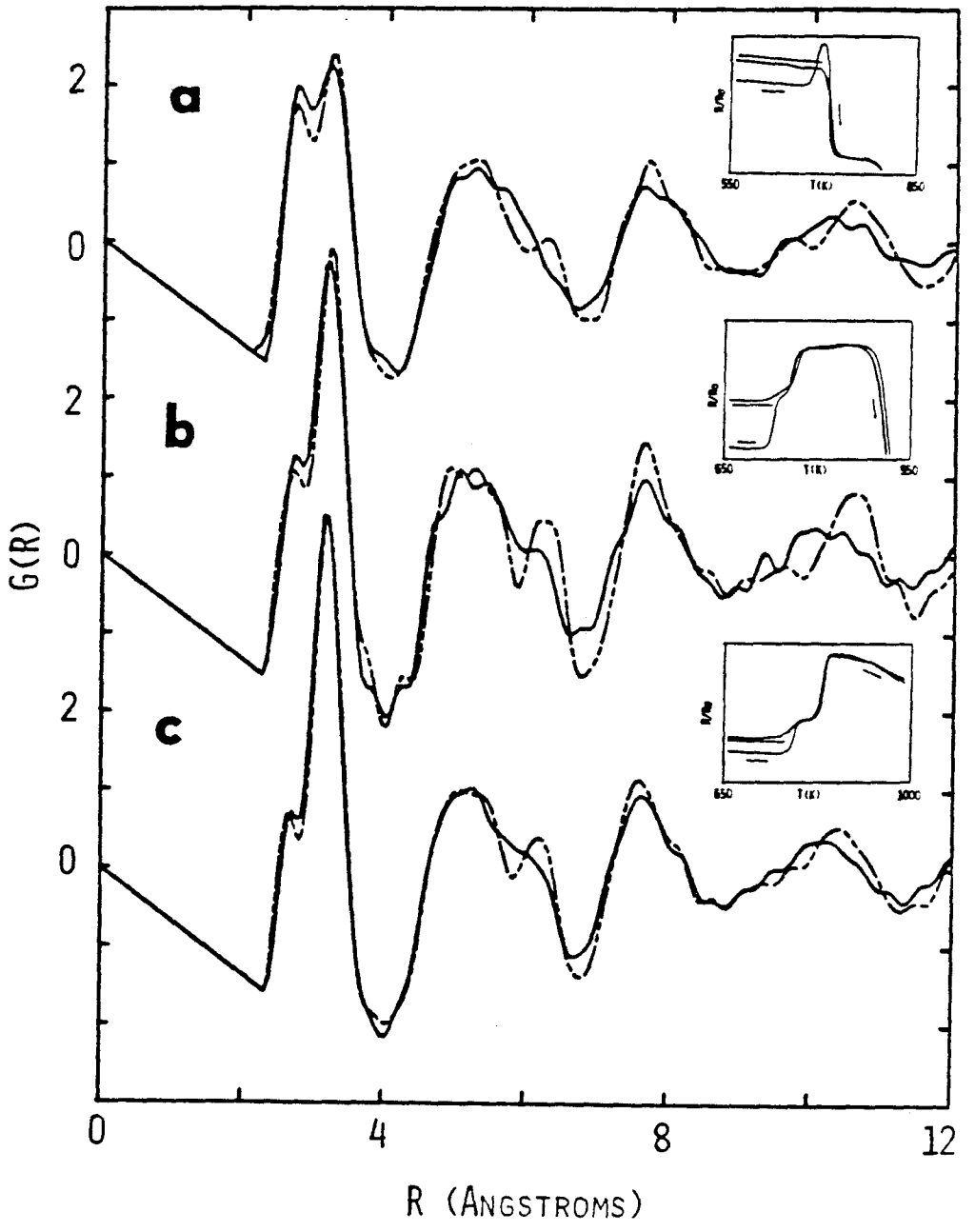

Fig. 4.3.3

Radial distribution function before (full lines) and after (dashed lines) the heat treatment represented in the onset of each figure for (a) $Zr_{62}Ni_{38}$ (b) $(Hf_{0.5}Zr_{0.5})_{62}Ni_{38}$ and (c) $Hf_{62}Ni_{38}$.

obtained for the coordination numbers: N(Ni-Ni)=3.1, N(Ni-Zr)=8.6 and N(Zr-Zr)=9.2. Roughly speaking our results suggest that the number of Zr-Ni neighbors should decrease to around 7.4 and the number of Zr-Zr increase to around 9.7.

This study could actually provide an interesting way to test the applicability of the Faber-Ziman theory in this amorphous alloy. The resistivity in its most general form can be written as[23]:

$$\rho = \beta\Big\{c_1 \langle|t_1|^2 a_{11}\rangle + c_2 \langle|t_2|^2 a_{22}\rangle + \tag{4.3.1}$$
$$c_1c_2(\langle|t_1|^2(1-a_{11})\rangle+\langle|t_2|^2(1-a_{22})\rangle+\langle(t_1t_2^*-t_1^*t_2)(a_{12}-1)\rangle)\Big\}$$

c_1 and c_2 are the concentrations of the two constituents, t_1 and t_2 are the single site scattering matrix, the a's are the various partial structure factors, β depends on the average atomic volume, the electron density and the Fermi velocity and the average $\langle f(K)\rangle$ means[29]:

$$\langle f(K)\rangle = \int_0^{2k_f} f(K)K^3dK \tag{4.3.2}$$

Using the isomorphic substitution technique to measure the partial structure factor before and after the first exotherm and the t-matrices for Ni[24] and Zr[25] we can write in the limit of a constant prefactor:

$$\frac{\Delta\rho}{\rho_o} = \frac{\beta}{\rho_o}\left\{c_1^2\langle|t_1|^2\Delta a_{11}\rangle + c_2^2\langle|t_2|^2\Delta a_{22}\rangle + c_1c_2\langle(t_1t_2^*-t_1^*t_2)\Delta a_{12}\rangle\right\} \tag{4.3.3}$$

This approach is presently under investigation.

Fig. 4.3.4 shows the superconducting transition in $Zr_{62}Ni_{38}$ as measured by electrical resistance changes at a temperature of 1.6K for different applied magnetic fields. The as quenched sample shows a very broad transition which has been seen before in other Zr based metallic glasses[26]. It was suggested that such behavior, coupled with other superconducting anomalies like the enhancement of H_{c2} at low temperature, may be due to spatial inhomogeneities on a scale of the order of the superconducting coherence lenght[27]. They proposed the existence of a distribution of electronic diffusivity $D=1/3v_f\ell$ due to variations in short-range order or to fluctuations in composition. This assumption would be in agreement with Kroeger et al.[5] who proposed the existence of clusters of Zr_3Ni_2 and Zr_2Ni together with unassociated atoms in the amorphous matrix. After the heat treatment beyond the first exotherm, we observe a sharp transition characteristic of homogenous phases, even though the heat treated sample shows clearly in fig. 4.3.5 two distinct phases. The upper critical field indicated by the arrows in fig. 4.3.4, is shown vs the temperature in fig. 4.3.5. The anomalous linear $H_{c2}(T)$ behavior is noticeable in the as quenched sample since curvature should be observable for the lowest measured temperatures.

Table IV.3.2 gives the T_c, critical field gradient $\left.\frac{dH_{c2}}{dT}\right|_{T_c}$ and the average electronic diffusivity $D=1/3v_f\ell$ (ℓ is the average electronic mean free path, v_f is the average Fermi velocity) for the different phases using the relation[28]:

$$\left.\frac{dH_{c2}}{dT}\right|_{T_c} = \frac{4k_B c}{\pi e D} \qquad (4.3.4)$$

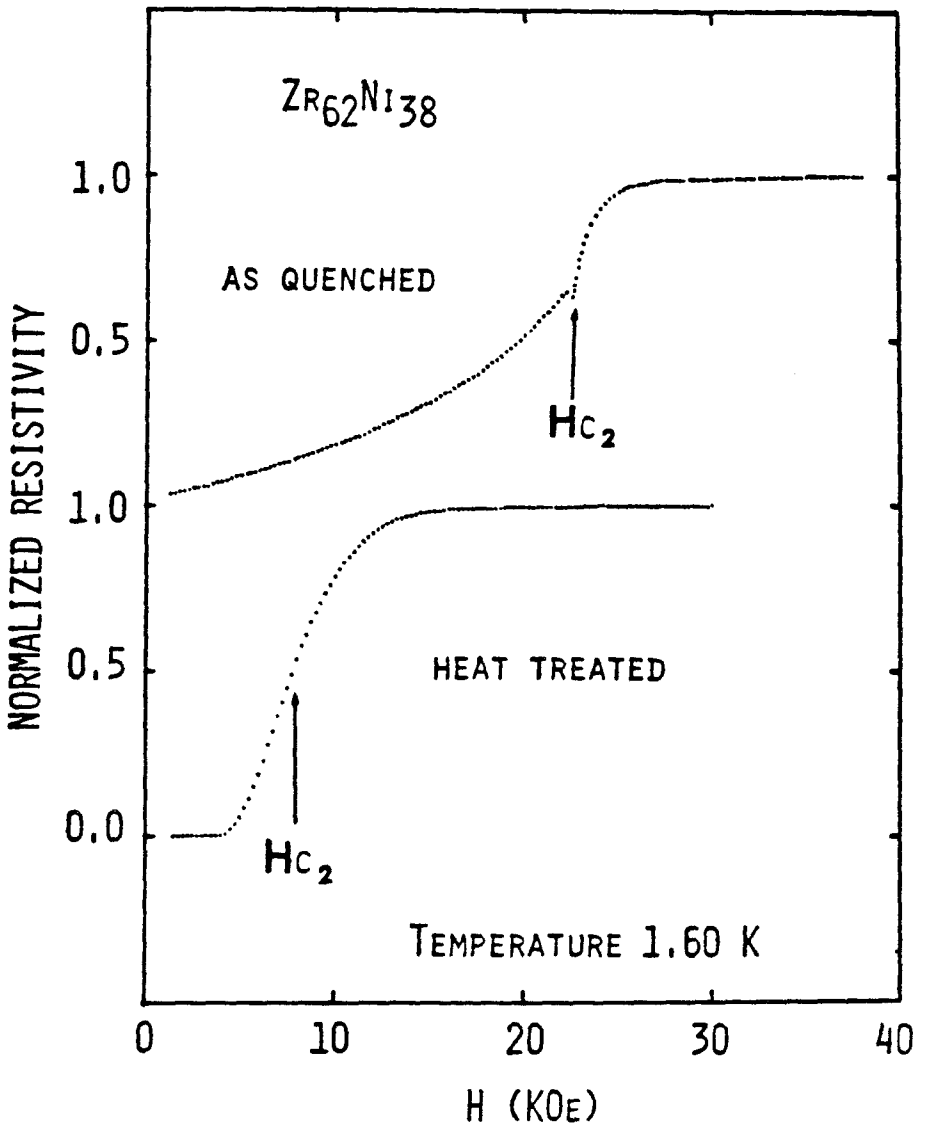

Fig. 4.3.4

Superconducting transition measured resistively for $Zr_{62}Ni_{38}$ as quenched and heat treated beyond the first exotherm.

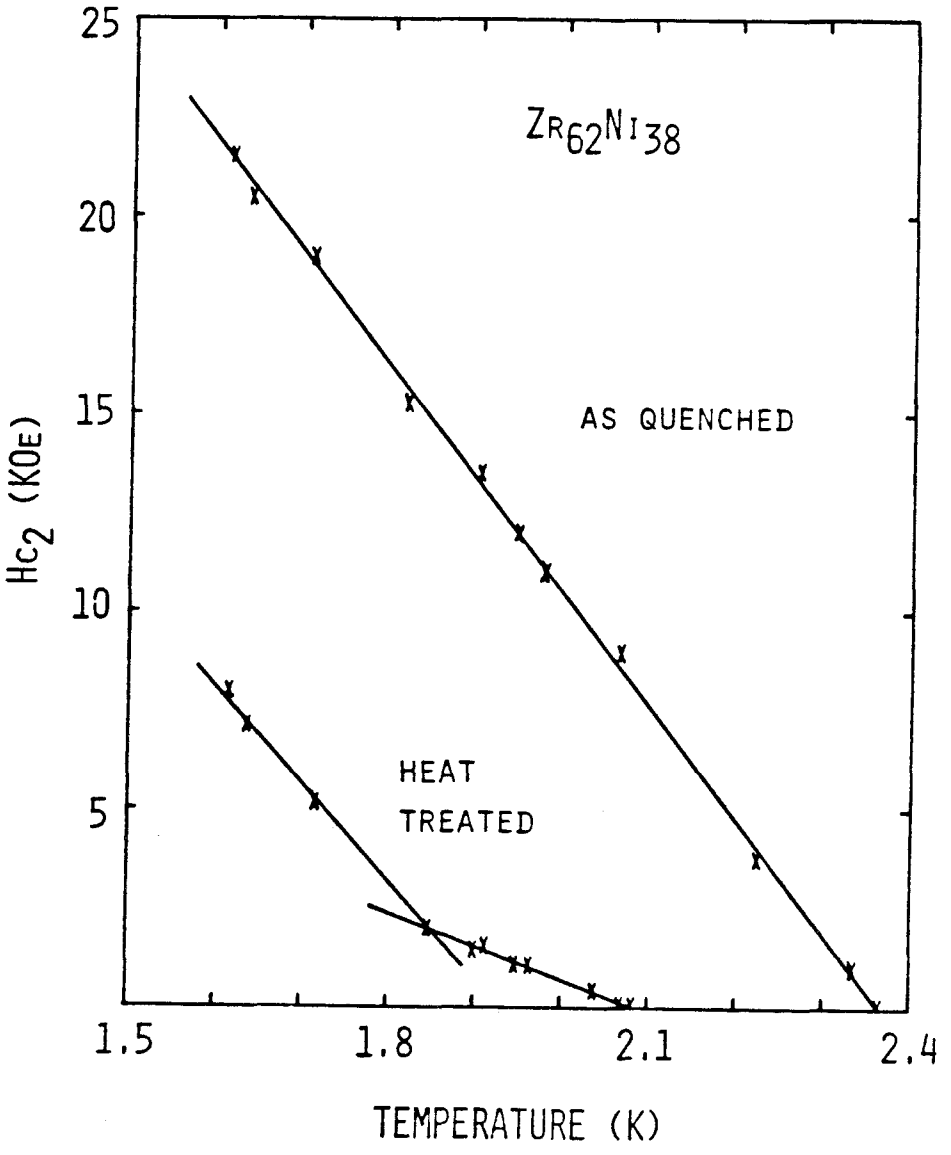

Fig. 4.3.5

Upper critical field vs temperature for $Zr_{62}Ni_{38}$ as quenched and heat treated beyond the first exotherm at a heating rate of 15°C/min.

Where c is the speed of light, k_B is the Boltzmann constant and e is the electronic charge.

Table IV.3.2

Superconductivity transitions, critical field gradients and average electronic diffusivities for as quenched and heat treated $Zr_{62}Ni_{38}$.

	PHASE	T_c(K)	$\left.\frac{dH_{c2}}{dT}\right\|_{T_c}$ (KG/K)	D(cm^2/s)
As quenched		2.36	28.6	0.384
Heat treated	Phase 1	1.92	25.5	0.430
	Phase 2	2.09	8.0	1.371

The Tc of the as quenched sample is slightly lower than the one reported by Kroeger et al.[5] for the same composition (2.50K). Many possible reasons can account for this discrepancy: 1) The state of relaxation of the glass. We know that T_c decreases upon free volume relaxation and we use melt-spun ribbons whereas Kroeger's specimens were quenched by arc-hammer. 2) The difference in the measuring technique. Our result comes from the extrapolation of the H_{c2} vs T curve whereas, Kroeger's result comes from specific heat. Finally, 3) we cannot omit the possibility of a slight offset in the concentration of the alloy. After heat treatment, phase 1, with the T_c of 1.92K has almost the same critical field gradient or average electronic diffusivity as the amorphous as quenched sample whereas, phase 2, with the T_c of 2.09K has an average electronic diffusivity more than three times larger. We thus consider phase 1 as the remaining amorphous state after the phase transition. From a plot of T_c vs composition[5]

we evaluated his concentration at ~56 At% Zr. It is worth mentioning that this concentration corresponds to the maximum in the resistivity vs concentration curve for the Zr-Ni system[29].

The resistivity of $Zr_{55}Ni_{45}$ is 185 $\mu\Omega$ cm whereas the initial amorphous $Zr_{62}Ni_{38}$ is 174$\mu\Omega$cm[1,29]. This represents an increase of 6.3% which is exactly the jump height observed in the resistivity during the first exotherm. This correlation suggests that phase 1 dominates the transport properties at high temperature. The resistivity would seem to be unaffected by the relatively high conducting phase 2 even though phase 2 is observable at low temperature from superconducting measurements monitored by resistance changes.

Fig. 4.3.6a and b show transmission electron micrographs for a heat treated $Zr_{62}Ni_{38}$. The pictures show a distribution of dark speckles ranging from 10 to 30Å in diameter. Agglomeration of these speckles produces the dark patches (average size 100-200Å) in the micrograph . Fig. 4.3.7a shows the electron diffraction pattern of a selected area of fig. 4.3.6a free of pits and holes. The pattern shows only a broad single halo and from it, there is no evidence for phase separation or crystallization. When the area under investigation includes holes or large pits we can detect crystals in the diffraction pattern, fig. 4.3.7b. This reflects probably the presence of easy crystallization sites for heterogenous nucleation or oxide films. J.L. Walter et al.[30] noticed oxide films at the bottom of deep pits in their thinned TEM samples of Zr_2Ni.

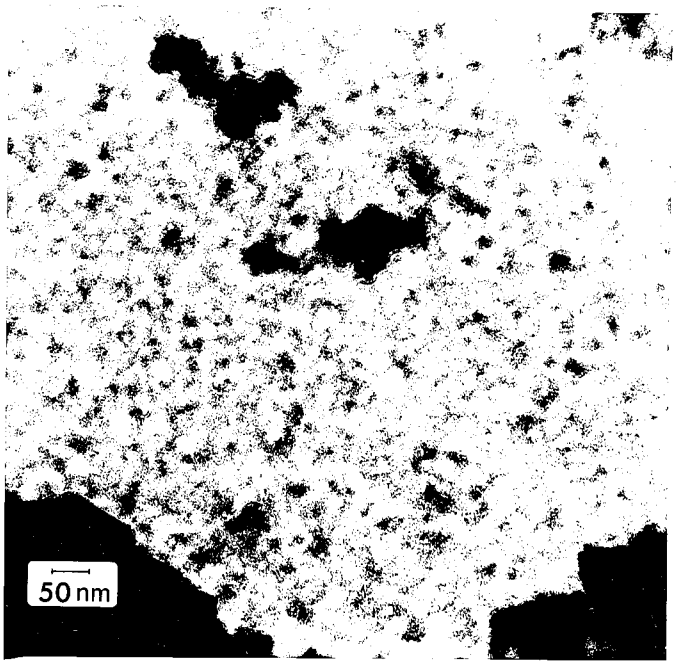

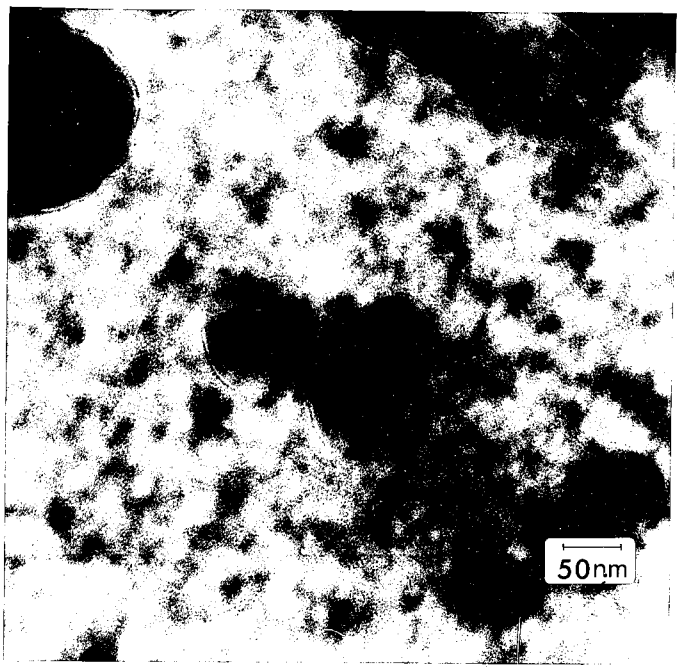

Fig. 4.3.6

(a) and (b) TEM micrographs of heat treated $Zr_{62}Ni_{38}$.

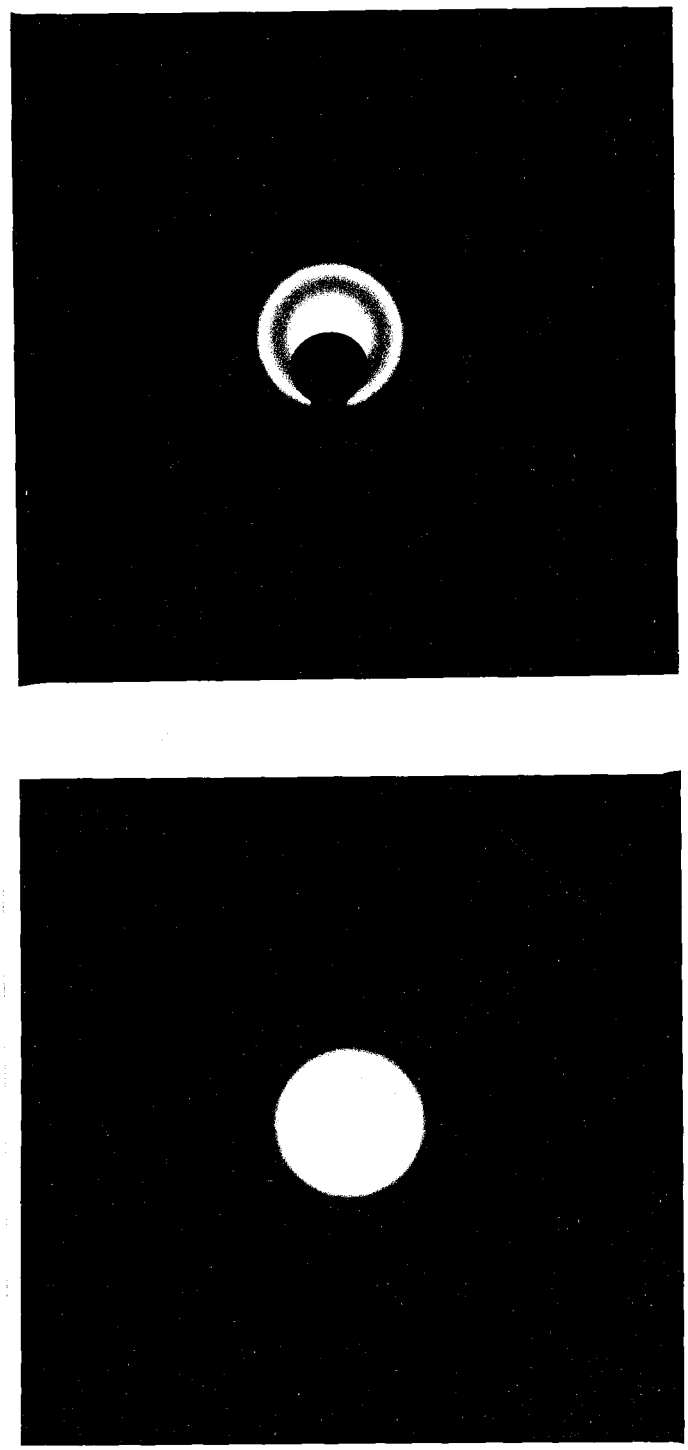

Fig. 4.3.7

Diffraction pattern of heat treated $Zr_{62}Ni_{38}$ (a) selected area in fig. 4.3.6 containing no pits and holes (b) area including holes and sample's edges.

In order to investigate the local short range order of this new phase we introduce Fe as a probe element in the matrix and perform Mossbauer experiments. Fig. 4.3.8 shows spectra of $(Zr_{62}Ni_{38})_{99.8}Fe_{0.2}$ in the as quenched condition, heat treated beyond the first exotherm and fully crystallized after the second. The spectra were analyzed using least square fit of multiple Lorentzian lines with variable height and width. Table IV.3.3 gives the average quadrupole splitting corresponding to the different sites. Our results are very similar to the ones reported by Wagner et al.[31] on $Zr_{95-x}Ni_xFe_5$. These authors discuss the similarities between the Mossbauer parameters of the stable crystalline phase (Δ Eq = 0.537) which, as in the present case, is mainly tetragonal $Zr_2Ni(Fe)$ ($CuAl_2$ type structure) and the average parameters observed in amorphous Zr-Ni-Fe (Δ Eq =0.608). They suggest that the average Fe environment in the glass might be like that of Fe in crystalline $Zr_2Ni(Fe)$. This would be in agreement with the presence of Zr_2Ni type associates in the amorphous state as suggested by Kroeger et al.[5]. In this environment each Fe atom is surrounded by Zr atoms only, with the average coordination of 8 Zr atoms arranged in an archimedian antiprism capped by 2 Fe atoms. The Zr sites have 11 Zr and 4 Fe atoms as first neighbors. The heat treated sample shows two very distinct sites. Site 1 has almost the same average quadrupole splitting as in the as quenched sample. This site corresponds to phase 1 in Table IV.3.2 and represents the Ni enriched amorphous matrix. Site 2, which must be representative of phase 2 in table IV.3.2 has a relatively large quadrupole splitting (0.931mm/s). This value is almost identical to the one reported by Vincze et al.[32] for

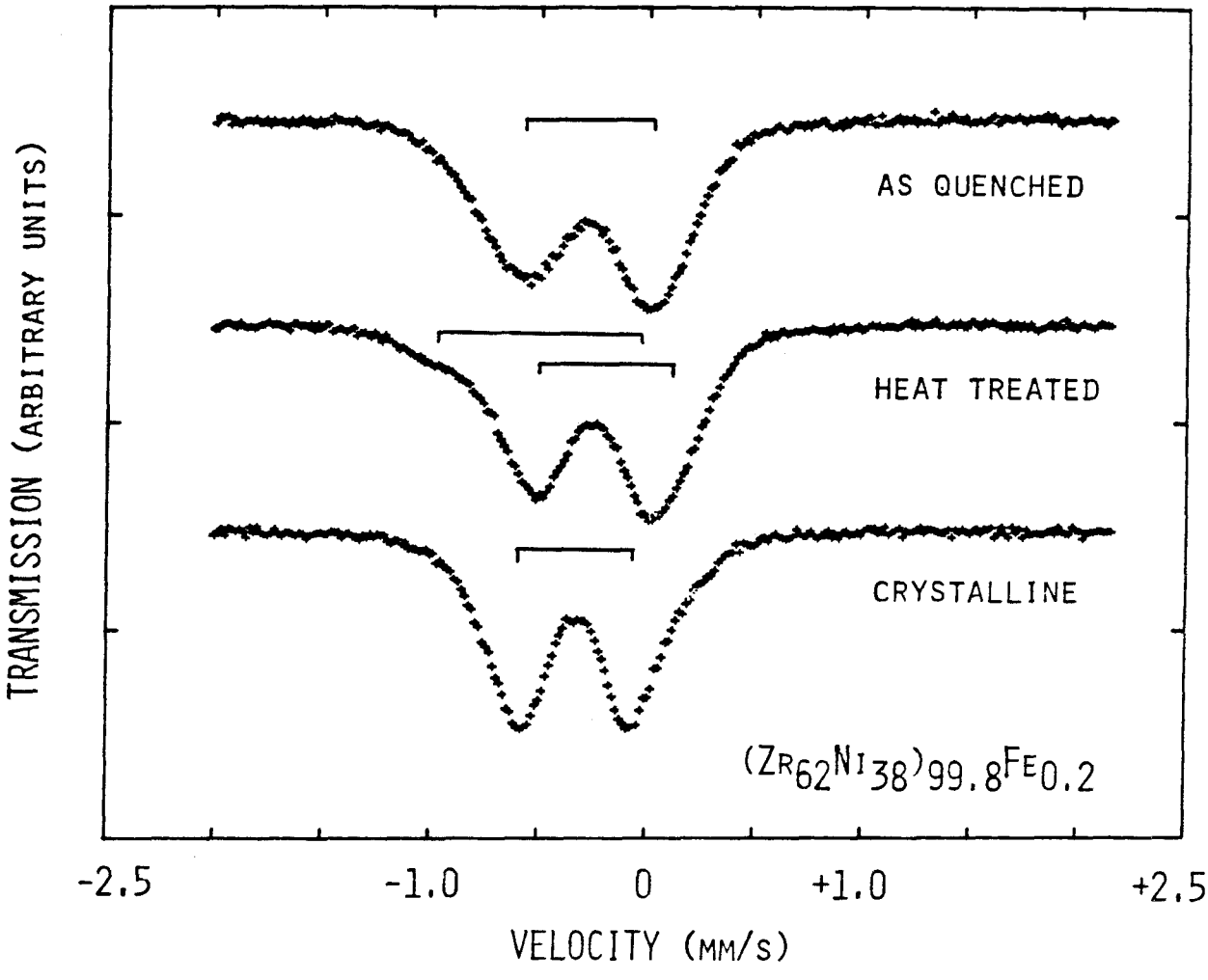

Fig. 4.3.8

Mossbauer spectra of $(Zr_{62}Ni_{38})_{99.8}Fe_{0.2}$ as quenched, heat treated beyond the first exotherm and fully crystallized after the second exotherm.

Fe in orthorhombic Zr_3Fe (Re_3B type). If Fe substitutes for Ni in the amorphous matrix and behaves in the same manner as Ni during the phase transition associated with the first exotherm, the above results would suggest the existence of a new metastable phase Zr_3Ni orthorhombic. In this environment the Fe site has 6 Zr atoms first neighbors and 3 Fe atoms somewhat further, while the two Zr sites have 2 Fe and 12 Zr in one case, 3 Fe and 11 Zr in the other case. This structure has a lower number of Zr-Ni(Fe) neighbors and a larger number of Zr-Zr neighbors than the one found by Wagner and Lee[21] for amorphous $Zr_{65}Ni_{35}$. Precipitation of an orthorhombic $Zr_3Ni(Fe)$ would then be consistent with the reduction in the number of Zr-Ni and the increase in the number of Zr-Zr observed in the RDF after heating beyond the first exotherm.

Table IV.3.3

Quadrupole splitting for different sites in $(Zr_{0.62}Ni_{0.38})_{99.8}Fe_{0.2}$ alloys.

ALLOY'S TREATMENT	QUADRUPOLE SPLITTING (mm/s)	REMARK
As quenched	0.608	Fit to two Lorentzians
Heat Treated 1 site	0.615	Fit to four Lorentzians
Heat Treated 2 site	0.931	Fit to four Lorentzians
Crystalline	0.537	Fit to two Lorentzians

CONCLUSION

The phase transition which occurs during the first exotherm in $(Zr_{1-x}Hf_x)_{62}Ni_{38}$ metallic glasses implies precipitation of very small "microcrystallites" (10-20Å size) too small to give rise to sharp rings in the diffraction pattern. The overall number of Zr-Ni neighbors decreases and the number of Zr-Zr neighbors increases. The resistivity increases because the Ni enriched amorphous matrix that remains after precipitation has a higher electrical resistivity than the original amorphous phase, thus overcompensating the influence of the highly conducting precipitates. Agglomeration of the "microcrystallites" into zones larger than the superconducting coherence length gives rise to two distinct observable phases from the $H_{c2}(T)$ curve. The Mossbauer results on samples with Fe introduced as a probe element might suggest that precipitation of metastable very fine grained microcrystalline $Zr_3Ni(Fe)$ is occurring during the first exotherm.

REFERENCES

1. Z. Altounian, Tuo Guo-hua and J.O. Strom Olsen (preprint).

2. O. Chipman, L. Jennings and B.C. Giessen, Bull. Am Phys. Soc. 23 (1978) 467.

3. K.H.J. Buschow, B.H. Verbeek and A.G. Dirks, J. Phys. D 14 (1981) 1087 - 97.

4. Y.D. Dong, G. Gregan and M.C. Scott, J. Non Cryst Solids, 43 (1981) 403 - 415.

5. D.M. Kroeger, C.C. Koch, C.G. McKamey and J. O. Scarbrough (preprint)

6. M. Mehra, R. Schulz and W.L. Johnson, J. Non Cryst. Solids, 61 & 62 (1984) 859 - 864.

7. G.S. Cargill III, Sol. St. Phys. 30 (1975) 227, and A.Williams, PhD Thesis, California Inst. of Tech., Pasadena Ca. (1981).

8. Z. Altounian, Tu Guo-hua and J. O. Strom Olsen J. Appl. Phys. 53 (1982) 7.

9. R. Schulz (unpublished results).

10. P.J. Cote and L.V. Meisel, Phys. Rev. Lett., 39 (1977) 102 - 105; Phys. Rev. B 15 (1977) 2970; 16 (1977) 2978.

11. S.R. Nagel, Phys. Rev. B 16, 4 (1977) 1694.

12. H.S. Chen and D. Turnbull, J. Chem. Phys. 48 (1968) 2560.

13. P.L. Maitrepierre, J. Appl. Phys. 41 (1970) 267.

14. E. Balanzat, J. Hillairet, J. Phys. F 12 (1978) 2907.

15. J. Hillairet, Emmanuel Balanzat, N. Derradji and A. Chamberod, J. Non Cryst. Solids 61 & 62 (1984) 781 - 786.

16. N.F. Mott, J. Inst. Metals 60 (1937) 267.

17. P.K. Rastogi and Pol Duwez, J. Non Cryst. Solids 5 (1970) 1 - 16.

18. R. Schulz, M. Mehra and W.L. Johnson (In press).

19. R. Schulz, K. Samwer and W.L. Johnson, J. of Non Cryst. Solids 61 & 62 (1983) 997 - 1002.

20. D. M. Kroeger, C.C. Koch, J.O. Scarbrough and C.G. McKamey Phys. Rev. B (In press).

21. C.N.J. Wagner and D. Lee, J. de Phys, C8 41 (1980) 242-245.

22. D. Srolovitz, T. Egami, and V. Vitek, Phys. Rev. B 24 (1981) 6936 - 6944.

23. T.E. Faber and J.M. Ziman, Philos. Mag 11 (1965) 153.

24. O. Dreirach, R.Evans, H.J. Guntherodt and J-U Kunzl, J. Phys. F2 (1972) 709.

25. Y. Waseda and H.S. Chen, Phys. Status. Solidi A 49 (1978) 387.

26. M.G. Karkut R.R. Hake, Phys. Rev. (1983) (in press).

27. W.L. Carter, S.J. Poon, G.W. Hull Jr., and T.H. Geballe Solid State Comm. 39 (1981) 41.

28. E. Helfand and N.R. Werthamer, Phys. Rev. Lett. 13 (1974) 686; Phys. Rev. 147 (1966) 288.

29. Z. Altounian, C.L. Folles, W.B. Muir and J.O. Strom-Olsen, Phys. Rev. B 27 (1983) 1955 - 1958.

30. J.L. Walter, Z. Altounian and J.O. Strom-Olsen, J. Non Cryst. Solids 61 & 62 (1984) 469 - 474.

31. H.G. Wagner, M. Ghafari, H.P. Klein, U. Gonser, J. Non Cryst. Solids 61 & 62 (1984) 427 - 432.

32. I. Vincze, F. Van der Woude and M.G. Scott, Solid State Comm., 37 (1981) 567-570.

V. EVIDENCE FOR d-BAND CONDUCTION IN METALLIC GLASSES

In this chapter a discussion will be given on the electrical resistivity of metallic glasses containing transition metal elements. The case of $(Mo_{0.6}Ru_{0.4})_{100-x}B_x$, $Zr_{100-x}Ni_x$ and $Zr_{100-x}Cu_x$, which were discussed in chapter IV, will be treated in detail. These systems are characterized by strong scattering and have a conventional mean free path on the order of the interatomic spacing. In this limit, as discussed before, the applicability of the Boltzmann formalism is doubtful and therefore the Ziman theory should be applied with caution.

Most of the theoretical understanding of the electrical transport in metallic glasses, involving transition metal elements, is based on the extended Ziman theory[14,18,58]. In this theory, Evans et al.[18] reinterpret Mott's classic explanation of the high resistivity of crystalline transition metals[6] and apply it to liquid transition metals using the Ziman formalism originally developed for simple liquid metals. First, we shall then briefly review Mott's theory.

Transition metals are characterized by a high density of d states at the Fermi level $N_d(E_f)$. Some parts of the Fermi surface are s-like and some parts d-like. The total potential (phonon, impurities...) induces transitions from the s-like part of the Fermi surface to the d-like part with a high probability since the rate is proportional to the density of the final states, $N_d(E_f)$. The relaxation time of an s electron in transition metals is then much less than an s electron in simple metals because of the absence of the empty d states at the Fermi level in this latter case. The relaxation time τ_d for the d-like part of the Fermi surface is comparable with τ_s because it

implies mainly d-d scattering for which the probability of transition is also proportional to $N_d(E_f)$. Fluctuations in the distance between neighboring atoms will induce changes in the width of the d-band by modifying the energy overlap integrals, I, in the tight binding approximation. These perturbations will affect the "hopping frequency" of the electrons towards the nearby sites and represent the starting point for calculating the d-d scattering[60,61]. The conductivity of a crystalline transition metal, in this two band model, can be separated into an s part and a d part.

$$\sigma = \sigma_s + \sigma_d$$

The velocity v_s of an s electron at the Fermi surface is much greater than v_d therefore its mean free path $\ell_s = v_s \tau_s$ is also much larger than the mean free path of a d electron. It follows that:

$$\sigma_s >> \sigma_d$$

In the generalized Ziman theory Evans et al.[18] considered the current to be carried by free electrons in plane wave states. These waves are scattered resonantly on the Fermi sphere by a "muffin-tin" potential. They replaced in the original Ziman formula the weak pseudopotential by a t-matrix. For transition metals, the d-phase shift η_2 dominates and therefore, in this picture, the resistivity comes from the d resonant scattering of the conduction electrons. These electrons are assumed to be s-like, the d electrons are considered to be immobile.

Let us write the s-d matrix element as:

$$J = \int \psi^{*}_{s,p} \, V \, \psi_{d} \, dv$$

where $\psi_{s,p}$ represents the conduction electron wave function made up of s and p orbitals, and V is the total potential. If, as before I represents the energy overlap integrals between adjacent atoms, Mott[62] pointed out that the Evans theory is valid if and only if the time taken for an electron to move from a d state in one atom to a d state in an adjacent atom, h/zI, (where z is the coordination number) is larger than the jump time from an s to a d state, h/J. If this condition is not fullfilled, the resonance required by the Evans theory cannot be built up. For this reason Mott believes that their theory is incorrect for pure liquid transition metals because of the large coordination number and overlap integral[62].

In amorphous transition metals alloys, for which the average coordination number can be even larger, the same argument should apply and a model involving s-d transitions and different mean free paths for s-p and d electrons should be more appropriate.

Amorphous metals alloys are known to approach the extreme dirty limit. The scattering is so strong that the conventional mean free paths of both s and d electrons are on the same order of magnitude as the interatomic spacing. In this limit of incipient Anderson localization, perturbation theory and the Boltzmann-equation formalism break down, and the conductivity must be evaluated using the Kubo formula. In this extreme regime, the electrons should be thought of as diffusing around rather slowly or even as hopping between quasi localized states rather than being occasionally scattered between

nearly coherent plane-wave states. Girvin and Jonson[63] showed that the adiabatic-phonon assumption also fails in this limit and phonons actually assist the mobility, producing an anomalous negative temperature coefficient of resistivity. Such negative temperature coefficient is observed in all the samples discussed in this thesis. This phenomenon is known to occur for localized states in the form of phonon-assisted hopping but it actually occurs even before localization is reached. Recently R.W. Cochrane et al.[6] reinterpreted the low temperature resistivity anomaly found in several amorphous metals as being a precursor effect of a localization transition in a three-dimensional interacting electron system. They found that the conductivity scales with the ones observed in other systems having typical resistivity an order of magnitude larger, and in which, metal-insulator transition is found.

Using the Kubo formalism, Ballentine et al.[64] have calculated, for clusters of 365 atoms, the conductivities of several liquid transition metals. They treated the s and d states on an equal footing and evaluated their relative contributions to the conductivity. They found that the sd contribution to the conductivity is usually very small and thus wrote:

$$\sigma \approx \frac{e^2}{\Omega} \left(D_s N_s(E_f) + D_d N_d(E_f) \right) \qquad (5.1)$$

$N_s(E_f)$ and $N_d(E_f)$ are the s and d partial densities of states and D_s and D_d are the respective electronic diffusivity. They found that for liquid La the d states comprises 90% of the density of states at the Fermi energy and contributes to 87% of the conductivity. Including hybridization, a diffusivity ratio D_s/D_d of only 1.1 was found

indicating very little dynamical difference between the s-like and the d-like states at the Fermi energy. Even if the diffusivity ratio is much larger for other liquid transition metals like Cr, Mn and Fe the d states are still responsible for about 85% of the conductivity because of the very large d component of the density of states. In a first approximation for those liquid transition metals we have:

$$\sigma \approx \frac{e^2}{\Omega} D_d N_d(E_f) \qquad (5.2)$$

Let us now return to metallic glasses and let us first consider the case of $(Mo_{0.6}Ru_{0.4})_{100-x}B_x$ glasses which has been extensively studied in the literature[65-67] and also discussed in chapter IV.

Fig. 4.2.9 in chapter IV showed a linear relationship between the conductivity and the density of states at the Fermi level for $(Mo_{0.6}Ru_{0.4})_{100-x}B_x$ across the whole concentration range for which the glass can be made amorphous. The values of γ were obtained from calorimetric measurements[66] and the data were normalized to the respective values for boron 18. We observe in this figure a straight positive slope. The s-d scattering model would predict an opposite behavior (i.e. an increase of resistivity with an increase in the density of d states at the Fermi level) if the number of free carriers is constant in this range of concentration. Fig. 5.1 shows the upper critical field gradient which is related to the average electronic diffusivity by[68]:

$$\left.\frac{dH_{c2}}{dT}\right|_{T_c} = \frac{4k_B c}{\pi e \bar{D}} \qquad (5.3)$$

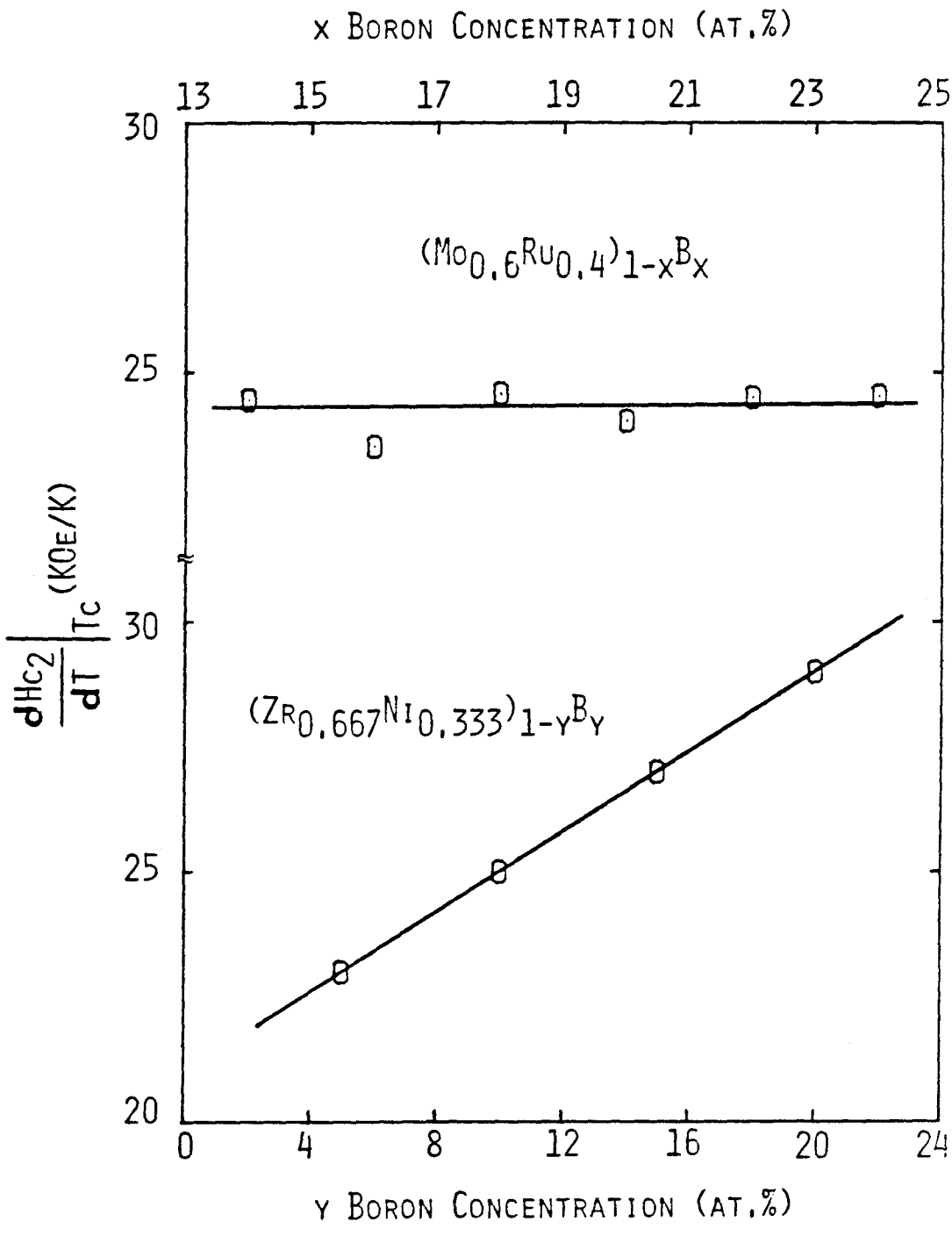

Fig. 5.1

Upper critical field gradient vs concentration for Mo-Ru-B and Zr-Ni-B systems.

This upper critical field gradient is independent of the boron concentration for the Mo-Ru-B system. Based on an abrupt discontinuity in the slope of the resistivity vs concentration at x=18, Johnson et al.[65] proposed the existence of two different types of defects with two different scattering mechanisms for x<18 and x>18. Figs. 4.2.9 and 5.1 suggest, that only one mechanism is valid over the whole concentration range. Because the density of d states at the Fermi level is fairly large in Mo-Ru-B glasses ($N_d(E_f)$ = 1.57 states/ev-atom for x=14), the average electronic diffusivity represents basically the d state diffusivity (as long as the D_s/D_d ratio is relatively small like in the case of liquid La). If eq. 5.2 is valid for Mo-Ru-B, and if

$$\bar{D} \approx D_d \tag{5.4}$$

it follows from 5.2, 5.3 and 5.4 that

$$N_d(E_f) = \left(\frac{\pi\Omega}{4ek_B c} \cdot \left.\frac{dH_{c2}}{dT}\right|_{T_c} \right) \sigma \tag{5.5}$$

This equation is basically analogue to the one predicted by the Ginsburg-Landau-Abrikosov-Gor'kov theory for the density of states in the extreme dirty limit. The slope of the density of states vs conductivity is then proportional to the upper critical field gradient at T_c. For $(Mo_{0.6}Ru_{0.4})_{100-x}B_x$, $\left.\frac{dH_{c2}}{dT}\right|_{T_c}$ is constant and we observe a linear relationship between N_d and σ across the whole concentration range. The least square fit between the density of

statesand the conductivity data corrected by the average atomic volume at each composition, gives an upper critical field gradient of 24.03 KG/^{o}K, in good agreement with the experimental average data of 24.21 KG/^{o}K. Fig. 5.1 shows that for $(Zr_2Ni)_{100-y}B_y$ glasses, the upper critical field gradient increases linearly with concentration from 23 KG/^{o}K for y=5 to about 30 KG/^{o}K for y=25. This gives rise to the curvature observed in fig. 4.2.9 for the Zr-Ni-B system. The data, in this case, are from reference 69 and they are normalized to the density of states and conductivity of amorphous Zr_2Ni.

Among all the metallic glasses of the type $ET_{100-x}LT_x$ where ET refers to an early transition metal and LT a late transition metal the best known are Zr-Cu and Zr-Ni. Based on the strong correlations which exist between the fractional change in magnetic susceptibility and resistivity upon crystallization Z. Altounian et al.[70,71] suggest that s-d scattering effects make an important contribution to the resistivity in both Zr-Cu and Zr-Ni. This suggestion is based on the assumptions that the Boltzmann equation and the weak scattering approximation are valid in the amorphous state as well as in the crystalline state. It assumes also that the s-d scattering matrix element is the same in the two phases. There are no a priori reasons to believe that these assumptions are true, and in fact, we showed in chapter IV that even if the change in the resistivity is correlated with the change in the density of d states during crystallization in an $(Mo_{0.6}Ru_{0.4})_{82}B_{18}$ glass, they behave in opposite direction upon relaxation in the amorphous state (i.e. an increase in resistivity is associated with a decrease in the density of states). Altounian et al.[72] also showed recently that their resistivity data in

glassy Zr-Ni are consistent with the Faber-Ziman model for liquid metals and attributed the discrepancies to errors introduced by the simplifying assumptions made in applying the model. Kroeger et al.[76], on the other hand, explain some peculiarities in the variation of Altounian's resistivity data for Zr concentration larger than 55 by the presence of clusters with definite stoichiometries.

Fig. 5.2 shows a plot of the density of states vs the conductivity for the Zr-Ni system. The data are normalized to the respective values for x=55. For Zr concentration larger than 55, fig. 5.3 shows that the upper critical field gradient and, therefore the average electronic diffusivity (from eq. 5.3) is independent of concentration to within experimental uncertainty. We thus observe, as for the Mo-Ru-B case, a linear relationship between the density of states and the conductivity for x>55 (fig. 5.2). The d-states seem to dominate the conductivity in this range of concentration. For x<55, the critical field gradient decreases rapidly with decreasing Zr concentration, indicating a rapid increase in the average electronic diffusivity (fig. 5.3). The conductivity increases while the density of states at the Fermi level decreases. In this regime (x<55) fig. 5.2 shows that, in fact, if we plot the density of states vs the resistivity instead of the conductivity, we get a linear relationship. The resistivity is directly proportional to the d density of states suggesting that Mott s-d scattering of nearly free electrons is predominant in this range of concentration. In this regime $\sigma_d << \sigma_s$ and equation 5.1 becomes:

$$\sigma \approx \frac{e^2}{\Omega} N_s D_s \qquad (5.6)$$

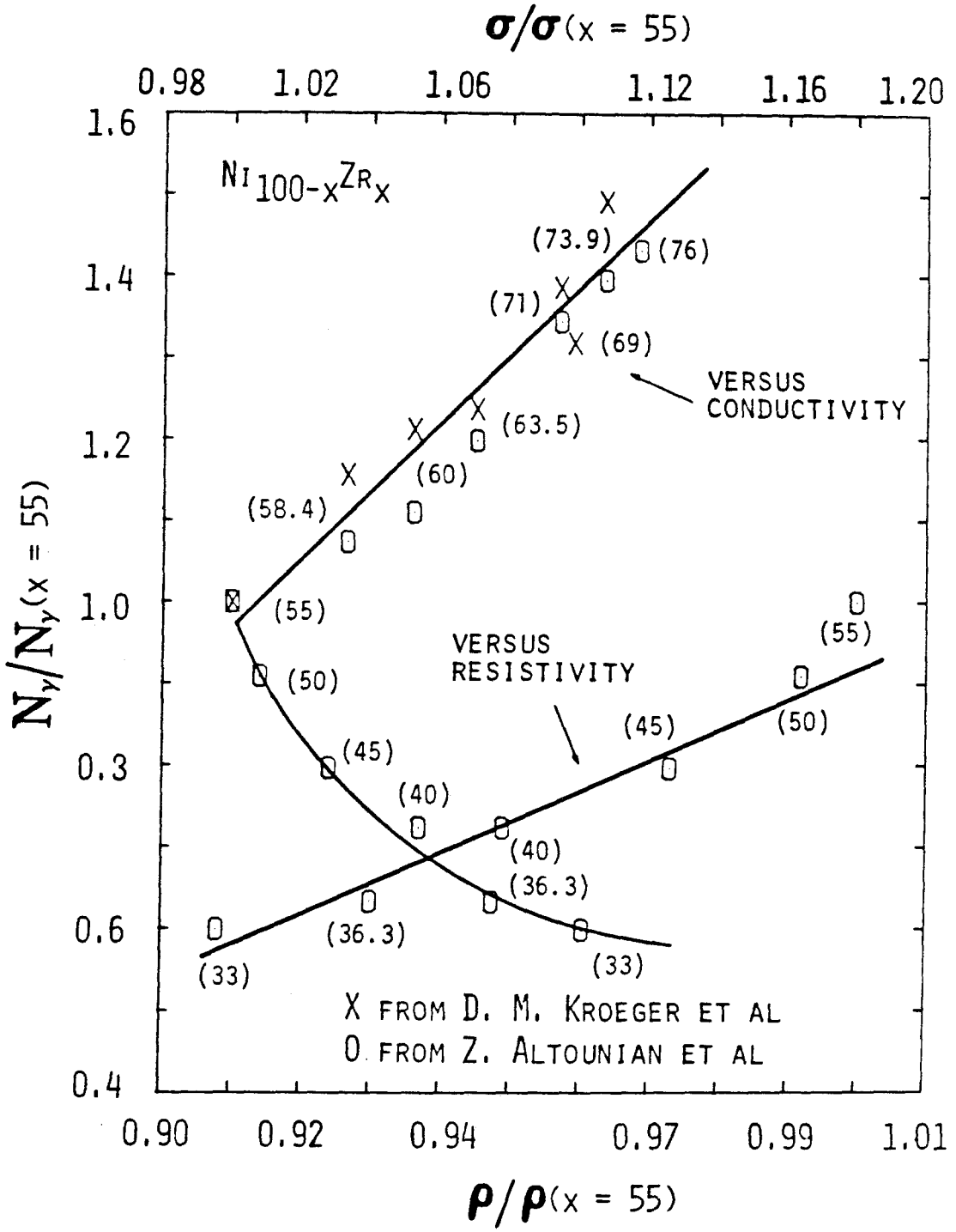

Fig. 5.2

Normalized density of states vs conductivity (or resistivity for x>55) for the Ni-Zr system. The concentrations are indicated in parenthesis. The data are normalized to the respective values for x=55.

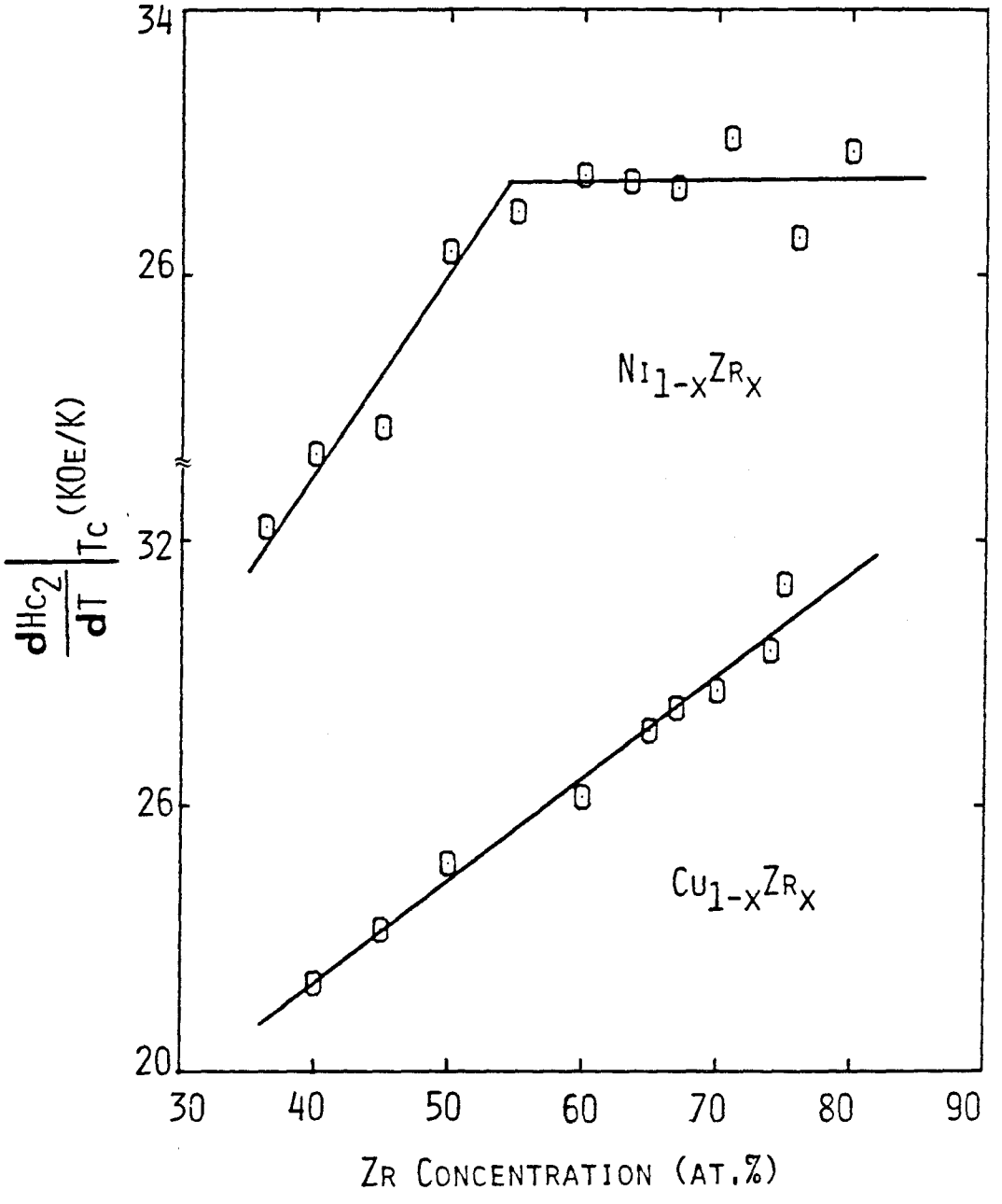

Fig. 5.3

Upper critical field gradient vs concentration for Ni-Zr and Cu-Zr systems.

N_s represents the density of s electrons or free carriers and D_s is the s state diffusivity which is proportional to the mean free path ℓ_s or the lifetime of the carriers τ_s. As it was pointed out by Altounian et al.[72], in Zr-Ni the ration Z/Ω (where Z is the valence and Ω is the atomic volume) is almost the same for both constituents so k_f and the number of free carriers should be essentially constant over the concentration range. On the Ni rich side, the density of the d states at the Fermi level is relatively small and if the diffusivity of the s states is much larger than that of the d states, the average diffusivity measured from the slope of the upper critical field will be essentially dominated by D_s and therefore equation 5.3 can be written as

$$\left.\frac{dH_{c2}}{dT}\right|_{T_c} \approx \frac{4k_B c}{\pi e D_s} \propto \frac{1}{\tau_s} \qquad (5.7)$$

The upper critical field gradient is proportional to the s-d scattering rate which, in turn, using the golden rule is proportional to the d density of states. Fig. 5.4 shows the log of the upper critical field gradient at T_c vs the log of the density of states. For the Zr-Ni system the least square fit of the data for $x < 55$ gives a slope of 1.015 in agreement with the previous discussion. Thus for a fixed number of carriers N_s and a diffusivity D_s varying, like τ_s, as $1/N_d(E_f)$ we find from equation 5.6 a direct proportionality between the resistivity and the density of states, as illustrated in fig. 5.2

Note that even if the d states diffusivity makes a non-negligible contribution to the average electronic diffusivity $\bar{D}$, we would still get a slope of one in the case where the lifetime of the

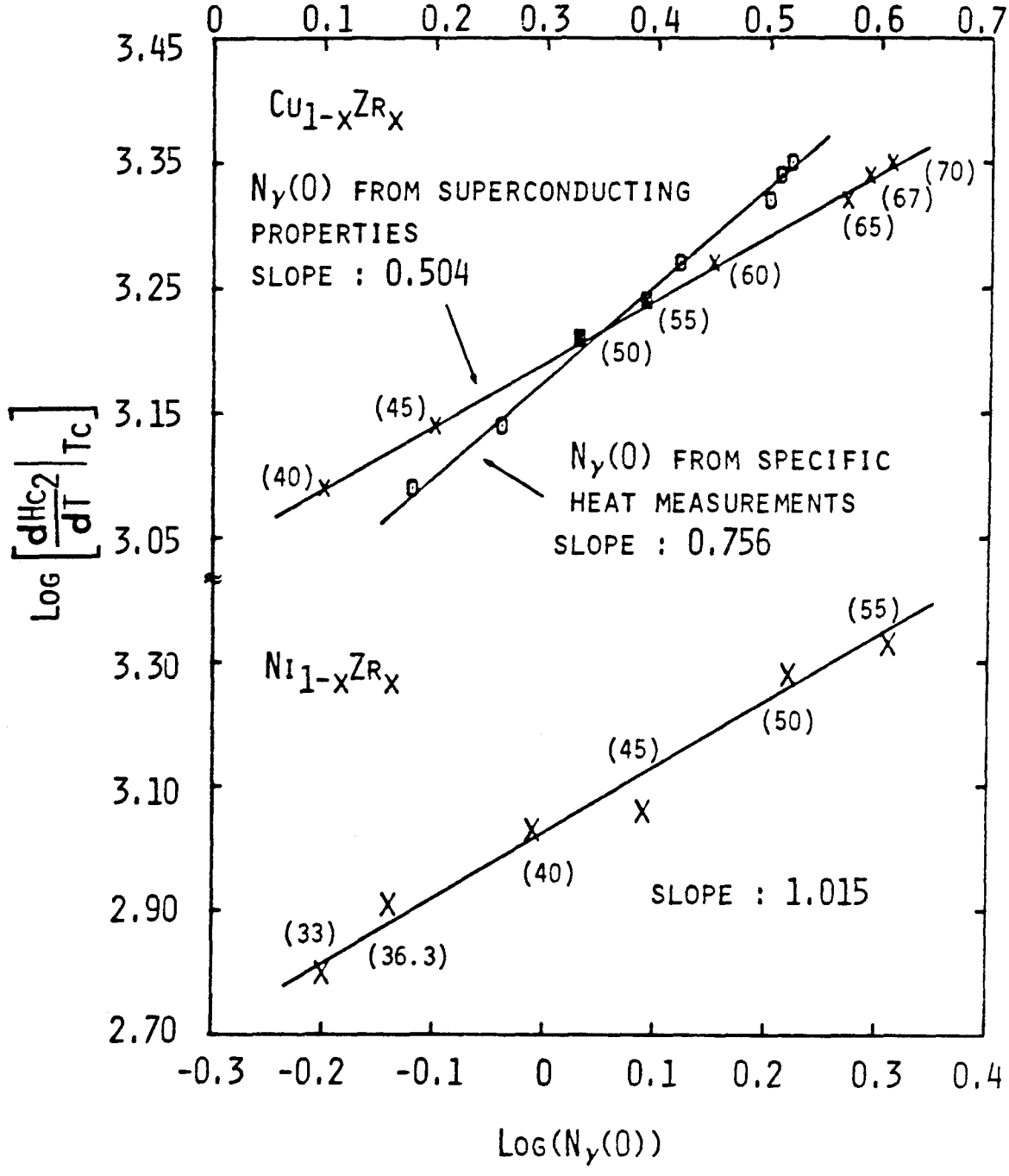

Fig. 5.4

Log-Log plot of the upper critical field gradient vs the density of states for Cu-Zr and Zr-Ni systems.

d-like states is determined by d-d scattering for which, as discussed previously, the probability of transition is also proportional to the density of d states at the Fermi energy.

We can wonder why the transition between the range where the d-states dominate the conductivity (x>55) and the one where the s-states (x<55) dominate is so sharp. A possible explanation comes from looking at fig. 5.5. Dong et al.[73] measured the positions of the peak of the first halo, Qp, in the x-ray diffraction pattern as a function of composition for the Zr-Ni system and found an apparent discontinuity around x=55. He suggests that the nature of the short range order might be different in the two ranges of concentration and this could explain why there is predominantly d-band conduction on one side and s-band conduction on the other.

The last system to be discussed is the Cu-Zr glasses. Fig. 5.3 shows that the upper critical field gradient increases continuously with Zr content over the whole range of concentration for which the alloy can be made amorphous. The rate of increase with respect to Zr concentration is, however, much lower than what is found for the Zr-Ni system. The slope of the log-log plot between the upper critical field gradient and the density of states (measured from superconducting properties) is 1/2 instead of 1 like for the Zr-Ni case (fig. 5.4). By writing the average electronic diffusivity as $\bar{D} = 1/3\bar{v}_f\bar{\ell}$ and the average electron mean free path as $\bar{\ell} = \bar{v}_f\bar{\tau}$ (where $\bar{\tau}$ is the average lifetime of the electrons at the Fermi surface) it follows from equation 5.3 and the last result that the average scattering rate $1/\bar{\tau}$ is proportional to the square root of the d density of states at the Fermi level, assuming a constant average group velocity of the

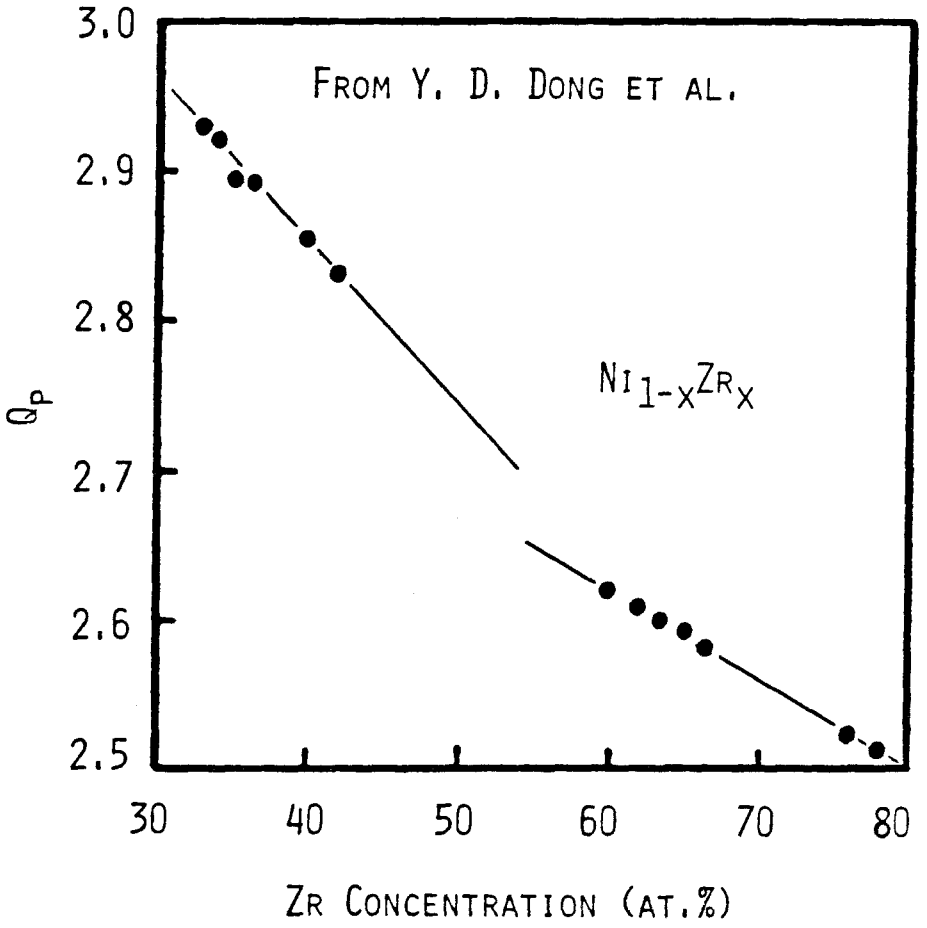

Fig. 5.5

Positions of the first peak of the structure factor vs composition for the Zr-Ni system.

electrons at the Fermi surface. This suggests that the s-d scattering model of nearly free electrons is not the only important mechanism of conduction in Cu-Zr and that the d electrons must make a non-negligible contribution, as well, in the transport.

It is interesting to note that if the density of states at the Fermi level is obtained from specific heat measurements, the slope of the log-log plot is 3/4 instead of 1/2 as we can see in fig. 5.4 For $x < 50\text{-}55$, the values of N_γ determined from calorimetric measurements are all larger than the ones obtained from superconducting properties by using the Ginsburg-Landau-Abrikosov-Gor'kov theory. For $x > 50\text{-}55$, it is the inverse. Discrepancies between the values obtained by both methods have been observed before[74,76] and attributed to uncertainties in the resistivity measurement[74], differences between specimens (state of relaxation, phase separation...)[76]. We believe that the trend observed here is too systematic to be explained by any of the above arguments. It is possible, however, that the states giving rise to the heat capacity might not be all the same as the one involved in superconducting pairing due to incipient localization.

Ching, Song and Jaswal[77] have recently calculated the electronic states in $Cu_{100-x}Zr_x$ metallic glasses using the orthogonalized LCAO method on periodic structural models containing 90 atoms. There is no assumption in the theory which makes it applicable only to weak scattering cases. They analyze each electronic state in terms of a localization index and show that the Cu d states are localized and the Zr d states are relatively delocalized. At the Fermi level, the states are delocalized but there is a tendency for a slight increase in their localization index when the Cu concentration

is increased. Since localization destroys superconductivity, this tendency of localization with increasing Cu concentration is probably related to the fact that the density of states seems to decrease faster with Cu concentration when measured from superconducting properties.

Fig. 5.6 shows that the conductivity decreases linearly with the density of states over the whole range of concentration with a different slope depending, again, whether the density of states is obtained from specific heat of from the slope of H_{c2}. The behavior is similar to the Mo-Ru-B system even though, the upper critical field gradient is not a constant. All these results on Cu-Zr can be understood if we assume that both s and d electrons are important in the conduction. Let us write the average electronic diffusivity as arising from contribution of both s and d states

$$\bar{D} = \frac{N_{s,p}}{N_{s,p} + N_d} D_s + \frac{N_d}{N_{s,p} + N_d} D_d \qquad (5.8)$$

where $N_{s,p}$ and N_d represents the partial density of states at the Fermi level and D_s and D_d have their usual meaning. Table V.1 lists the bare partial density of states obtained by Ching et al.[77] together with some other relevant data for the $Cu_{100-x}Zr_x$ system. The average electronic diffusivity has been calculated using eq. 5.3 and the upper critical field gradient from ref. 75. The conductivity, density and mass enhancement factor $(1+\lambda_{sf}+\lambda_{ep})$ are from reference 70 and 75. The mean atomic volume Ω has been determined from the density and the average atomic weight.

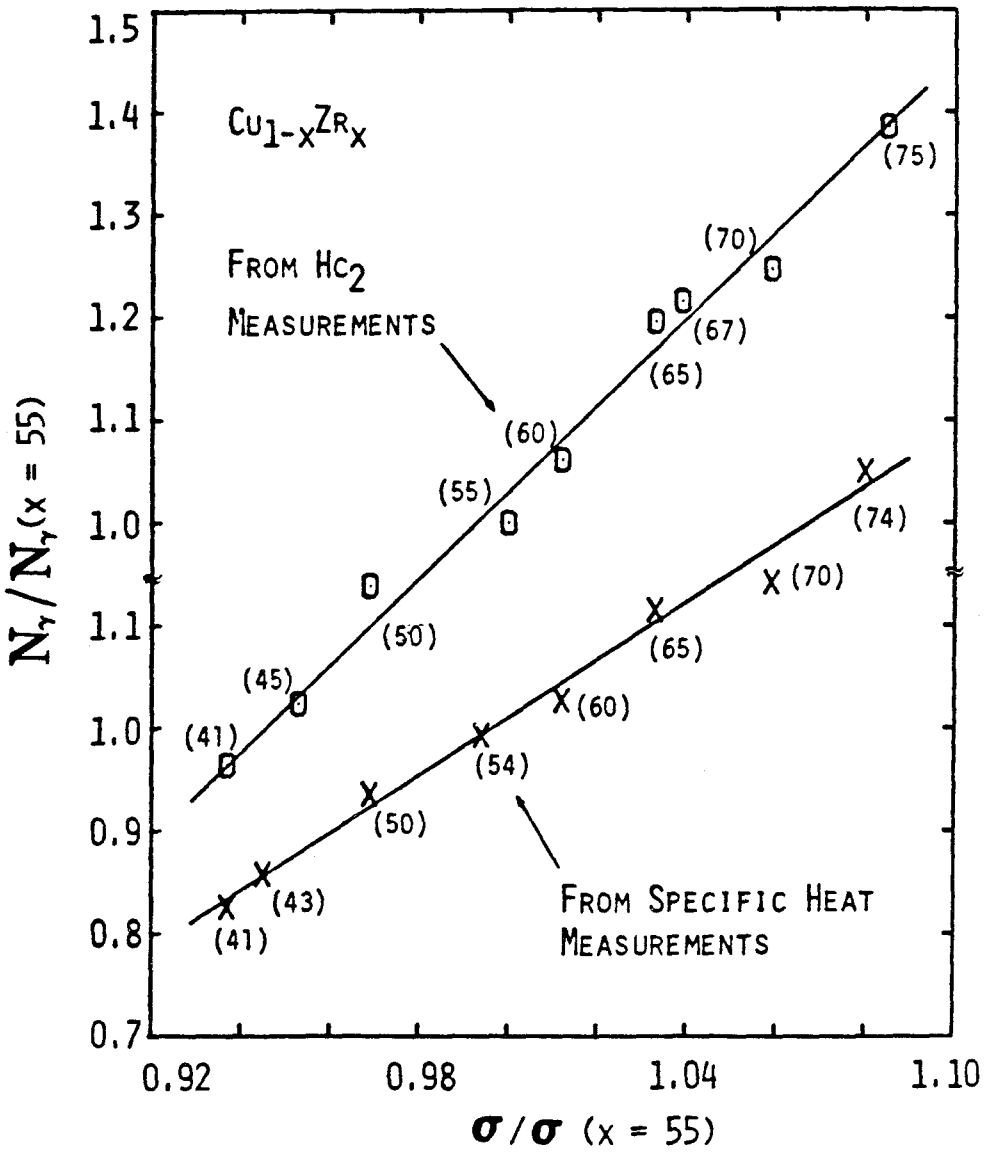

Fig. 5.6

Normalized density of states vs conductivity for the Cu-Zr system. The concentrations are indicated in parentheses and the density of states are from either calorimetric measurements or superconductivity measurements. The data are normalized to the respective values for x=55.

TABLE V.1

Electronic density of states at the Fermi level together with other parameters for $Cu_{100-x}Zr_x$ metallic glasses.

	$N(E_f)$ states/ev atom									
x	Cu4s Cu4p	Zr5s Zr5p	Cu3d	Zr4d	$\bar{D}$ x1000 (cm^2/s)	σ $(\Omega cm)^{-1}$	d (g/cm^3)	Ω $(\AA^3)$	Z_{eff}	$1+\lambda_{sf}+\lambda_{ep}$
67	.115	.187	.026	.713	0.391	6.08	6.95	19.61	1.67	1.87
50	.126	.106	.050	.577	0.451	5.65	7.25	17.72	1.50	1.68
33	.200	.057	.060	.289	0.533	5.30	7.57	15.94	1.33	1.61

The s states diffusivity is given by $D_s = 1/3 v_s \ell_s = 1/3 v_s^2 \tau_s$ where v_s is the s states velocity at the Fermi level, ℓ_s is the mean free path and τ_s is the lifetime. If we assume that the Mott s-d scattering model is the main scattering mechanism for the s electrons, it follows using the golden rule that

$$\frac{1}{\tau_s} = \frac{2\pi}{\hbar} \left| < \Psi_d \mid V \mid \Psi_{s,p} > \right|^2 N_d(E_f) \qquad (5.9)$$

then,

$$D_s = \left(\frac{\hbar v_s^2}{6\pi |<\Psi_d|V|\Psi_{s,p}>|^2} \right) \frac{1}{N_d(E_f)} \equiv \frac{\alpha}{N_d(E_f)} \qquad (5.10)$$

In ref. 46, Waseda assumed that Zr has two valence electrons per atom and Cu one. The ratio between the effective valence electrons and the average atomic volume, in that case, is almost independent of the concentration. This means that we can consider the

Fermi wave vector $k_f = (3\pi^2 Z/\Omega)^{1/3}$ and the s states Fermi velocity $v_s = \hbar^2 k_f/m$ as roughly constant across the concentration range. For a given s-d scattering matrix element, we can calculate the s and d states diffusivity from eq. 5.8, eq. 5.10 and the values, in table V.1 for the partial density of states and average electronic diffusivity.

Fig. 7a shows the results for three different parameters. The dropping off in the d states electronic diffusivity with increasing Cu concentration is associated with the increase in the d states localization index mentioned earlier, the degree of localization being related to the electron mean free path. It is interesting to note that when $\alpha=0.4$, the d states diffusivity vanishes when the Cu concentration reaches 67 At.%. Beyond this point the d electrons are essentially immobile and the conductivity is assumed entirely by the s and p electrons. If we were to increase the Cu concentration beyond this point, the density of d states at the Fermi level would still decrease and the conductivity would increase according to the Mott s-d scattering model. We would then expect a minimum in the conductivity versus concentration around 67 At.% Cu and, indeed, we find experimentally a maximum in the resistivity curve around this concentration[70,78]. Fig. 7b shows the calculated conductivities using eq. 5.1 for a parameter $\alpha=0.3$ together with the experimental points from Altounian et al.[70,75]. The bare density of states given in Table V.1 has been corrected by the mass enhancement factor $(1+\lambda_{sf}+\lambda_{ep})$ before being used in eq. 5.1. The conductivity is found to decrease over the whole range of concentration and the results are in fairly good agreement with the experimental data.

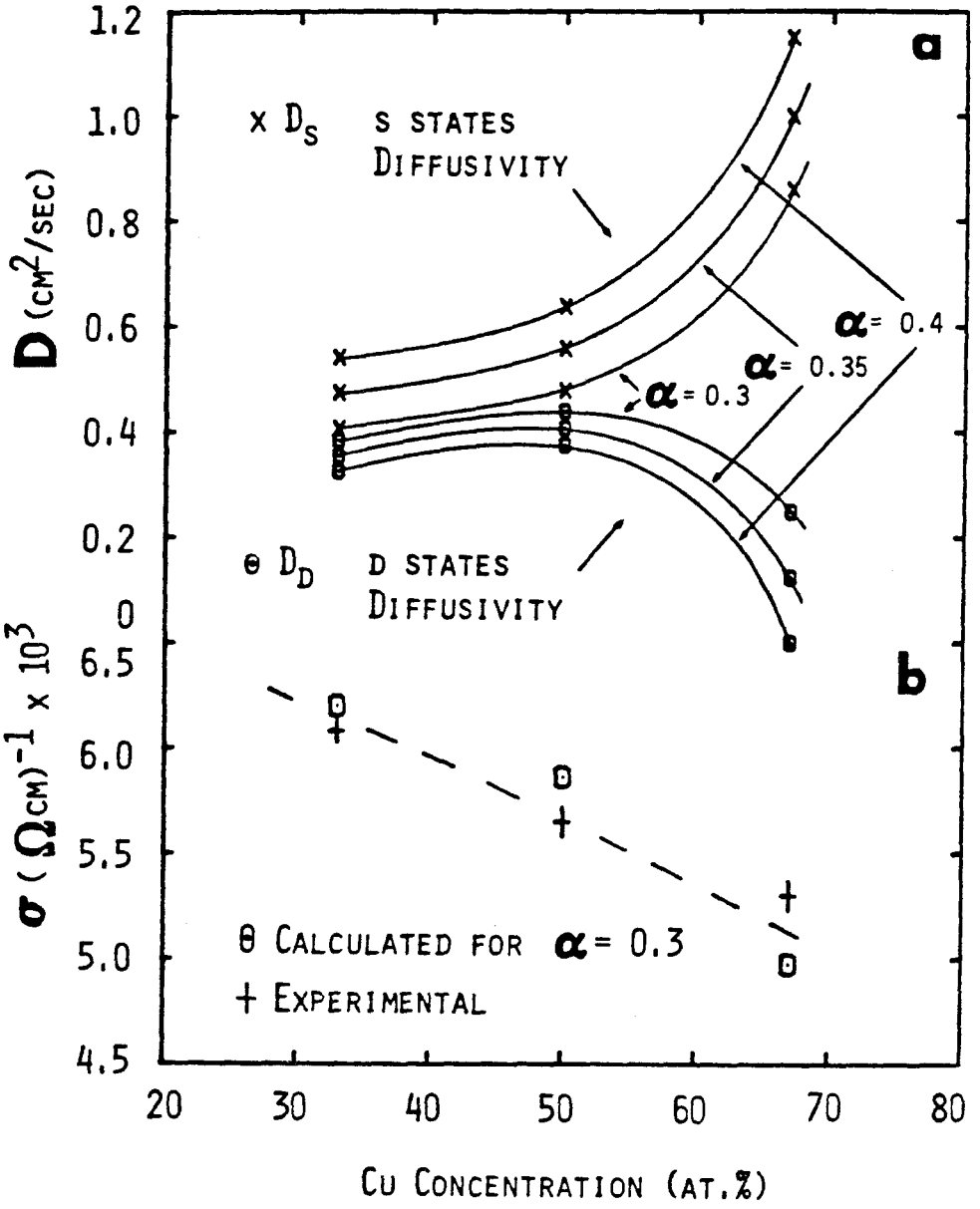

Fig. 5.7a & b

Calculated electronic diffusivity for the s and d states vs the Cu concentration for different parameters α (or s-d scattering matrix element).

Calculated conductivities for a parameter α = 0.3 together with the experimental data points from Altounian et al (ref. 70 & 75).

Even if the electrical resistivity of Cu-Zr[46] and Zr-Ni[79] has been found to be in reasonable agreement with the extended Faber-Ziman theory, the question of the applicability of this theory to systems with such a short mean free path still remains puzzling. This chapter represents an attempt to explain the behavior of the electrical resistivity in those systems from a different point of view and emphasizes the possibility of d-band conduction in these glasses.

VI. CONCLUSION

We have shown that the electrical resistivity can be used as a very convenient experimental tool to study phase separation, ordering and relaxation phenomena in metallic glasses. Each of these problems is, by itself, very important and because of the topological randomness of the structure, they are also very difficult to detect using conventional techniques like X-ray diffraction. The ability to locate them in the temperature-time diagram is already a big step. Because of the great sensitivity of electrical resistivity measurements it is possible to observe slight changes in the short range order which are invisible to other techniques. The lack of a good and reliable theory relating atomic order to electrical resistivity in metallic glasses, however, limits the power of such measurements.

In chapter II, I described some of the theoretical approaches which have been used to study these phenomena in the crystalline state. To what extent these formulas can be extended and applied to metallic glasses is still a very controversial subject. Chapter V is a warning for those who applied the Ziman formalism in the Born approximation and the free electron picture, too extensively.

It is in fact, not to hard to think of alternative ways to interpret the behavior of the resistivity during structural relaxation, without reference to the Ziman formalism. For instance, it was shown in chapter V that, quite often, in metallic glasses the conductivity is directly proportional to the density of states at the Fermi level with a constant slope given by the upper critical field gradient at T_c.

$$\sigma = \kappa\, N(E_f) \tag{6.1}$$

Several authors have calculated, using different techniques, the electronic density of states in disordered systems. In particular, the method of expansion in moments[53] using a tight binding approximation has been quite successful for studying the local density of states in amorphous metals[54]. It was found that the shape of the density of states on a given site is governed by the local radial distribution of near neighbors $G_i(r)$ and is less sensitive to the local symmetry[55]. High-density regions give rise to sharp peaks in the density of states while low density regions produce a rather flat distribution. Fig. 6.1, for instance, shows a typical example of the local density of states on a Ni site in a solid-like cell (i.e. high density region) compared with one for a liquid-like cell. Going back to the theory of Cohen and Grest (II.2.D), let $N_s(E_f)$ be the average density of states for the solid-like sites and $N_\ell(E_f)$, the average density of states for liquid-like cells. By rewriting the total average density of states, eq. 6.1 becomes

$$\sigma = \kappa\, ((1-p)\, N_s(E_f) + p\, N_\ell(E_f)) \tag{6.2}$$

where p is the number of liquid-like cell and the normalized change in resistance during structural relaxation can be written as

$$\frac{\Delta\rho}{\rho_o} = \frac{(N_s(E_f) - N_\ell(E_f))}{N_s + p\,(N_\ell - N_s)}\,\Delta p \tag{6.3}$$

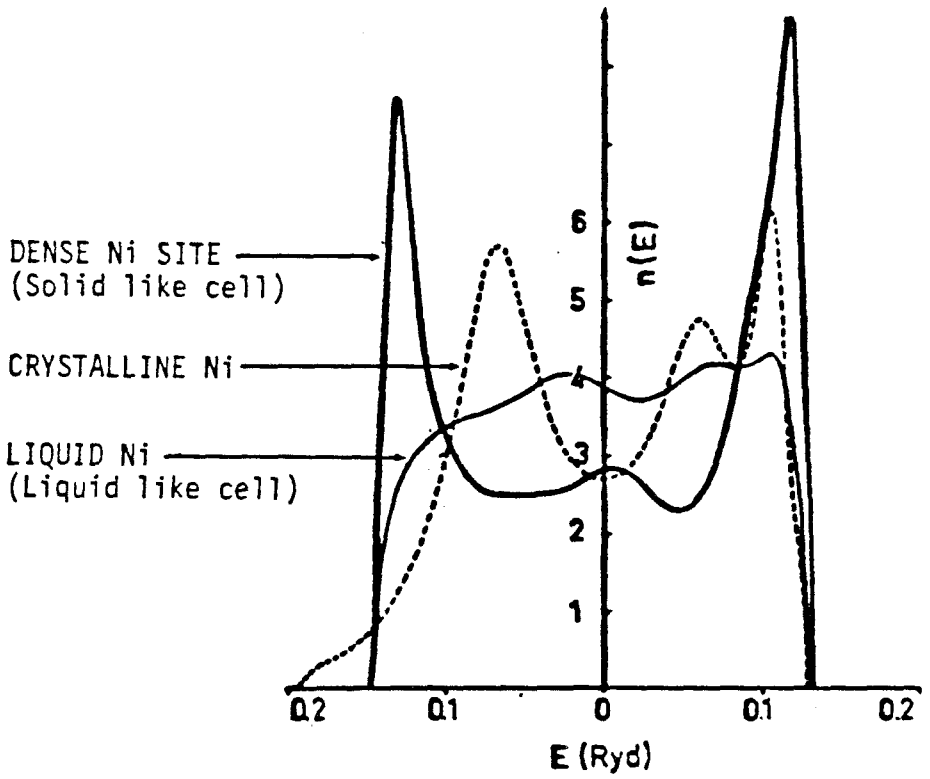

Fig. 6.1

Calculated local density of states: for nickel in a solid-like cell (high density region), for liquid nickel and for crystalline nickel (the data are from ref. 83).

When E_F is close to a band-edges, $N_s(E_f) > N_\ell(E_f)$ (fig. 6.1) and the resistivity should decrease upon structural relaxation whereas when it is close to the middle of the band the resistivity should increase during isothermal annealing. It is not surprising that eq. 6.3 is similar to eq. 2.2.16 since the local density of states is directly related to the local radial distribution function. The connection with Egami's model for structural relaxation is also evident since the local density of states on a site with hydrostatic stress p is governed by $G_p(r)$ given in eq. 2.2.6 and 2.2.8 .

Because of the great potential application of metallic glasses and the importance of the character of the homogeneity of a material in any industrial application, we will probably see, in the future, a growing interest in the use of electrical resistivity as a tool to detect phase transformation. Other techniques, more sophisticated and probably more powerful, have been used to study inhomogeneity in metallic glasses, however, electrical resistivity measurements are attractive since they can be performed so easily. It is not necessary to emphasize the great use of such measurements in studying age-hardening in conventional crystalline alloys.

There remains much work to be done from both the experimental as well as theoretical point of view. An X-ray hot stage diffractometer which will permit in-situ high-angle X-ray analysis up to 2400°C has been assembled by the author and small angle X-ray scattering experiments can now be performed in Dr. Johnson's laboratory at the California Institute of Technology. These systems can be of a great importance for anyone who would be interested in pursuing this work in the future.

REFERENCES

1. W. Klement, Jr., R.H. Willens, and Pol Duwez, Nature 187 (1960) 869.

2. W. Buchel and R. Hilsch, Z. Phys. 138 (1954) 109.

3. R. Hasegawa and C.C.Tsuei, Phys. Rev. B 2 (1970) 1631; G.S. Grest and S.R. Nagel, Ibid 19 (1979) 3571.

4. R.W. Cochrane, R. Harris, J.O. Strom-Olsen and M.J. Zuckermam Phys. Rev. Lett. 35 (1975) 676.

5. R. Asomoza, A. Campbell and A. Fert, J. de Phys. C-5, (1979) 225; F. Liu and J. Ruvalds, Physica B107 (1981) 623; S.J. Poon Solid State Comm. 45 (1983) 531.

6. R.W. Cochrane and J.O. Strom-Olsen, Phys. Rev. B 29 (1984) 1088.

7. E. Badic, R. Krsnik, B. Leontic, Z. Vucic, I. Zoric and Rizzuto Phys. Rev. Lett. 27 (1971) 805; R. Hasegawa, Phys. Lett. 38 (1972) 5.

8. P.J. Cole and L.V. Meisel, In Glassy Metals I, edited by H.J. Guntherodt and H. Beck (Springer, New York, 1980) 141.

9. P.K. Rastogi and Pol Duwez, J. Non Cryst. Solids 5 (1970) 1.

10. Phillippe Maitreplerre, J. App. Phys. 41 (1970) 498.

11. W. Teoh, N. Teoh and Sigurds Arajs, 2nd Intl. Conf. on Amorphous Metals (Plenum Press) Ed. Hasegawa & Loyy.

12. M. Sakata, N. Cowlam and H.A. Davies, J. Phys. F 11 (1981) L157.

13. E. Balanzat, C. Mairy and J. Hillairet, J. de Phys. C8, 41 (1980) 871 and E. Balanzat and J. Hillairet, J. Phys. F 12 (1982) 2907.

14. J.M. Ziman, Phil. Mag. 6 (1961) 1013.

15. D.L. Goodstein , States of Matter (Prentice-Hall, New Jersey 1975) 234.

16. T.E. Faber and J.M. Ziman, Phil. Mag. 11 (1965) 153.

17. A.B. Bhatiá and D.E. Thornton, Phys. Rev. B 2 (1970) 3004.

18. R.Evans, D.A. Greenwood and P. Lloyd, Phys. Lett. 35A (1971) 57.

19. L.V. Meisel and P.J. Cote, Phys. Rev. B 16 (1977) 2978; Phys. Rev. B 17 (1978) 4652; see also P.J. Cote and L.V. Meisel Phys. Rev. Lett. 39 (1977) 102.

20. I. Hernandez-Calderone, J.S. Helman and H. Vucetich, Phys. Rev. B 14 (1976) 2310.

21. D. Turnbbull and M.H. Cohen, J. Chem. Phys. 34 (1961) 120.

22. T. Egami, K. Maeda, D. Srolovitz and V. Vitek, J. de Phys. 41 (1980) C8-272.

23. K.F. Kelton and F. Spaepen, Proc. 4th. Intl. Conf. on Rapidly Quenched Metals (Sendai, 1981) 527.

24. N.W. Ashcroft and D.C. Langreth, Phys. Rev. 156 (1967) 685.

25. T. Egami, V. Vitek and D. Srolovitz, 4th. Intl. Conf. on Rapidly Quenched Metals (Sendai 1981).

26. D. Srolovitz, T. Egami and V. Vitek, Phys. Rev. B 24 (1981) 6936.

27. P. Allia, R. Sato Turtelli, F. Vinai, Solid State Comm. 43 (1982) 82.

28. P. Allia, D. Andreone, R. Sato Turtelli and R. Vinai, J. Appl. Phys. 53 (1982) 8798.

29. Morrel H. Cohen and G.S. Grest, Phys. Rev. B 20 (1979) 1077

30. C.C. Tsuei, Solid State Comm. 27 (1978) 691.

31. H.S. Chen and D. Turnbull, J. of Chem. Phys. 48 (1968) 2560

32. M. Avrami, J. Chem. Phys. 7 (1939) 1103; 8 (1940) 212 and 9 (1941) 177. See also B.G. Bagley and E.M. Vogel, J. Non Cryst. Solids 18 (1975) 29.

33. H.S. Chen, Appl. Phys. Lett. 29 (1976) 12

34. Joel L. Lebowitz, J. Marro and M.H. Kalos, Comments Solid State Phys. 10 (1983) 201.

35. J. W. Cahn, Trans. AIME 242 (1968) 166..

36. J. Marro, A.B. Bortz, M.H. Kalos and J.L. Lebowitz, Phys. Rev. B 12 (1975) 2000.

37. N.F. Mott, J. Inst. Metals 60 (1937) 267.

38. Z. Matyas, Phil. Mag. 40 (1949) 324.

39. H. Herman, J.D. Cohen and M.E. Fine, Acta Met. 11 (1963) 43.

40. R. Labusch, Phys. Stat. Sol. 3 (1963) 1661.

41. P.L. Rossiter and P. Wells, J. Phys. C 4 (1971) 354

42. P.L. Rossiter and P. Wells, Phil. Mag. 24 (1971) 425

43. A.J. Hillel, J.T. Edwards and P. Wilkes, Phil. Mag. 32 (1975) 189.

44. A.J. Hillet, Acta Met. 18 (1970) 253.

45. See for example A. Guinier, X-ray Diffraction, Freeman ed. (1963) Chapter 2.

46. Y. Waseda and H.S. Chen, Phys. Stat. Sol. B 87 (1978) 777.

47. J. Piller and P. Haasen, Acta. Met. 30 (1982) 1.

48. R. Schulz (unpublished results).

49. K. Binder and D. Stauffer, Z. Physik B 24 (1976) 407.

50. J.W. Cahn, Acta Met. 9 (1961) 795.

51. J.S. Langer, M. Baron, H.D. Miller, Phys. Rev. A 11 (1975) 1417.

52. J. Mimault, J. Delafond, A. Junqua, A. Naudon and J. Grilhe, Phil. Mag. B 38 (1978) 255.

53. R.B. Pond, U.S. Paten No. 2 (1958) 825, 108; T.R. Anthony and H.E. Cline, J. Appl. Phys. 49 (1978) 829.

54. P. Pietrokowsky, Rev. Sci. Instrum. 34 (1963) 445.

55. C.N.J. Wagner, Advan. X-ray Anal. 12 (1963) 50.

56. Atomic Structure Of Transition Metal Based Metallic Glasses, A.Williams, Doctorate Thesis, Cal. Inst. Of Tech. (1981).

58. S.R. Nagel, Phys. Rev. B 16 (1977) 1694.

59. N.F. Mott, Philos. Mag. 26 (1972) 1249 also N.F. Mott and H. Jones, The Theory Of The Properties Of Metals And Alloys.

60. T.K. Mitra, J. Phys. C 2 (1969) 52.

61. S. Barisic, Phys. Rev. B 5 (1972) 932.

62. N.F. Mott, Philos Mag. 26 (1972) 1949

63. S.M. Girvin and M. Jonson, Phys. Rev. B 22 (1980) 3583.

64. L.E. Ballentine, S.K. Bose, J.E. Hammerberg, J. Non Cryst. Solids 61 & 62 (1984) 1195 1200.

65. W.L. Johnson and A.R. Williams, Phys. Rev. B 20 (1979) 1640.

66. S.T. Hopkins and W.L. Johnson, Solid State Comm. 43 (1982) 537.

67. M. Mehra, R. Schulz and W.L. Johnson, J. Non Cryst. Solids 61 & 62 (1984) 859.

68. E. Helfand and N.R. Werthamer, Phys. Rev. Lett. 13 (1974) 686; Phys. Rev. 147 (1966) 288.

69. Alan Mak and W.L. Johnson, Phys. Lett. 89A (1983) 353.

70. Z. Altounian, Tu Guo-hua and J.O. Strom-Olsen, J. Appl. Phys. 53 (1982) 4755.

71. Z. Altounian, Tu Guo-hua and J.O. Strom-Olsen (preprint).

72. Z. Altounian, C.L. Folles, W.B. Muir and J.O. Strom-Olsen, Phys. Rev. B 27 (1983) 1955.

73. Y.D. Dong, G. Gregan and M.G. Scott, J. Non Cryst. Solids 43 (1981) 403.

74. K. Samwer and H.V. Lohneysen, Phys. Rev. B 26 (1982) 107.

75. Z. Altounian and J.O. Strom-Olsen, Phys. Rev. B 27 (1983) 4149.

76. D.M. Kroeger, C.C. Koch, J.O. Scarbrough and C.G. McKamey (preprint).

77. W.Y. Ching, L.W. Song and S.S. Jaswal (preprint).

78. Gerd Prufer, Doctorate Thesis, Gottingen University (1983).

79. Z. Altounian, C.L. Folles, W.B. Muir and J.O. Strom-Olsen, Phys. Rev. B 27 (1983) 1955.

80. F. Cyrot-Lackmann, J. de Phys. 35 (1974) C4-109.

81. S.N. Khanna and F. Cyrot-Lackmann, Phys. Rev. B 21 (1980) 1412.

82. F.Cyrot-Lackmann, J. Non Cryst. Solids 61 & 62 (1984) 1027.

83. S.N. Khana and F. Cyrot-Lackmann, Phil. Mag. B 38 (1978) 197.